Worldwide analysis of the limiting efficiency of 2-junction solar cells

T.H.W. Post

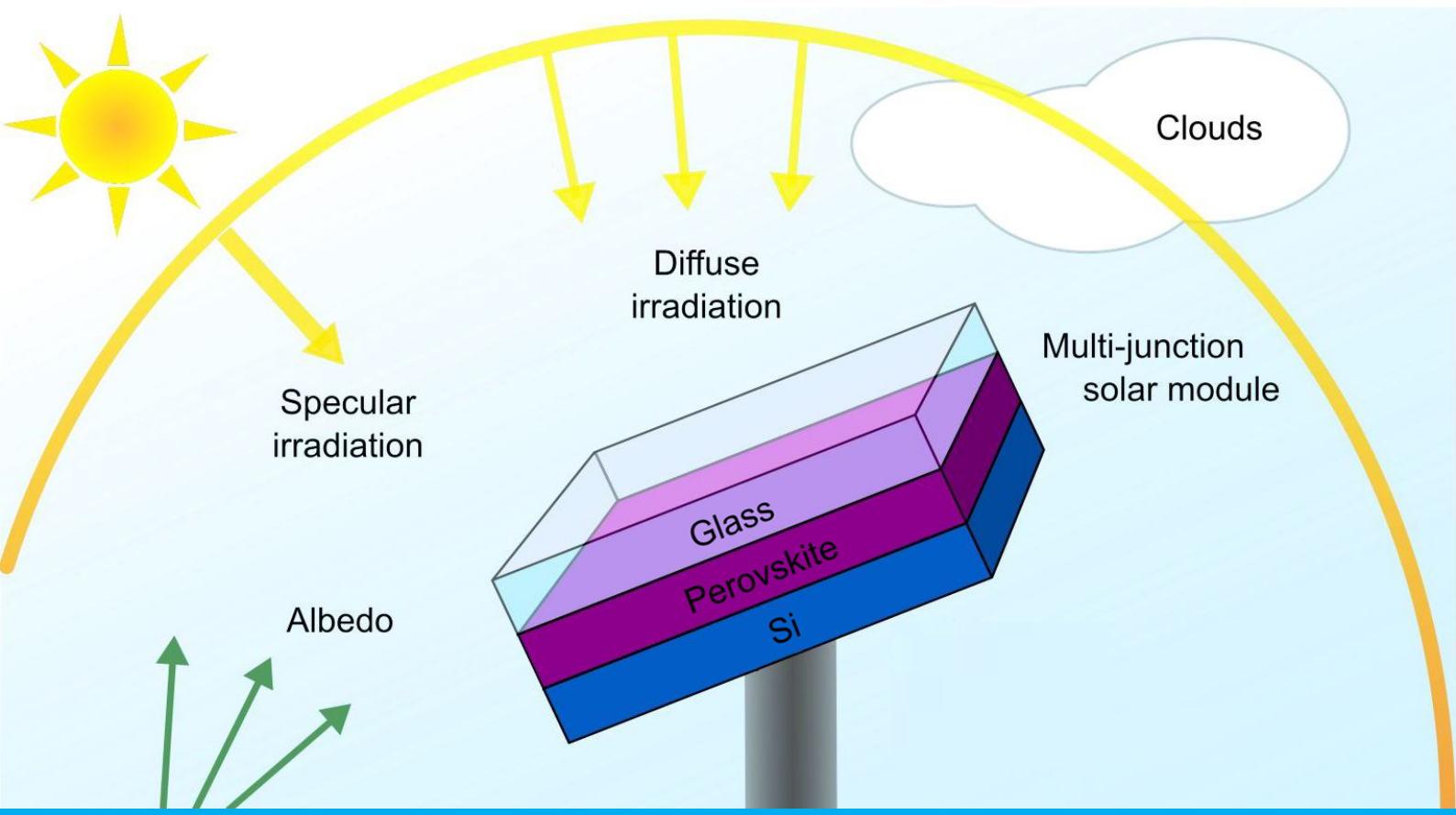

Cover image: [1]

Worldwide analysis of the limiting efficiency of 2-junction solar cells

by

T.H.W. Post

to obtain the degree of Master of Science
at the Delft University of Technology,
to be defended publicly on Thursday April 29, 2021 at 10:00 AM.

Student number:	4623029	
Project duration:	April 20, 2020 – April 29, 2021	
Thesis committee:	Dr. Olindo Isabella,	TU Delft, supervisor
	Dr. Hesan Ziar,	TU Delft, daily supervisor
	Prof. dr. ir. Miro Zeman,	TU Delft, internal committee member
	Dr. Paul Procel Moya,	TU Delft, external committee member
	Dr. Stephan de Roode,	TU Delft, external committee member

An electronic version of this thesis is available at `http://repository.tudelft.nl/`.

TU Delft

Abstract

As the efficiency of silicon (Si) photovoltaic (PV) moves ever closer to the theoretical limit, 2-junction PV becomes increasingly interesting. Since PV cells are tested under standard test conditions (STC), but real world working conditions differ, it is interesting to see how 2-junction PV performs worldwide in different climates. Worldwide spectra where simulated in SMARTS using data from NASA's Global Land Data Assimilation System (GLDAS), Clouds and the Earth's Radiant Energy System (CERES) and Socioeconomic Data and Applications Center (SEDAC) and from the Joint Institute for the Study of the Atmosphere and Ocean (JISAO). SMARTS provides only clear-sky spectra, to account for cloudiness, the BRL model is used.
The top absorber is 1.72 eV Perovskite and the bottom absorber is 1.12 eV Si. Because Si is an indirect bandgap material, a limiting Efficiency model by Richter et al. is used that takes both Auger and radiative recombinations into account. Because this model relies on variables and constants only given for Si, and the top absorber is a direct bandgap material, the detailed limit model by Shockley and Queisser is used to calculate the performance of Perovskite.
The distribution of high and low local yearly average irradiance is overall realistic, except for the north of Africa and the Middle East. Here aerosol optical depth (AOD) values are elevated. The elevated AOD can be explained by dust events, still these areas should be among the ones with the highest irradiance. The AOD effects the blue side of the spectrum mostly. All spectra where normalised using CERES' irradiance data.
The Richter model is thickness dependent. Thus the optimal thickness of Si is determined to find the optimal efficiency. To distinguish between the effects of the top layer and local climate effects on the thickness, firstly the optimal thickness of single junction Si is calculated and analysed. The optimal thickness ranges from 70 to 870 μm globally. The average is 205 μm and the irradiance weighted average is 165 μm. A relation between optimal thickness and ambient temperature was found.
For double junction Perovskite - Si current matching was used to find the optimum. The thickness of Si ranges from 10 to 4500 μm. But only nine locations (of 597) have a thickness above 500 μm. The average thickness is 77 μm and the irradiance weighted average is 81 μm. Locations with a high optimal thickness had a blue-er spectrum than the locations with a low thickness.
Using the optimal thickness of single junction Si and current matching, the optimal top-bandgap was determined around the world. The optimal bandgap ranges between 1.55 and 1.76 eV, the average is 1.655 eV and the irradiance weighted average is 1.663 eV. The relation between the top bandgap and optimal Si thickness was determined under STC. High bandgaps had the lowest optimal thicknesses and the thickness increased with decreasing top-bandgap. Alterations in spectrum and temperature where applied as well to find the effect on that relation. Decreasing temperature and airmass both resulted in an increase in optimal thickness per bandgap vise versa. Changing the spectrum has a greater effect than the temperature change.

Contents

1 Introduction

Solar is one of the fastest growing renewable energy sources [2] [3]. Approximately 95% of the sold photovoltaic (PV) modules (solar modules) is made with a Silicon (Si) semiconductor material [4]. The Shockley–Queisser limit (or detailed balance limit of efficiency) is the maximum theoretical efficiency limit of a single junction Si solar cell. It was formulated first in 1961 and was calculated to be 30% [5]. In 2013, Richter et al. [6] reassessed this theoretical limit to be 29.43%. As the efficiency of existing solar cells moves ever closer to this limit [7], 2-junction cells become increasingly interesting. Calculations of the efficiency of a solar cell, are usually based on Standard Test Conditions (STC) and since real working conditions differ from that, this thesis focuses on the effect that this difference has on the performance of single-junction and double-junction solar cells, around the world. The results are depicted in worldwide maps.

1.1. Loss mechanisms in PV modules

Part of the photons entering a PV cell, will contribute to the energy generation of that cell. The energy of an incoming photon can be lower than the bandgap energy, exactly the same or higher. Photons with a too low energy will contribute to non-absorption: these photons will pass trough the cell without interaction. Photons with the same or higher energy than the bandgap can create an electron-hole pair. The surplus of energy from the photons will be released as heat: thermalisation loss. A solar cell with a large bandgap will have a small amount of thermalisation losses, but most photons will pass through, because most photons have a too low energy to be absorbed. Visa versa, in a solar cell with a small bandgap a larger amount of the incoming light spectrum can be absorbed, but thermalisation will be high. Using multiple junctions in a solar cells can decease both unabsorbtion and thermalisation losses, as depicted in Figure 1.1. The incoming

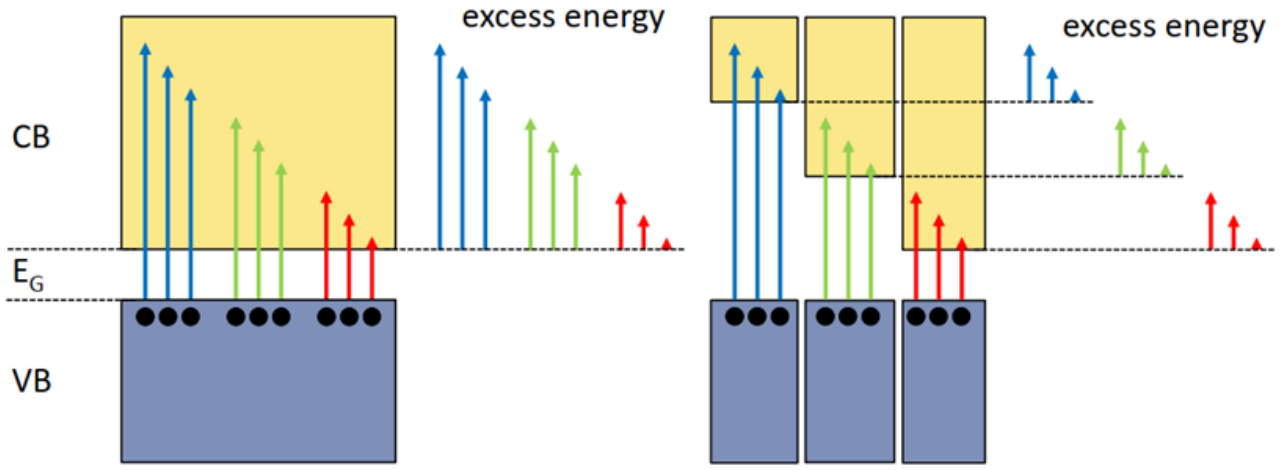

Figure 1.1: Energy losses with one (left) and three junctions (right). VB stand for valance band, CB stands for conduction band and E_g is the bandgap energy. [8].

irradiation in this figure moves from left to right. Using a large bandgap as top layer and a smaller bandgap solar cell at the bottom, a large range of photons can be absorbed and the amount of excess energy is lower. In this thesis, the performance of 2-junction (2 absorberlayer) PV cells are analysed.

1.2. A global PV efficiency map

PV cells are tested under standard test conditions (STC). These are: AM1.5 spectrum, 1000W/m^2 incoming irradiance and a 25°C cell temperature. AM stands for air mass. When light reaches the top of the atmosphere, it travels thought to reach the earths surface. The amount of air mass depends on the angle of the sun, which can be seen in Figure 1.2. Since the distance between the earths surface and the sun differs per location on earth, the amount of incoming irradiance, the spectrum of the irradiance and the air temperature vary across the globe.

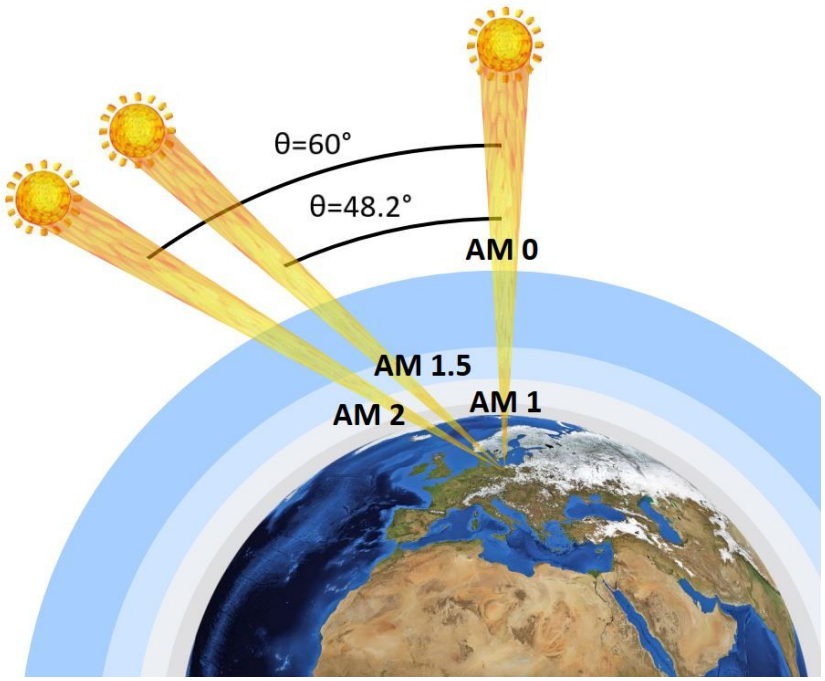

Figure 1.2: The air mass depends on the angle of the sun [9].

Globally these conditions vary, thus the performance of an installed PV panel will differ from the STC performance. A map with the calculated efficiency per area on earth would be a helpful tool to use before PV installation to decide what would be the best absorber layer and best design parameter choices. A PV Energy yield map for single junction solar cells has been developed by Peters and Buonassisi [10]. Peters and Buonassisi used the detailed-balance (Shockley–Queisser) method to determine the Energy yield. In Figure 1.3 their 2015 Global Energy Yield results for Si are depicted.
A year ago, a performance ratio (PR) map for silicon-based multi-junction solar cell was created by Liu et al. [11]. PR is the ratio of the actual- to the theoretical energy output. Optical absorption and current generation were primarily calculated with EQE values from literature. Five different configurations (among which two-terminal(2T) and four-terminal(4T)) and multiple material combinations are compared. In a 2T configuration, the two absorber layers and connected in series via a tunneljunction and in a 4T configuration the top and bottom layer are electrically isolated from one another. Figure 1.4 is a depiction of the configurations. Figure 1.5 is an example of a PR map for a 2T and 4T cell for 2015. Liu at al. studied what the best standard performance across the globe is for one standard cell (based of measured EQE from literature), but the purpose of this study is to obtain the best possible cell by using a theoretical approach. The efficiency of the 2-junctions solar cells, will be calculated for a 2T configurations, for 2019. A 4T cell is harder to create and thus not as attractive to the market as 2T configurations. The Shockley and Queisser model as documented by Rühle [12] and the Limiting Efficiency model by Richter [6] are used to calculated the performance of top and bottom cell respectively. Richters model takes into account both the Auger and radiative

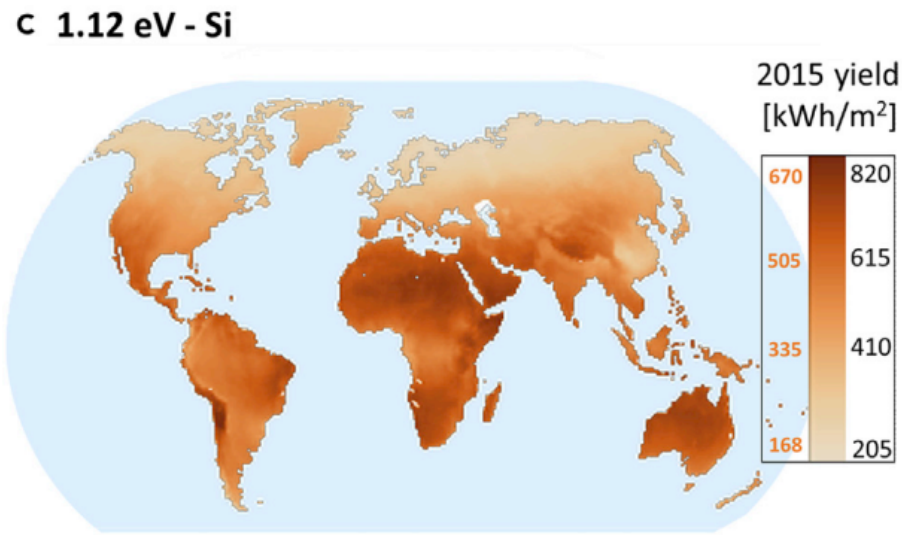

Figure 1.3: The 2015 Global Energy Yield for Si according to Peters and Buonassisi [10]. The two axes are corresponding to the radiative limit (right) and a projection to record solar cell efficiencies (left, color);

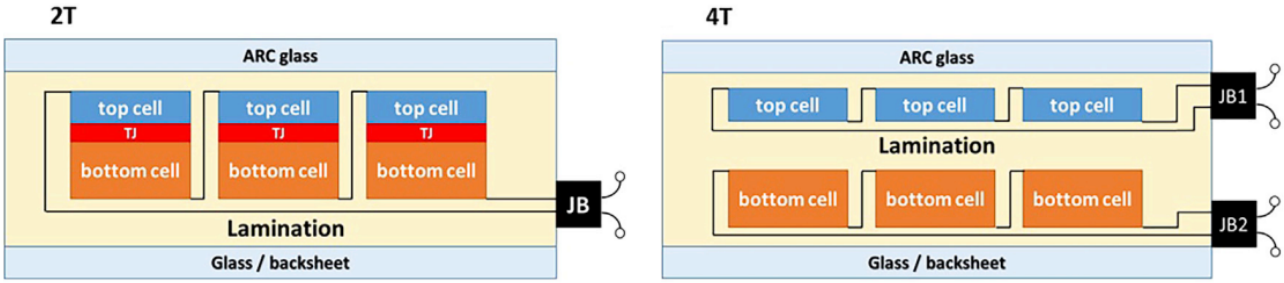

Figure 1.4: Schematic depiction of a two-terminal(2T, left) and a four-terminal(4T, right) configuration [11].

losses of the indirect-bandgap Si bottom. The Auger losses are dependent of thickness, thus this research will give information about optimal thickness as a function of location on earth and top layer. Lastly, for the final calculations, p-type Si is considered, since it currently has a higher marked share [13] [14].

1.3. Thesis report structure

This report starts with the first necessity to build a global model: data. Information about the data and their sources are given in chapter 2. Besides data, working models to present the top- and bottom absorber layer are needed. In chapter 3 all used models are explained. In chapter 4 the validations are shown. The simulated results are presented in chapter 5 and lastly in chapter 6 the conclusion and recommendations are given.

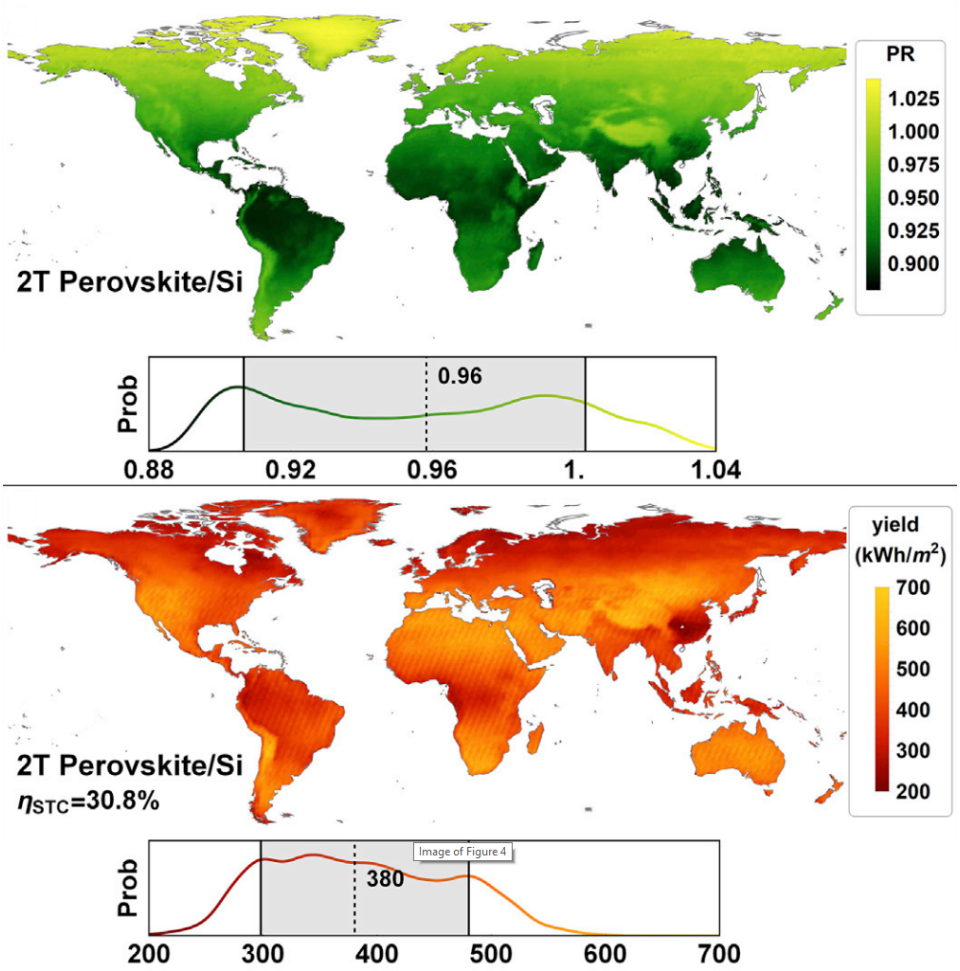

Figure 1.5: Perovskite-Si tandem cell 2T PR (top) and yield (bottom) for 2015 [11].

2

Input data

The global horizontal irradiance (GHI) consists of a direct and diffuse irradiance component, the direct normal irradiance (DNI) and diffuse horizontal irradiance (DHI). The spectra of these components, for clear-sky conditions, in 2019, are simulated using Simple Model of the Atmospheric Radiative Transfer of Sunshine (SMARTS) version 2.9.5 [15]. SMARTS uses a text file to import its input variables and simulation preferences from. This .txt file can be altered to create an as specific scenario as is preferred. Matlab [16][17] code were used to alter the input file, run SMARTS and extract the output data into .mat file. The functions to do this, are based on code by de Mooij [18].
To represent the diverse climate conditions around the world, global data from a variety of sources is used. The time resolution of all used data is hourly or 3-hourly. In this chapter the different sources will be named and adjustments for SMARTS are explained. The yearly average data is depicted on map in Appendix A. For the albedo spectrum and aerosol model, data is used as an condition to choose between two spectra and models from SMARTS' selection. In section 2.5 the details will be discussed and other calculation preferences will be named here as well.

2.1. GLDAS data

Air temperature at the earth surface, relative humidity and surface pressure data are obtained from NASA's Global Land Data Assimilation System (GLDAS) Version 2 Data Products, from GLDAS Noah Land Surface Model L4 3 hourly 1.0 x 1.0 degree V2.1 [19] [20]. The special resolution of the data is 1° x 1°, with 3 hour intervals. Because each value is the average of the past 3 hours, the first file is from January 01 3:00 and the last file is from January 1 2020 0:00. Files each contain one time interval, a bulk downloader is recommend to use. The files are .nc4 files and can be opened in Matlab using `ncinfo` and `ncread`.
The temperature is given in K and SMARTS needs the input to be in °C, thus 273.15 is subtracted from all temperature values. The pressure data is in Pa and is divided by 100 the convert it to mbar, which is the necessary unit for SMARTS. Lastly, the humidity is specific humidity, q, given in kg/kg. For SMARTS, the input needed is relative humidity, RH, and it is computed as follows:

$$RH = \frac{w}{w_s} \cdot 100\% \tag{2.1}$$

$$q = \frac{m_{wv}}{m_{wv} + m_d} \tag{2.2}$$

Where:

$$w = \frac{m_{wv}}{m_d} \tag{2.3}$$

where w is the mass mixing ratios of water vapor and w_s is the saturation mass mixing ratios of water vapor (mixing ratio for which RH = 100%). m_{wv} is the mass of water vapor and m_d the mass of dry air. Adding Equation 2.2 and 2.3 together gives [21]:

$$w = \frac{q}{1-q} \approx q \tag{2.4}$$

The difference between $\frac{q}{1-q}$ and q ranges from $7.3{\cdot}10^{-7}$ (for $q = 8.5{\cdot}10^{-4}$ kg/kg) to $3.8{\cdot}10^{-4}$ (for $q = 1.9{\cdot}10^{-2}$ kg/kg). The saturated mixing ratio can be written as:

$$w_s = \frac{M_v}{M_d}\frac{e_s}{M_d} = 0.622\frac{e_s}{p-e_s} \approx 0.622\frac{e_s}{p} \tag{2.5}$$

where M_v is the specific mass of water vapor, M_d is the specific mass of dry air, e_s is the saturated vapor pressure and p is pressure (in mbar) [22]. The Clausius–Clapeyron relation states:

$$\frac{e_s}{e_0} = \frac{e_s}{6.11} = \exp\left(\frac{L_v}{R_v}\left(\frac{1}{T_0}-\frac{1}{T}\right)\right) \tag{2.6}$$

$$e_s = 6.11\exp\left(\frac{L_v}{R_v}\left(\frac{1}{T_0}-\frac{1}{T}\right)\right) \tag{2.7}$$

Where e_0 is the saturated vapor pressure (in mbar) at 273.15 K, Lv is the latent heat of vaporization, R_v is the specific gas constant for water vapor, T_0 is the reference temperature (273.15 K) and T is the temperature [23]. Using saturation vapor pressure data, a simplified relation for e_s can be written as [24]:

$$e_s \approx 6.11\exp\left(\frac{17.67(T-T_0)}{T-29.65}\right) \tag{2.8}$$

Inserting Equation 2.4, 2.5 and 2.8 into Equation 2.1 gives:

$$RH = q\cdot\left(0.622\frac{e_s}{p}\right)^{-1} = 0.263\cdot q\cdot p\cdot\exp\left(\frac{17.67(T-T_0)}{T-29.65}\right)^{-1} \tag{2.9}$$

2.2. CERES data

Precipitable water, ozone total-column, snow coverage, aerosol optical thickness at 550 nm, surface shortwave down flux and top-of-atmosphere (TOA) shortwave flux data came from NASA's Clouds and the Earth's Radiant Energy System (CERES) data product SYN1deg[25] [26] [27]. The data, desired area, time range and -resolution can be selected on their data product page [28]. The chosen time resolution is hourly (resolutions of 3-hourly and monthly averages are available as well) and the fluxes are all-sky (clear-sky is available as well). The CERES SYN1deg products have a 1° x 1° resolution. The files are .nc files and can be opened in Matlab using `ncinfo` and `ncread`.
Of the used data, CERES SYN1deg's own products are the TOA- and surface fluxes. The other available products come from several different sources. The snow and ice daily coverage is from the NSIDC (National Snow and Ice Data Center) Near-Real-Time SSM/I-SSMIS EASE-Grid Daily Global Ice Concentration and Snow Extent product, the column ozone amount is taken from the Goddard Earth Observing System (GEOS-5.4.1) and the aerosol optical thicknesses are from an aerosol transport model MATCH [29] [30].

2.3. Altitude data

The altitude data comes from the Joint Institute for the Joint Institute for the Study of the Atmosphere and Ocean (JISAO) [31]. The data set covers the whole earth and has a resolution of 1° x 1°. This 1 degree data is from Rand Corporation / Scripps Institution of Oceanography [32]. Is is a revision done in 1975. Details of data sources and estimation methods used in the original Scripp tabulation are given by Smith, Menrd, and Sharman (1966) [33]. The data is presented in one .nc file and can be opened in Matlab using `ncinfo` and `ncread`.

2.4. Urban Extents Grid

The Urban Extents Grid data has been made available by NASA's Socioeconomic Data and Applications Center (SEDAC) [34]. It is determined whether areas on earth are urban on rural. To determine urban areas, a combination of population counts, settlement points, and the presence of Nighttime Lights is used. Areas are defined as urban if they are either a cluster of lighted cells from the Nighttime Lights or buffered settlement points for which the total population is greater than 5000 persons. The population count consist of estimates from 1990, 1995, and 2000. The estimated areas are urban areas in 1995. The earth is divided by 30 arc-second (1km) grid. One arc-second is 1/3600 of a degree [35]. The data covers all area from east to west

and is bounded by 84 degree north and -56 degree south. The chosen file format is .bil (other options: .ascii and gris) it can be opened in Matlab using `multibandread`. The required input information for this function can be found in the corresponding .hdr file.

2.5. Other SMARTS adjustments

Two albedo spectra are used: light soil (code 38, which is also used to obtain the reference ASTMG spectra [36]) and snow (code 3). Which albedo is use, is determined using the CERES snow coverage data. When the snow coverage is ≥ 50%, the snow albedo is used.

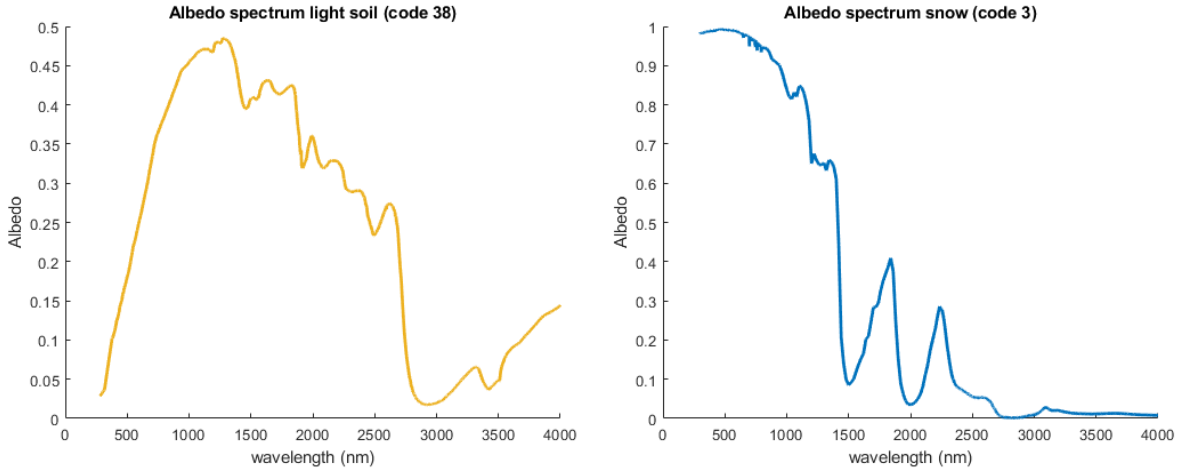

Figure 2.1: Light soil albedo spectrum (left) and snow albedo spectrum (right).

The aerosol model is also chosen from SMARTS' collection. Either S&F_RURAL or S&F_URBAN is used. This depends on NASA's Urban Extents Grid data, which tells whether a location in in an urban or rural area.
The tilt angle is the optimal tilt angle, calculated according to Quinn and Lehman [37]. SMARTS uses only positive angles, thus the absolute value is calculated:

$$\beta_{opt} = \left| (\cos(\gamma) \cdot \tan(\vartheta) \left[\left(1 + \frac{((\tau\alpha)_d \cdot g(k_T) - (\tau\alpha)_r \cdot \rho_g)}{2 \cdot (1 - g(k_T))} \right)^{-1} \right] \right| \tag{2.10}$$

γ is the surface azimuth, which is extracted from one of SMARTS' output files. This will be explained in section 3.2. ϑ is the latitude and ρ_g is the ground reflectance and is assumed to be 0.2. The average values of either albedo spectrum is 0.2 and it was assumed in the paper as well. $(\tau\alpha)_d$ and $(\tau\alpha)_r$ are the transmittance-absorptance product of the diffuse- and the reflected radiation stream. Both are assumed to be 1. k_T is the average annual clearness index, which will be introduced further in section 3.1. The correlation used for $g(k_T)$ is:

$$g(k_T) = \begin{cases} 0.977 & k_T \leq 0.15 \\ 1.237 - 1361 \cdot k_T & 0.15 \leq k_T \leq 0.7 \\ 0.273 & k_T \geq 0.7 \end{cases} \tag{2.11}$$

The surface azimuth is 180° (surface facing south) in the northern hemisphere and 0° (surface facing north) in the southern hemisphere. The solar position and air mass are calculated using the date (year, month, day, hour) and location (latitude and longitude). The spectral range between which all spectral calculations are be performed, is 280-4000 nm, with 10 nm intervals. And the results that were printed are direct tilted irradiance and diffuse tilted irradiance (IOUT number 6 and 7).

2.5.1. SMARTS limitations

SMARTS has a minimum temperature limitation, which is not described in the manual. The minimal temperature depends on the surface pressure and altitude. The altitude can be given as input data by itself or

SMARTS can calculate the altitude, using the surface pressure. In Table 2.1 surface pressure values are given, together with the calculated altitude and minimum temperature. In Figure 2.2 the minimum temperature is plotted as a function of the surface pressure and as a function of the altitude. It can immediately be seen that the highest minimum temperature is not at either highest or lowest value of either, but peaks in between. The reason for this is unknown. Because of this behaviour, the input temperature for SMARTS was limited to a minimum of -32.24 °C.

Table 2.1: Pressures, corresponding altitudes and the minimum temperature.

Pressure (mbar)	**Altitude (km)**	**minimum temperature (°C)**
718.00	2.805	-35.63
730.00	2.674	-35.09
750.00	2.461	-34.20
770.00	2.252	-33.32
790.00	2.048	-32.45
794.72	2.000	-32.25
800.00	1.947	-32.33
810.00	1.848	-32.48
850.00	1.459	-33.13
900.00	0.994	-34.03
950.00	0.550	-34.75
1000.00	0.125	-35.51
1015.00	0.0004	-35.74
1015.05	0.000	-35.75

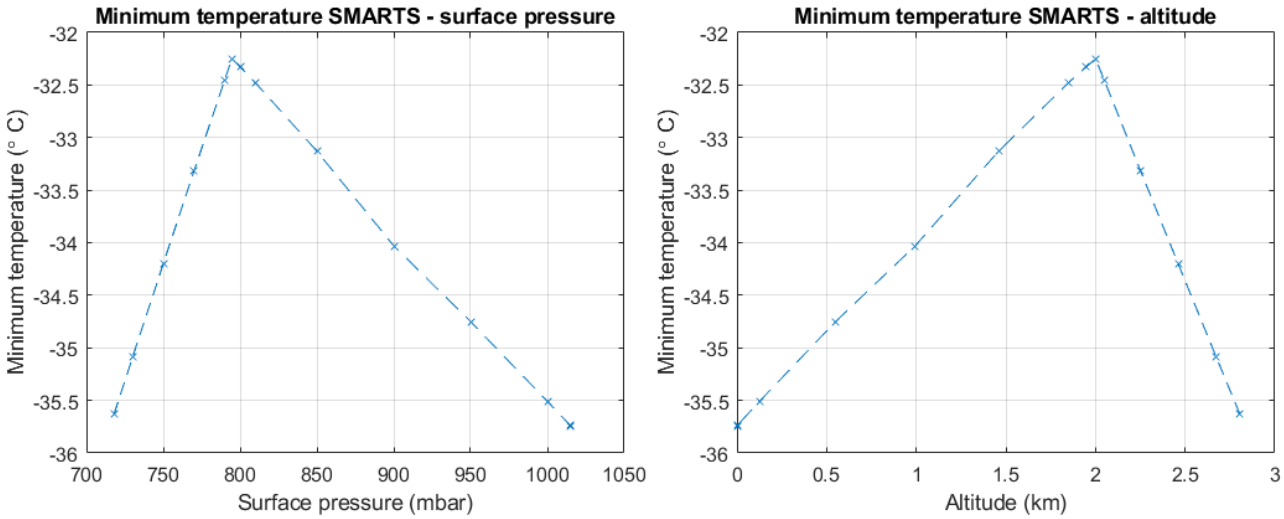

Figure 2.2: Minimum tempearture for SMARTS as function of pressure (left) and corresponding altitude (right).

Another limitation (which is mentioned in the manual) is the maximum allowed value of aerosol optical depth (AOD) at 550 nm is up to 5.0. In the manual it is state that the maximum allowed values is 5.0, but in reality, that is already too high. Thus all AOD values all limited to 4.999. AOD at 500 nm (which is another input option for the same card) does not have this limitation, but a complete data set for this wavelength could not be found.

3

Model explanation

The modeling has been made visual in a flow chart, depicted in Figure 3.1. SMARTS simulates clear-sky DNI and DHI spectra. To simulate the influence of clouds, BRL model is used. Since SMARTS aborts calculations when the sun is below the horizon, all input values used after the SMARTS simulation, need to be resized correctly using the "night filter". The efficiencies of the top layers, which both are direct-bandgap, are calculated using the detailed balance method [12]. For the indirect-bandgap Si bottom layer a reassessed model by Richter et al. is used [6]. In this chapter all these steps are explained and necessary equations are given.

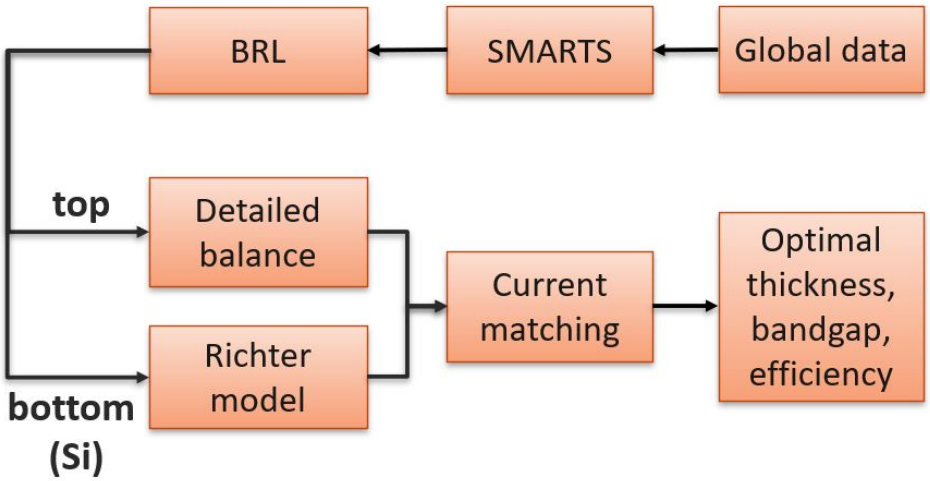

Figure 3.1: Flowchart of model.

3.1. BRL model

SMARTS only simulates irradiation under clear-sky conditions. To account for cloudiness, the diffuse and direct irradiation ratio's (d_f, d_r) for these circumstances are needed to determine the all-sky spectrum:

$$GHI_{all-sky} = (d_r \cdot DNI_{clear-sky}) \cdot \cos(\theta) + d_f \cdot DHI_{clear-sky} \tag{3.1}$$

Where:

$$d_r = \frac{DNI_{all-sky}}{GHI_{all-sky}} \tag{3.2}$$

$$d_f = \frac{DHI_{all-sky}}{GHI_{all-sky}} \tag{3.3}$$

θ is the zenith angle. Best would be to use data sets of GHI, DHI and DNI to determine these ratios, but since DHI and DNI data on a large geographica; scale is rare, it was decided to use a model to estimate the ratios.

In 2010, Ridley et al. [38] developed a model with as many predictors as possible, that requires as little as possible recorded data, the Boland–Ridley–Lauret (BRL) model. Ridley et al. compared the BRL model with Reindl[39], Skartveit[40] and Perez[41] models. The BRL model outperforms the other models in both northern and southern hemispheres. Torres et al. [42] compared 17 different diffuse fraction models, among which 3 models that consider the process dynamics: Dirint model[41], Skartveit et al. model[40] and lastly the BRL model. All three outperformed the other models, they showed a better fit to the measured irradiance. Plus, the Dirint and BRL model perform best when comparing the calculated diffuse ratio. Lastly it is concluded that the BRL model is more easily applied. Because of its simplicity and good performance, the BRL model is used to estimate the hourly diffuse ratio.
The Matlab code for the BRl model was made by Mishra[43] and Stark [44]. The BRL model is an extension of the simple, single predictor generic model developed by Boland et al. [45], two year earlier. The single predictor uses the hourly clearness index, k_t. This is the ratio of irradiance which reaches the earth's surface to the top-of-atmosphere (TOA, extraterrestrial) irradiation. Both variables are data from CERES about which more can be found in section 2.2. The generic equation with one predictor and the clearness index are given by :

$$d_f = \frac{1}{1+\exp(-5.0033+8.6025\cdot k_t)} \tag{3.4}$$

$$k_t = \frac{I_{surface}}{I_{TOA}} \tag{3.5}$$

In the BRL model, the general equation to calculate the diffuse ratio is:

$$d_f = \frac{1}{1+\exp(-5.38+6.63\cdot k_t+0.006\cdot AST-0.0077\cdot\alpha+1.75\cdot K_t+1.31\cdot\Psi)} \tag{3.6}$$

The extra predictors of this formula are solar elevation α, Apparent Solar Time AST, daily clearness index K_t and persistence Ψ. Data from seven locations worldwide were used to determine the parameters (weight) of all predictors. The daily clearness is the ratio of the sum of both surface- and top-of-atmosphere irradiance.

$$K_t = \frac{\sum_{i=1}^{24} I_{surface}}{\sum_{i=1}^{24} I_{TOA}} \tag{3.7}$$

The AST can be calculated by [46]:

$$AST = h + TZ - \frac{\lambda}{15} + \frac{E_t}{60} \tag{3.8}$$

where h is the hour of the day, TZ is the time zone with respect the Coordinated Universal Time (UTC). The TZ is determined based on the longitude λ. Lastly, E_t is the equation of time, which is:

$$\begin{aligned} E_t =& (0.000075 + (0.001868\cdot\cos(\Gamma)) - (0.032077\cdot\sin(\Gamma)) \\ & - (0.014615\cdot\cos(2\cdot\Gamma)) - (0.04089\cdot\sin(2\cdot\Gamma)))\cdot 229.18 \end{aligned} \tag{3.9}$$

In which Γ is the day angle:

$$\Gamma = 2\pi\cdot\frac{day-1}{365} \tag{3.10}$$

In this equation, day is the day number of the year, which can range from 1 to 365.
The solar elevation angle, α, is the inverse of the zenith angle (θ_z):

$$\alpha = 90^\circ - \theta_z \tag{3.11}$$

The zenith angle used in the BRL model, is CERES data, because the irradiance input is CERES data as well.
Ψ is an average of both a lag and a lead of the clearness index. This predictor was chosen to take into account atmospheric inertia.

$$\Psi = \begin{cases} \frac{k_{t-1}+k_{t+1}}{2} & sunrise < t < sunset \\ k_{t+1} & t = sunrise \\ k_{t-1} & t = sunset \end{cases} \tag{3.12}$$

When DHI is detemined, Equation 3.13 can be used to calculate DNI and finally d_r. The CERES surface irradiance data is used as GHI for this equation.

$$GHI = DNI\cdot\cos(\theta_z) + DHI \tag{3.13}$$

3.1.1. BRL zenith mismatch

zenith mismatch (= time mismatch)
scale of error

3.2. Night filter

The output of SMARTS consists of 3 files: 'smarts295.ext.txt' contains the tabulated results, 'smarts295.out.txt' contains information about in- and output (and errors) and 'smarts295.inp.txt' is a copy of the input file. The results for the ext file are imported into .mat files. When the zenith angle is > 90° (sun below horizon), the simulation is aborted and SMARTS will continue and try the next hour. As a result, no numbers will be printed in the ext file for that hour. To match the length of SMARTS's output (.ext), the input values for all calculations after the simulation step, need to be resized. Since the .out file does contain all information, all zenith values are extracted form there (using `textscan` and `regexp`) and used to filter out the input data at night.

3.3. Efficiency and fill factor

The efficiency, η, and fill factor, FF, of a solar cell can be expressed as[47]:

$$\eta = \frac{V_{mpp} \cdot J_{mpp}}{\int_{280nm}^{4000nm} GHI(\lambda)} \tag{3.14}$$

$$FF = \frac{V_{mpp} \cdot J_{mpp}}{V_{oc} \cdot J_{sc}} \tag{3.15}$$

V_{mpp} and V_{oc} are the voltage at the maximum power point (mpp) and the open circuit (oc) voltage. J_{mpp} and J_{sc} are the current density at mpp and short circuit (sc). The currents are calculated in Matlab [16][17], using the detailed balance model [12] for the top layer and the model by Richter [6] for the Si bottom layer. The voltage input for the equations starts at 1 mV and increases with 0.5 mV steps until the current becomes negative.
For a 2-junction solar cell, with a two-terminal (2T, see section 1.2) configuration, the efficiency and FF will be calculated as described in Equation 3.14 and 3.15, but the voltage used, is the sum of the voltage of both absorber layers. And the current used, is the lowest of the two. The cell that produces the lowest current is called the limiting cell.

3.4. Detailed balance model

The formula of the Detailed Balance model are for a paper from Rühle [12]. The first version of the Matlab code of this model was made by Ziar[48]. The detailed balance model is based on an ideal p-n junction. The single type of recombination taken into account is radiative recombination. This the dominant loss mechanism for direct band gap materials [47], thus the model is only applicable for the top layers. The bandgaps of absorber materials considered are given in Table 3.1.

Table 3.1: Bandgaps of used absorber materials

	Si	**CdTe**	**Perovskite**
$E_g(eV)$	1.12 [47]	1.45 [49]	1.72 [50]

The external current (the final current generated by the module) is calculated according to:

$$J_{ext} = J_{max} - J_r(V) + J_{nr}(0) - J_{nr}(V) = J_{max} - J_r(V) \tag{3.16}$$

J_{max} is the maximum photocurrent density and J_r is the radiative recombination current density. J_{nr} are the non-radiative processes and are neglected. J_{max} can be expressed as:

$$J_{max} = \int_0^\infty a(E)\Phi^i(E)dE \tag{3.17}$$

And a is the absorbance, which in an ideal case is one for $E_{photon} \geq E_g$. Absorbance can be calculated with Equation 3.37, but the absorbance is positively related to the thickness in that equation and the loss is not related to thickness in this model. Because the losses will not increase with increasing thickness, an optimal

will never be found: the optimal thickness and the corresponding efficiency would keep increasing. Φ^i is the incident spectral photon flux. The spectral global horizontal irradiance is simulated in SMARTS and can be converted into flux using Equation 3.18.

$$\Phi^i = \frac{q\lambda}{hc} GHI(\lambda) \tag{3.18}$$

q is the elementary charge, h is the Planck constant and c is the speed of light.
The radiative recombination current, J_r, is calculated using:

$$J_r = f_g q \int_0^\infty \Phi^e(E,V)dE \tag{3.19}$$

f_g is a geometrical factor and is schematic displayed in Figure 3.2. F_g is 2 when assuming that the solar cell is emitting radiation from the front and rear side and F_g is 1 if a perfect back reflector is placed onto the rear side and radiation is emitted at the front side only. Since the top layer needs to emit light to the bottom layer, F_g is 2. Rühle assumed f_g to be 2 as well. q is the elementary charge and Φ^e is emitted photon flux. Φ^e is

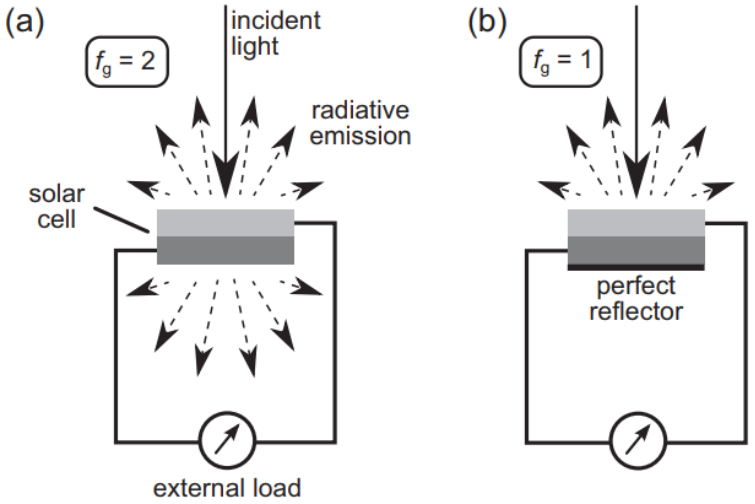

Figure 3.2: Schematic solar cell. In (a) the geometrical factor f_g is 2 and the cell emits light at top and rear side. In (b) f_g is 1, a perfect reflector is attached to the rear side and light is only emitted at the front side [12]

.

calculated according to:

$$\Phi^e(E,V) = \frac{2\pi E^2}{h^3 c^2} \frac{a(E)}{\exp\left(\frac{E-qV}{k_B T_c}\right) - 1} \tag{3.20}$$

k_B is the Boltzmann constant, T_c is the cell temperature, V is the external applied voltage and E is the spectral energy, which can be converted from λ using [47]:

$$E = \frac{h \cdot c}{\lambda} \tag{3.21}$$

The cell temperature can be determined using [51]:

$$T_c = T_a + \frac{T_{NOCT} - 20°C}{800} G_M \tag{3.22}$$

T_a is the ambient temperature, for which GLDAS data is used and G_M is the solar irradiance. T_{NOCT} is the nominal operating cell temperature (NOCT). The NOCT is the cell temperature under 800 W/m^2 irradiance, 20 °C ambient temperature and a wind speed of 1 m/s [47]. The values of NOCT ranges per research work, Table 3.2 shows the T_{NOCT} used here.

Table 3.2: Nominal operating cell temperatures

	Si	**CdTe**	**Perovskite**
$T_{NOCT}(°C)$	44 [52]	45 [53]	43 [52]

3.5. Auger and radiative losses model

For an indirect bandgap material, Auger recombination is an important loss mechanism[47]. For Si, the model by Richter[6], which includes both Auger recombination and radiative recombination, is used. The Auger recombination is assumed to be constant with different temperatures. Here, the external current is written as:

$$J = J_L - qWR_{intr} \tag{3.23}$$

J_L is the photocurrent density generated by the incident light (which will be explained in Equation 3.42), q is the elementary charge, W the cell thickness and R_{intr} is the intrinsic recombination rate.

$$R_{intr} = \frac{\Delta n}{\tau_{intr}} \tag{3.24}$$

Δn is the excess carrier concentration and τ_{intr} is the intrinsic bulk lifetime (which is expressed in Equation 3.29). Δn can be determined by solving the following equation:

$$n \cdot p = (n_0 + \Delta n) \cdot (p_0 + \Delta n) = n_{i,eff}^2 \exp\left(\frac{qV}{k_B T_c}\right) \tag{3.25}$$

n and p are the electron and hole concentrations respectively, n_0 and p_0 are these concentrations at equilibrium. V is the external applied voltage, k_B is the Boltzmann constant and T_c is the cell temperature (calculated using Equation 3.22). $n_{i,eff}^2$ is the effective intrinsic carrier concentration, which has the following relation:

$$n_{i,eff} = n_{i,0} \exp\left(\frac{\Delta E_g}{2k_B T_c}\right) \tag{3.26}$$

n_i is the intrinsic carrier concentration and ΔE_g is energy bandgap narrowing (BNG). Because of its small effect [54] (0.14% decrease of efficiency) and complicated expression [55], bandgap narrowing is assumed to be 0, making $n_{i,eff}^2$ equal to $n_{i,0}$. For $n_{i,0}$, the expression formulated by Sproul is used [56] [57]:

$$n_{i,0} = 1.541 \cdot 10^{15} T^{1.712} \exp\left(\frac{-E_g^0(T_c)}{2k_B T_c}\right) \tag{3.27}$$

E_g^0 is the intrinsic bandgap. For this, the relation by Thurmond is used [58] [57]:

$$E_g^0(T_c) = E_g^0(0) - \frac{\alpha \cdot T_c^2}{T_c + \beta} \tag{3.28}$$

$E_g^0(0)$ (Si bandgap at 0 K) is 1.17 eV, α is $4.73 \cdot 10^{-4}$ eVK^{-1} and β is 636 K. The intrinsic bulk lifetime, τ_{intr}, can be expressed using [54]:

$$\tau_{intr,adv} = \frac{\Delta n}{(n \cdot p - n_{i,eff}^2)(2.5 \cdot 10^{-31} g_{eeh} \cdot n_0 + 8.5 \cdot 10^{-32} g_{ehh} \cdot p_0 + 3.0 \cdot 10^{-29} \Delta n^{0.92} + B_{rel} \cdot B_{low} \cdot (1 - P_{PR}))} \tag{3.29}$$

g_{eeh} and g_{ehh} are enhancement factors, formulated as follows:

$$g_{eeh}(n_0) = 1 + 13\left\{1 - \tanh\left[\left(\frac{n_0}{N_{0,eeh}}\right)^{0.66}\right]\right\} \tag{3.30}$$

$$g_{ehh}(p_0) = 1 + 7.5\left\{1 - \tanh\left[\left(\frac{p_0}{N_{0,ehh}}\right)^{0.63}\right]\right\} \tag{3.31}$$

$N_{0,eeh} = 3.3 \cdot 10^{17}$ cm^{-3} and $N_{0,ehh} = 7.0 \cdot 10^{17}$ cm^{-3}, for Si [54]. B_{low} is the radiative recombination coefficient for lowly doped silicon and B_{rel} is the relative radiative recombination coefficient. For B_{low} the measured value by Trupke [59] were inpterpolated and extrapolated, according to the cell temperature. The measured values are in Table 3.3.

For B_{rel}, the equations by Altermatt are used [60]:

$$B_{rel} = \frac{B}{B_{low}} = \frac{b_{max} - b_{min}}{1 + \left(\frac{n+p}{2 \cdot b_1}\right)^{b_2} + \left(\frac{n+p}{2 \cdot b_3}\right)^{b_4}} \tag{3.32}$$

Table 3.3: B_{low} values for Si, measure by Trupke [59].

Cell temperature (K)	**B$_{low}$ (cm^{3}s^{-1})**
77	$8.01{\cdot}10^{-14}$
90	$4.57{\cdot}10^{-14}$
112	$2.14{\cdot}10^{-14}$
170	$8.84{\cdot}10^{-15}$
195	$7.35{\cdot}10^{-15}$
249	$5.48{\cdot}10^{-15}$
300	$4.73{\cdot}10^{-15}$

In which:

$$b_{min} = r_{max} + \frac{r_{min} - r_{max}}{1 + (T_c / r_1)^{r_2}} \tag{3.33}$$

$$b_1 = s_{max} + \frac{s_{min} - s_{max}}{1 + (T_c / s_1)^{s_2}} \tag{3.34}$$

$$b_3 = w_{max} + \frac{w_{min} - w_{max}}{1 + (T_c / w_1)^{w_2}} \tag{3.35}$$

In Table 3.4 the values for Equation 3.32 to 3.35 are given. These values are valid for Si, for a temperature range from 77K to 400K and an injection range from 10^{11}cm^{-3} to 10^{19} cm^{-3} [60].

Table 3.4: B_{rel} parameter values [60]

Parameter	**Value**	**Parameter**	**Value**	**Parameter**	**Value**
b_{max}	1.00	r_1	320	s_2	3.00
b_2	0.54	r_2	2.50	w_{max}	$4.0{\cdot}10^{18}$
b_4	1.25	s_{max}	$1.5{\cdot}10^{18}$	w_{min}	$1{\cdot}10^{9}$
r_{max}	0.20	s_{min}	$1{\cdot}10^{7}$	w_1	365
r_{min}	0.00	s_1	550	w_2	3.54

To account for photon recycling (PR), the radiative recombination coefficient ($B_{rel} \cdot B_{low}$) is multiplied by (1-P_{PR}). The probability of PR, P_{PR}, is determined by

$$P_{PR}(W, n_r, p) = \frac{\int_0^\infty A_{bb}(E, W, n, p) \cdot B(E) dE}{\int_0^\infty B(E) dE} \tag{3.36}$$

A_{bb} is the relative absorbance:

$$A_{bb} = \frac{\alpha_{bb}(E)}{\alpha_{bb}(E) + \alpha_{FCA}(E) + \frac{1}{4n_r^2 W}} \tag{3.37}$$

α_{bb} and α_{FCA} are the absorption coefficients for band-to-band (bb) transitions and free carrier absorption (FCA) and n_r is the refractive index. Parameter values by Green [61] are used for α_{bb} and n_r. The wavelengths range of the table is from 250 to 1450 nm. The values given are for 300K, but temperature coefficients are available to extrapolated the parameters to the matching temperature, like show in Equation 3.38.

$$x(T_c) = x(T_0) \cdot \left(\frac{T_c}{T_0} \right)^{C_x(T_0) \cdot T_0} \tag{3.38}$$

x is the parameter to be extrapolated, C_x is the temperature coefficients of this parameter and T_0 is the temperature of the tabulated values, 300 K in this case[61]. Rüdiger's [62] expressions for α_{FCA} are used.Equation 3.39 for an n-type cell and Equation 3.40 for a p-type cell.

$$\alpha_{FCA,n} = 1.8 \cdot 10^{-18} \cdot \lambda^{2.6} \cdot n \tag{3.39}$$

$$\alpha_{FCA,p} = 2.6 \cdot 10^{-18} \cdot \lambda^{2.4} \cdot p \tag{3.40}$$

These equations are valid for the wavelength range λ = 1000–2000 nm. FCA in Si can be neglected for wavelengths λ < 1000 nm [62]. B is the spectrally resolved radiative recombination coefficient:

$$B(E) = \frac{1}{\pi^2 c^2 \hbar^3 n_{i,eff}^2} n_r^2(E) \cdot E^2 \cdot \alpha_{bb}(E) \exp\left(-\frac{E}{k_B T_c}\right) \tag{3.41}$$

$\hbar$ is the reduced Planck's constant (which is $h/2\pi$). The current density J_L is integral of the spectral photon flux Φ^i (can be obtained using Equation 3.18) and the relative absorbance, A_{bb}.

$$J_L = \int_0^\infty A_{bb}(E)\Phi^i(E)dE \tag{3.42}$$

For this model the narrow base assumption is used. This assumption states that the minority carrier diffusion length, L_B, is much smaller that the width of the base region of the cell, W_B. Figure 3.3 is a basic sketch of a PV cell. The diffusion length can be interpreted as the length minority carriers can travel before recombine [47]. Thus in other words the narrow base assumption means that all minority carriers created at the emitter, will reach the rear contract.

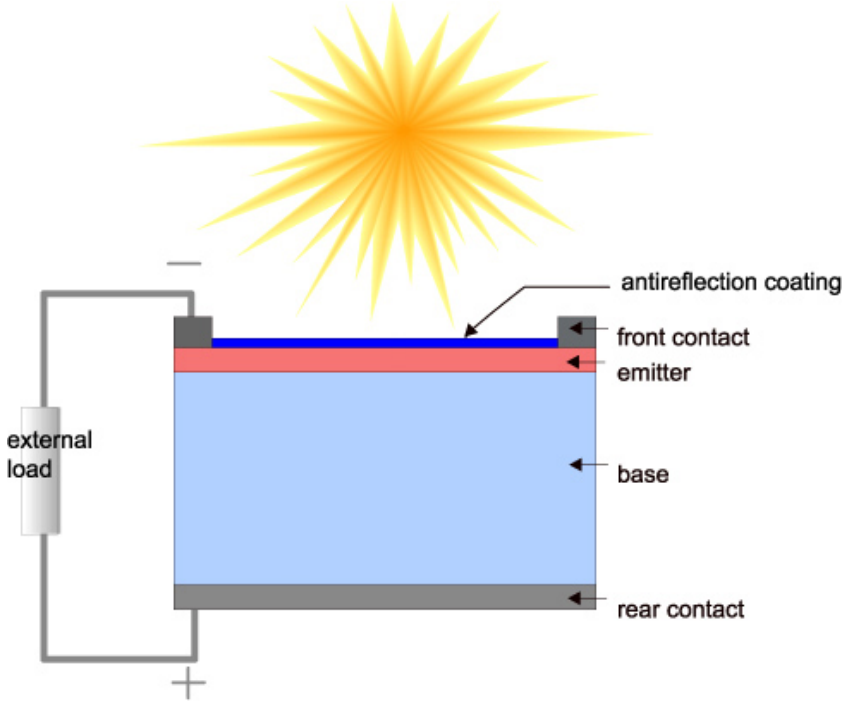

Figure 3.3: Basic sketch of a PV cell [63].

4

Validation

4.1. Validating Detailed balance model

The results of the Detailed balance code are compared to the the results of Rühle [12], under AM1.5 spectrum and temperature of 25 °C, for bandgaps of 0.4 to 4.3 eV. The results of the validation are shown in Figure 4.1. It can be seen that all variable match the data, concluding that the code for the top layer works correctly.

4.2. Validating Richter-model

The results of the Richter[6] model are given in contour plots with on the x-axis the cell thickness and on the y-axis either electron- (for n-type) or hole equilibrium concentration (for p-type)). These plots where created using `contourf` and `contour` for a filled contour plot with lines at the same values as in the paper. The simulations where run for concentrations of 10^{12} to 10^{17} cm^{-3}, every step the input is multiplied by 10^1. And for thicknesses 1, 2, 5, 10, 20, 50, 100, 200, 500 and 1000 μm. Richters plots for n-type and p-type Si are depicted in Figure 4.2 and Figure 4.3. The right upper corner is white, because the narrow base assumption (diffusion length » base thickness) is not valid here. The results from the Matlab calculation are given in 4.4 and 4.5. For both types, the overall shape is similar but the values are slightly different. The most visible differences are that the efficiency and voltage are higher and the FF is lower. One of the reasons for this, is the absence of band gap narrowing (BNG). As explained in chapter 3, BGN has a small effect [54] on the result.To examine the effect of BGN, the verification was also done with a constant BNG of 1% of the bandgap energy. The results of this, for n-type and p-type, are depicted in Figure 4.6 and 4.7. Adding constant BGN decreases both efficiency and voltage, proving that it influences the performance negatively, as it should. Still there is a small difference between the paper and the Matlab calculation. The reason for this is unknown. But nonetheless, the values are very similar, concluding that the Matlab code is working correctly.

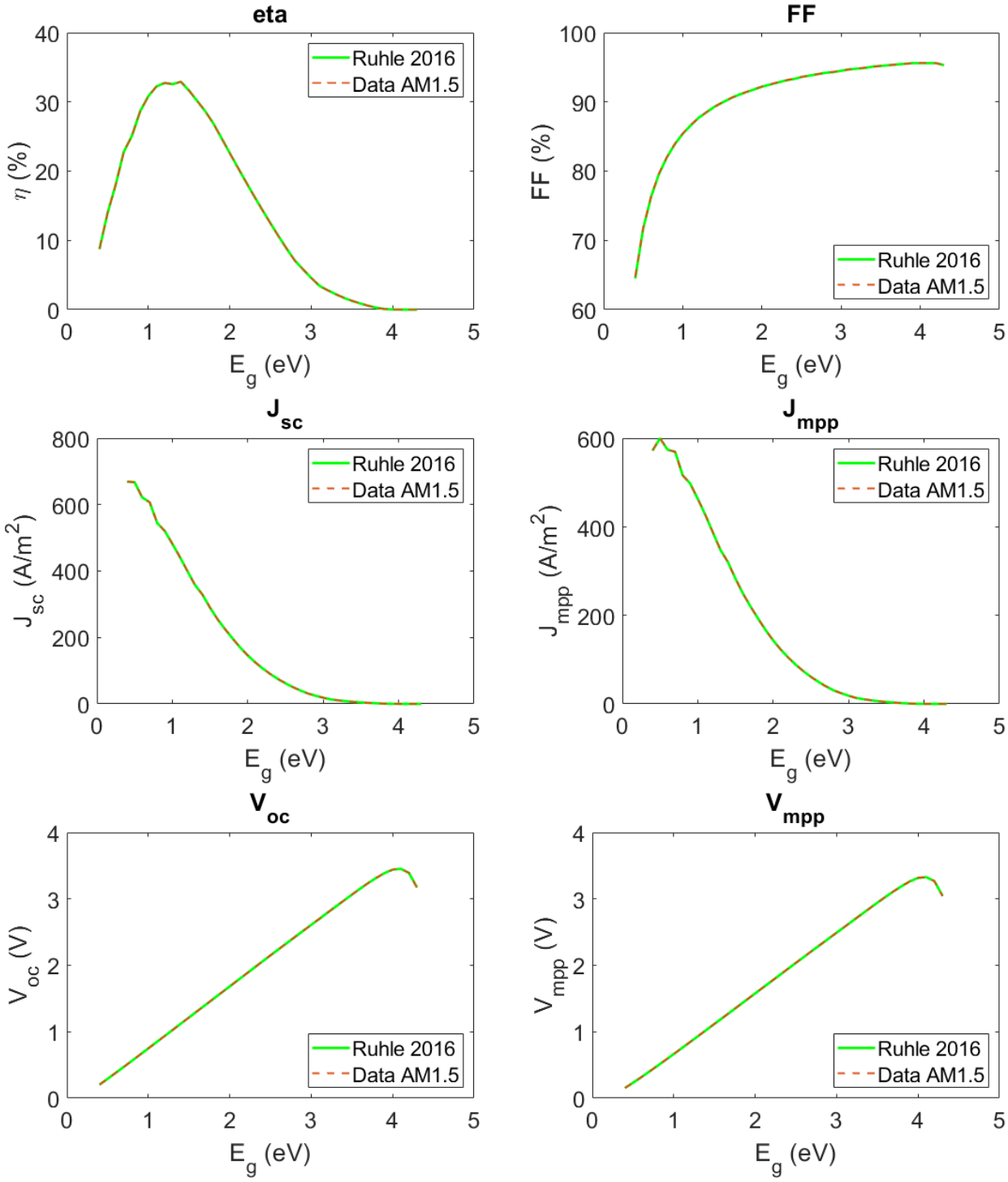

Figure 4.1: Comparison of results from Matlab code and data by Rühle [12] of top-layer variables.

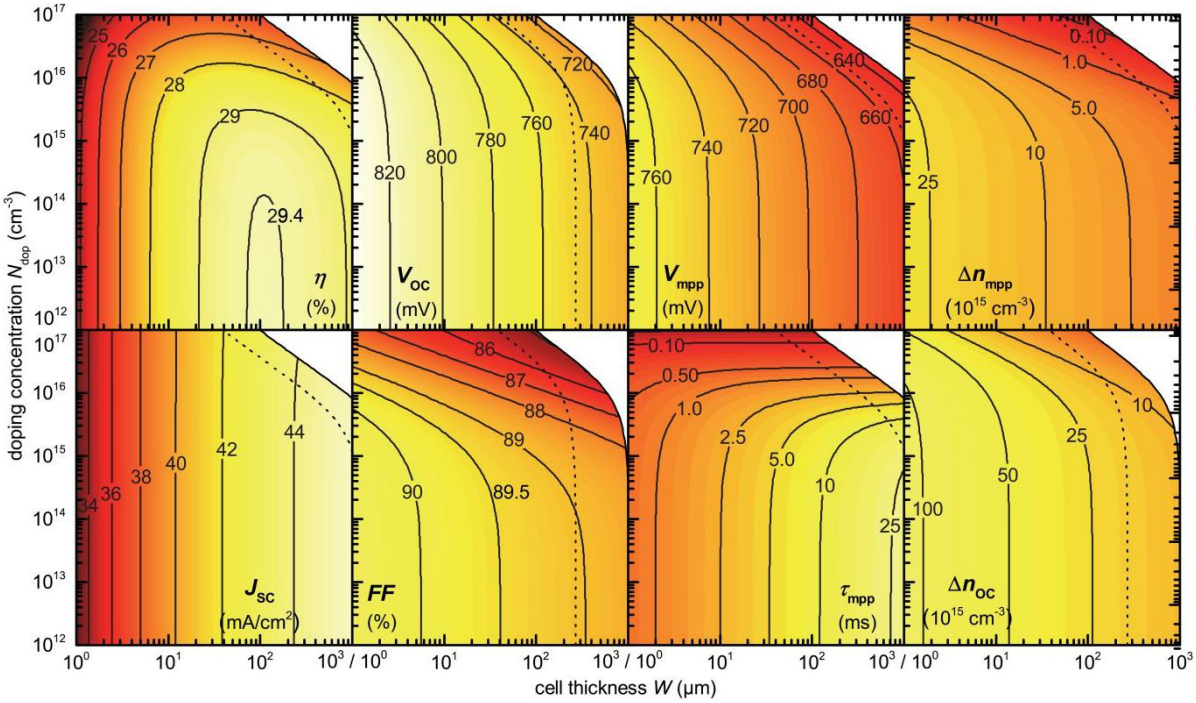

Figure 4.2: Richters values for an n-type Si PV cell [6]

.

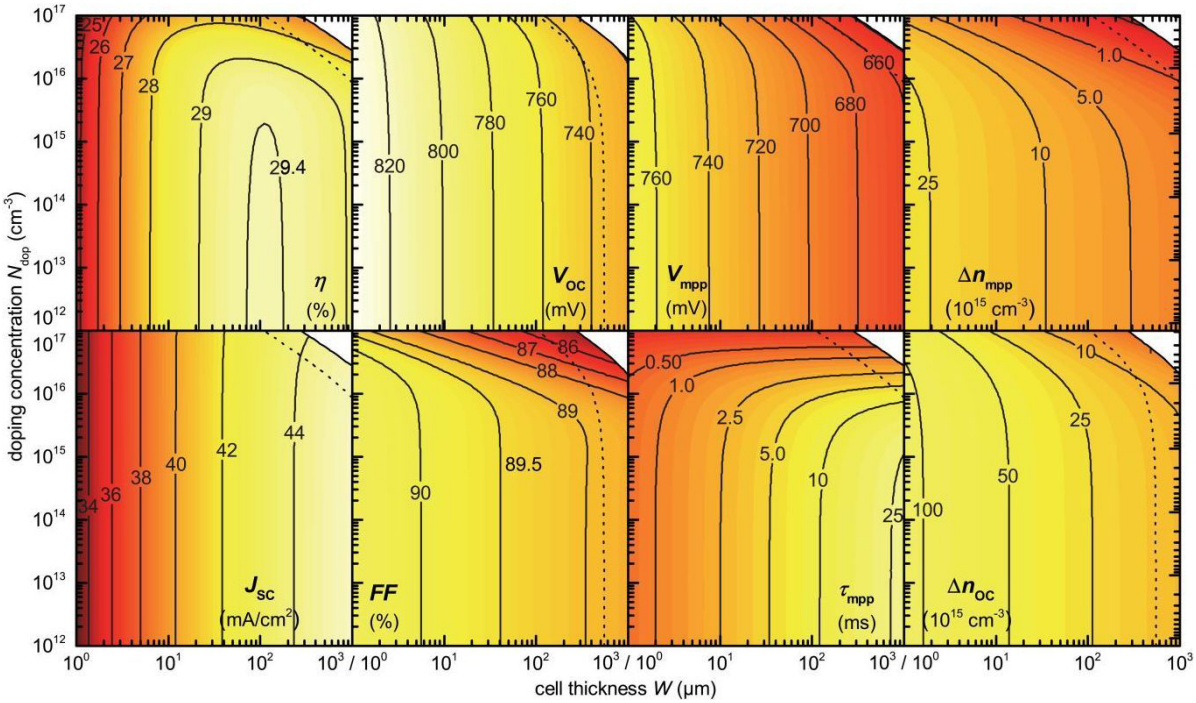

Figure 4.3: Richters values for an p-type Si PV cell [6]

.

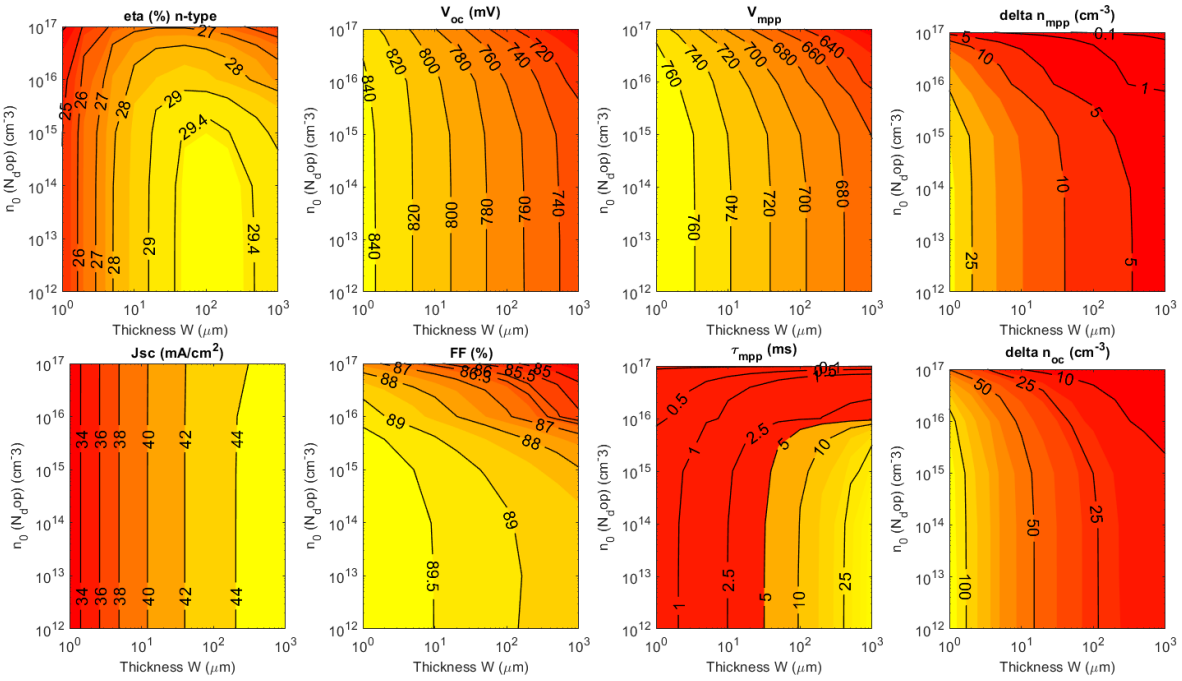

Figure 4.4: Simulated values for an n-type Si PV cell, with BNG = 0

.

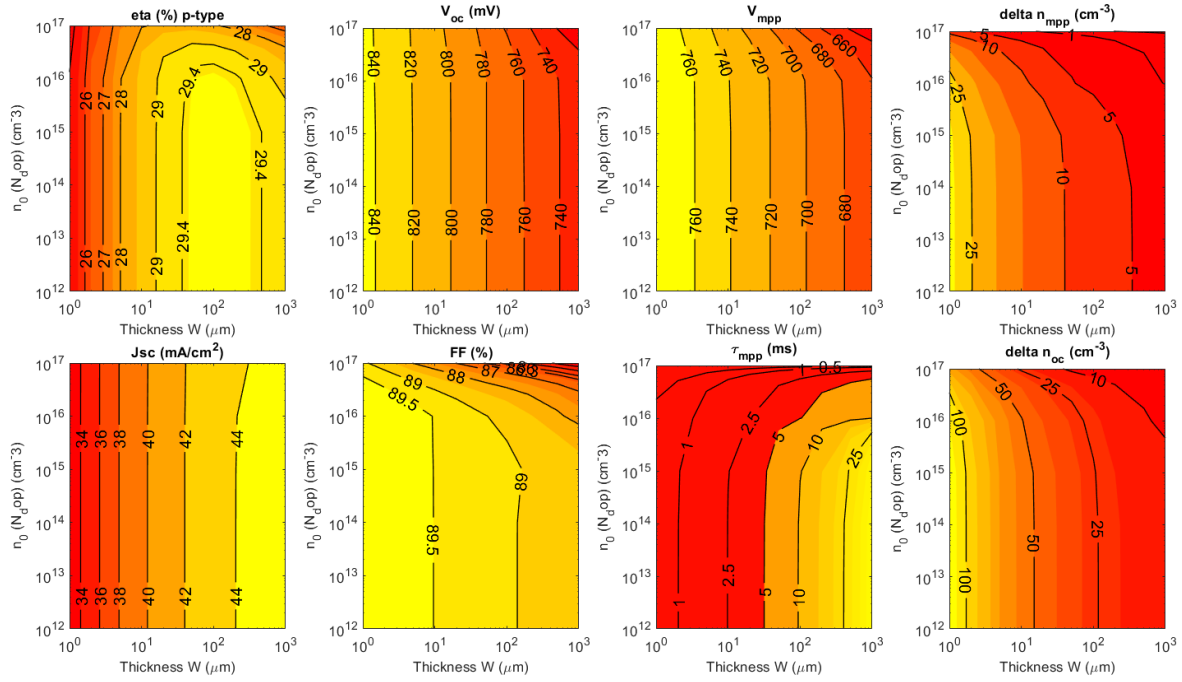

Figure 4.5: Simulated values for an p-type Si PV cell, with BNG = 0

.

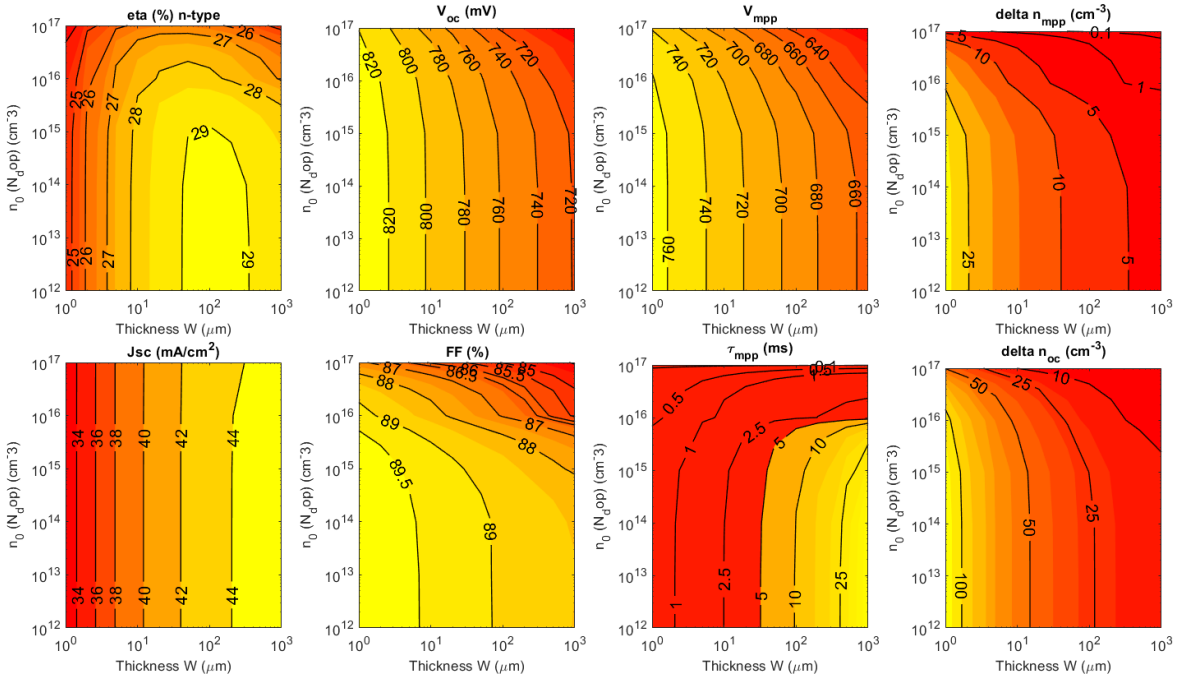

Figure 4.6: Simulated values for an n-type Si PV cell, with BNG = %1 $\cdot E_g$

.

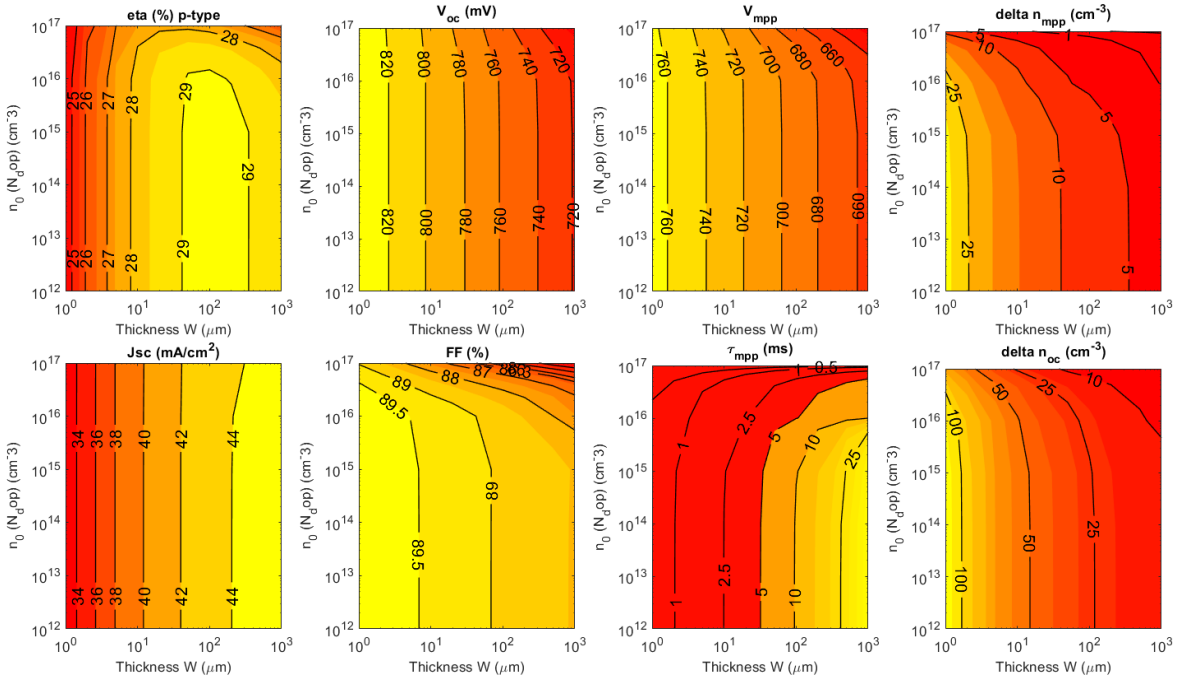

Figure 4.7: Simulated values for an p-type Si PV cell, with BNG = %1 $\cdot E_g$

.

5

Results

Based on the methodology in chapter 3, in this chapter results are shown in four part. The worldwide GHI which was used as input, single junction Si, 2-junction Perovskite-Si, and the relation between the optimal top-bandgap and bottom-thickness are all visualised and discussed.

5.1. GHI map

In Figure 5.1 the integrated average GHI spectrum is depicted and Figure 5.2 shows the average Initial Surface Shortwave Down Flux from NASA's CERES. The global distribution of high and low irradiance simulated by SMARTS is overall realistic and in good agreement which the CERES data. In the northern hemisphere in the simulated irradiance a chessboard pattern is visible(above 30 °). Maps of the average input data can be found in Appendix A. Although non of the maps show this pattern strongly, the combination of all input data could be the reason for this pattern in the end result. The simulated irradiance in north Africa and the Middle East is significantly lower than the irradiance data. After inspecting all average input data maps, it is most likely caused by the aerosol optical depth (AOD) data. In Figure 5.3 this data is depicted.

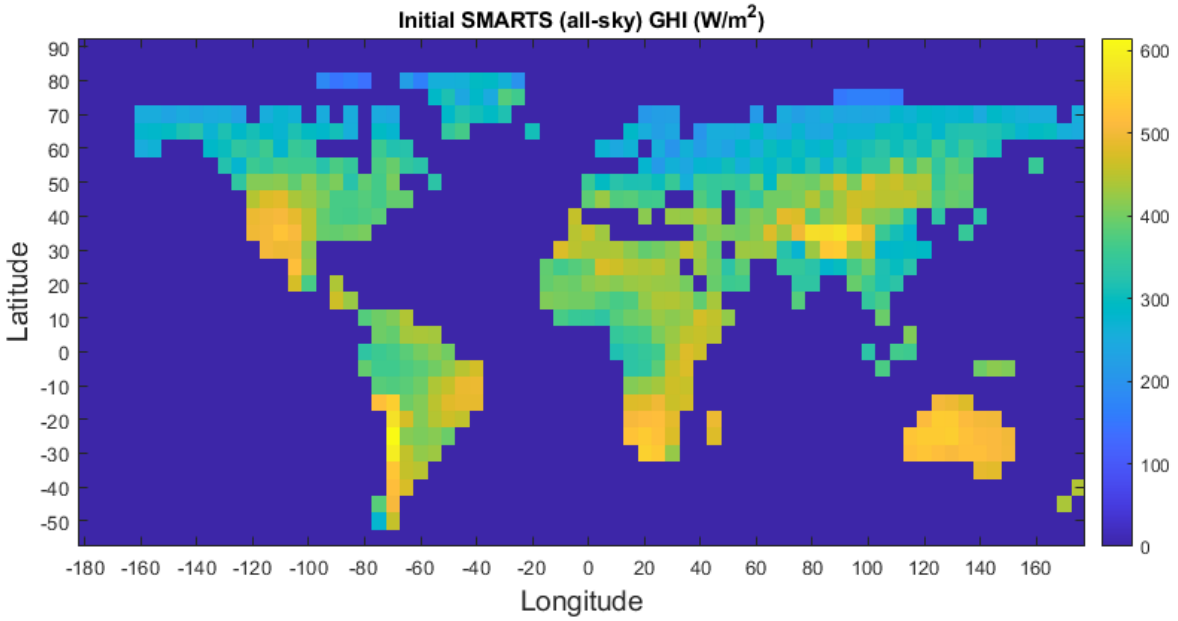

Figure 5.1: Initial GHI from SMARTS, after applying BRL model. The irradiance ranges from 141 to 615 W/m^2

AOD is a measure of how much sunlight is prevented from reaching the ground due to small particles like dust and smoke. A low AOD value means the atmosphere is very clean, values above 0.4 correspond to very hazy conditions [65]. In the AOD map it can be seen that at the west side of north Africa and in the Middle

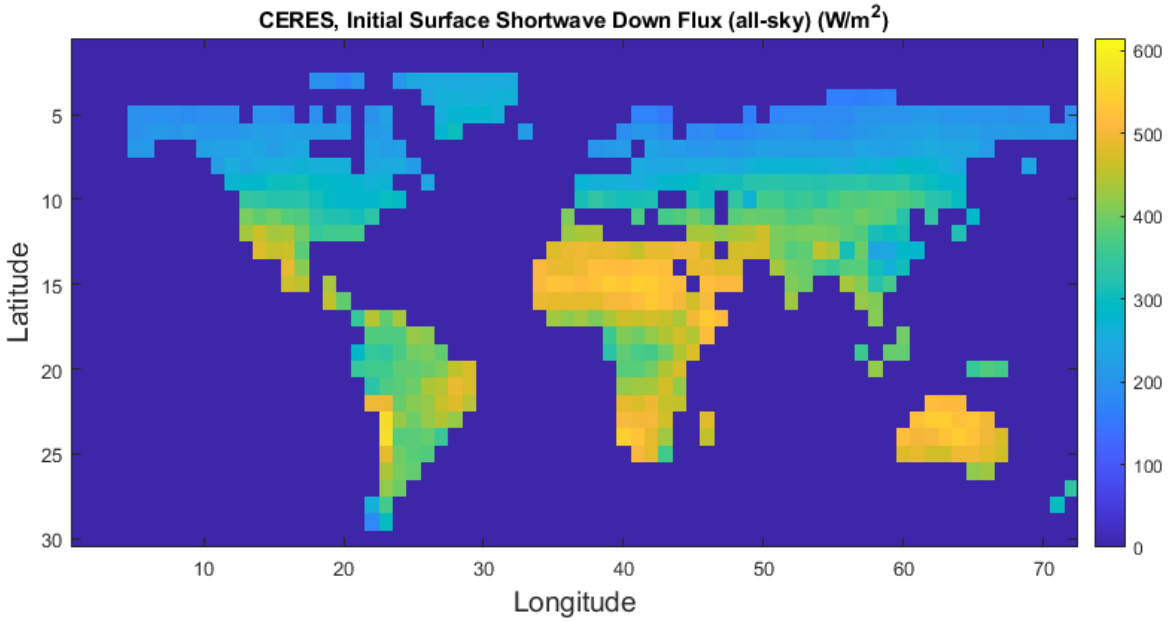

Figure 5.2: CERES Initial Surface Shortwave Down Flux (all-sky). Downward or Downwelling irradiation is the irradiation from the sun coming down to the earth's surface and upward irradiation comes from reflection at the surface[64]. The irradiance ranges from 154 to 572 W/m^2. SYN1deg uses 18 spectral bands from 175 to 4000nm[27].

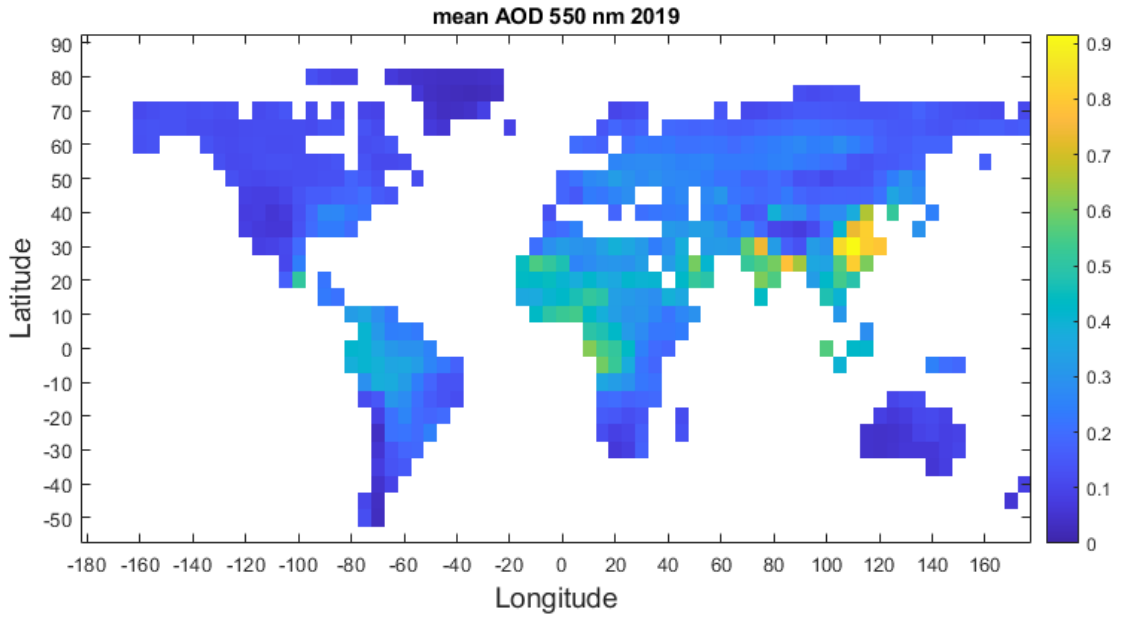

Figure 5.3: Yearly average aerosol optical depth data for 550 nm.

East AOD values are elevated at the same locations as where in the SMARTS GHI maps, the irradiance is lower than expected. Since dust storms originate in arid and semi-arid regions, in particular the Sahara and the Middle East [66], and the Middle East is one of the regions worldwide most affected by dust, next to Africa, [67], an elevated AOD can be expected. Still these regions have a high GHI [68], like the average GHI data from CERES shows in Figure 5.2. Because another complete data set for AOD could not be found, it was decided to normalise the simulated GHI spectra, using the CERES surface flux data. The new integrated values are exactly the same as the average CERES data. And thus the map after normalisation is not shown. The AOD effects the blue part of the spectrum more than the red part(see Figure 5.4)> Normalisation is a quick fix, but no long term solution, since the red part of the spectrum, which is mostly not absorbed is increased or

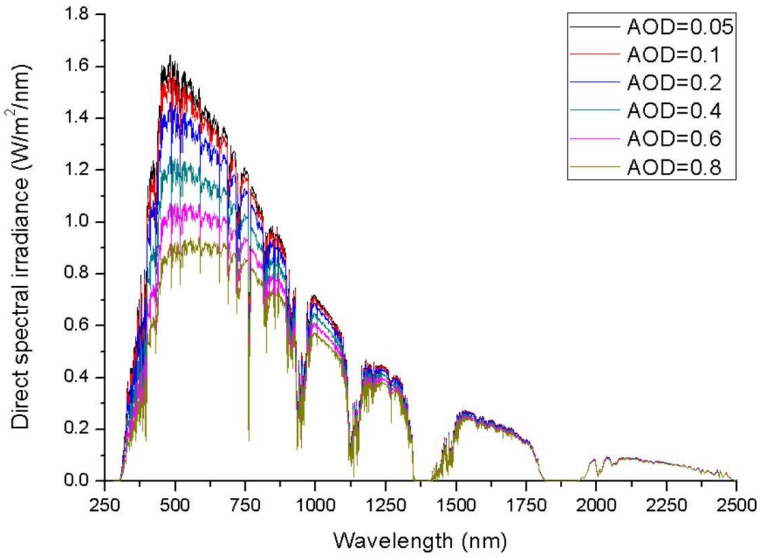

Figure 5.4: Effect of increasing AOD on light spectrum. [69]

decreased as well and this will effect the efficiency. In Figure 5.5 the normalisation factors are depicted. The maximum normalisation factor is 1.480, the minimum is 0.625 and the average is 0.915.
Apart from irradiance, the ambient temperature, is used by the models for both absorber layers. In Figure 5.6

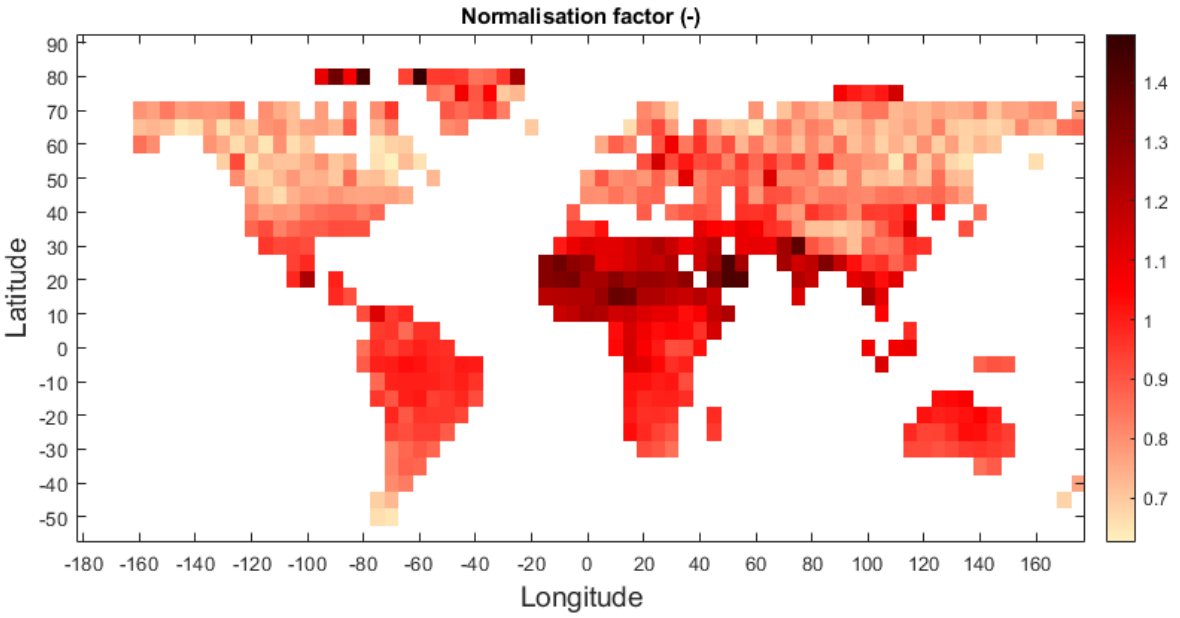

Figure 5.5: Normalisation factors. The factors range from 0.625 to 1.480.

the yearly day-time average ambient temperature data is depicted in a map.

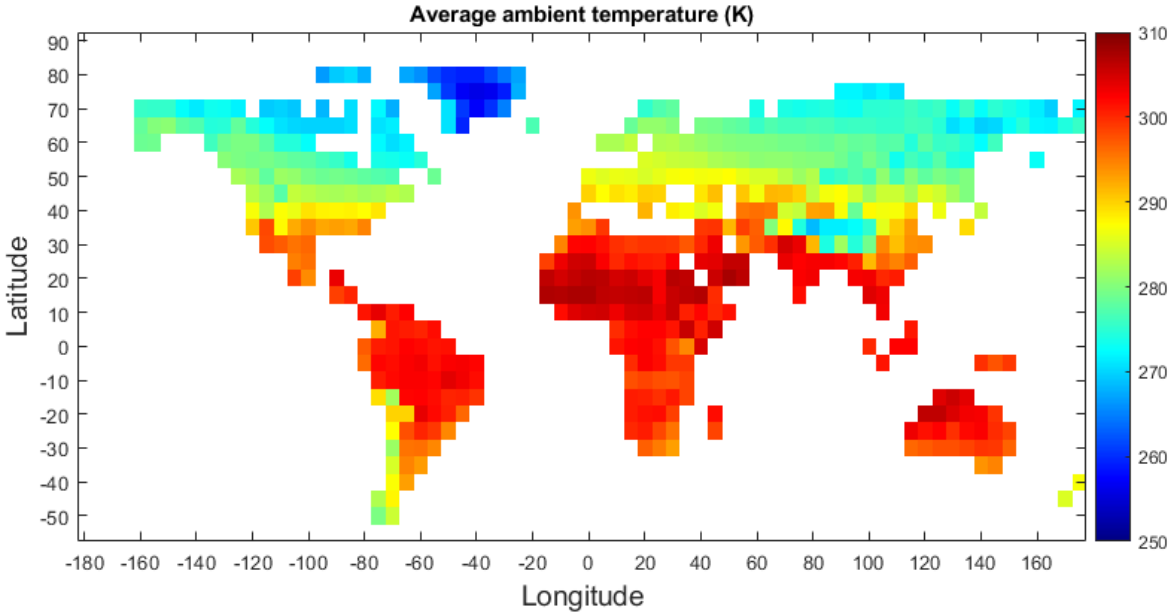

Figure 5.6: Day-time average ambient temperature for 2019. The range is 256 to 308 K.

5.2. Si single-junction results

In this section the local result from the Richter model [6] for a single-junction Si cell are shown. In Figure 5.7 the optimal cell thickness around the world is shown. To make differences better visible, the range of the color bar is 70-500 μm. The thinnest cell is 70 μm and the maximum thickness is 870 μm. The thickness distribution is depicted in Figure 5.8.

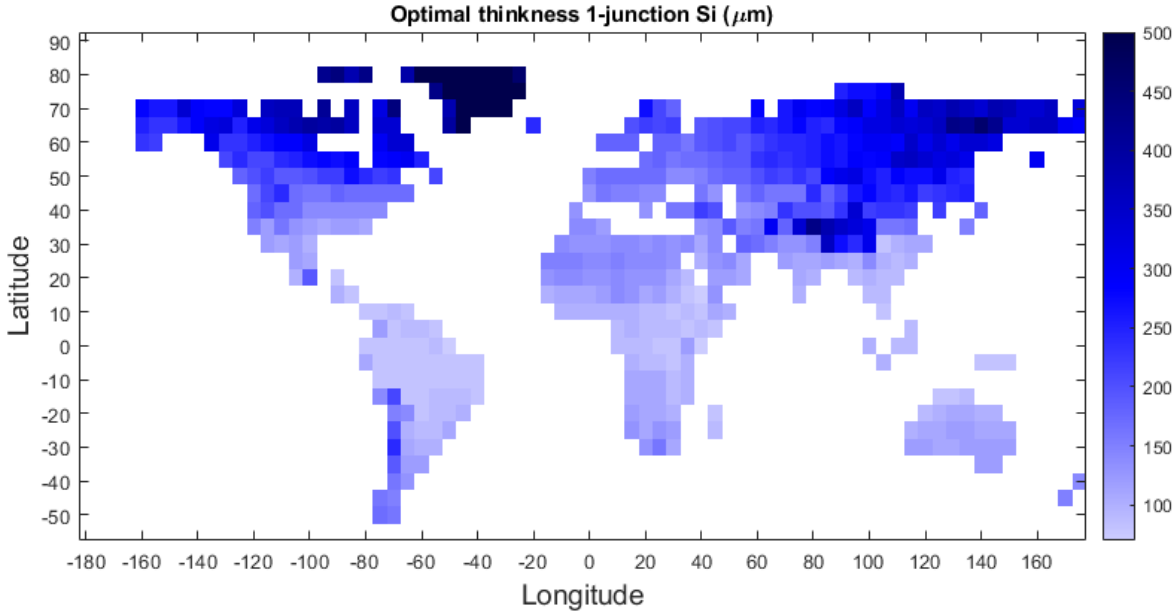

Figure 5.7: Optimal thickness of Si for a single junction. The minimum thickness is 70 μm and the maximum is 870 μm

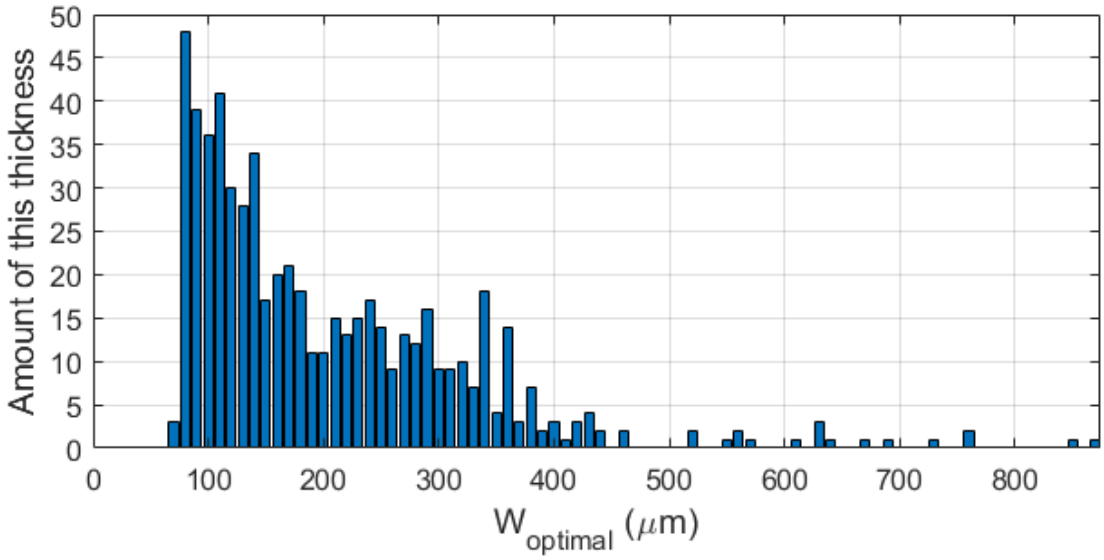

Figure 5.8: Thickness ditribution for single junction Si. As maximum there are 48 locations with an optimal thickness of 80 μm.

It is favorable that the optimal thickness is close to most PV modules. Assuming more PV is present in high irradiance areas than in lower irradiance areas, the average thickness should shift to the thickness of locations where most PV is installed or likely will be. The irradiance weighted average thickness takes this into account. The irradiance weighted average is calculated using Equation 5.1.

$$W_{opt,irr\_weighted\_avg} = \frac{sum(W_{opt} \cdot GHI)}{sum(GHI)} \tag{5.1}$$

The average optimal cell thickness is 205 μm and the irradiance weighted average is 165 μm.
In Figures 5.9 and 5.10 the annual yield and efficiency are depicted. The mpp power, voltage and current can be found in Appendix B, in section B.1. The yield ranges from 199 to 733 kWh/m^2 and the average is 440 kWh/m^2. Peters et al. [10] yield for Si, **??**, ranges from 205 to 820 kWh/m^2. Since they used the detailed balance model, which does not take into account Auger losses, their higher yield is understandable. The areas of high an low irradiance are in good agreement with the map from this project. Areas such as Chile yield high as expected, because of their high irradiance and low temperature.

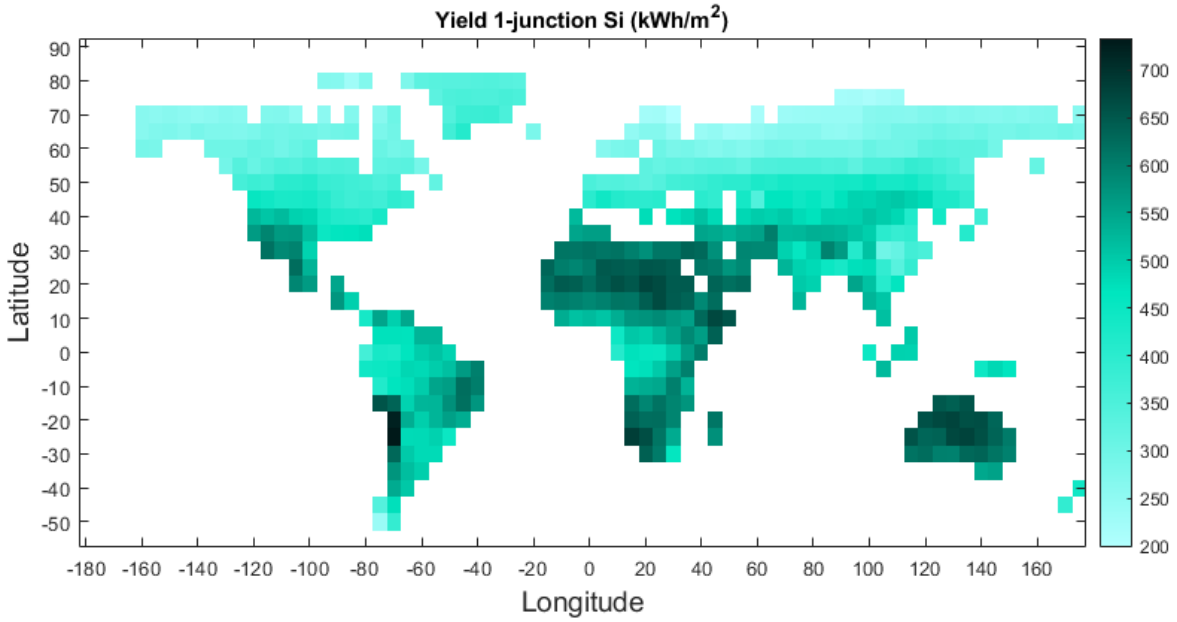

Figure 5.9: Single junction Si annual yield. The values range between 199 and 733 kWh/m^2.

The efficiency ranges from 27.22 to 31.03 %. The average is 29.06 %, which is slightly lower, but close to the theoretical limit (under STC) of 29.43 %. The irradiance weighted average efficiency is 28.88 %. The efficiency is lowest in Africa and Middle East where both the GHI has been increased by normalisation and the temperature is very high.
To see if either the optimal thickness, the efficiency or both are related to the temperature or GHI, the variables were plotted and the result is visible in Figure 5.11.

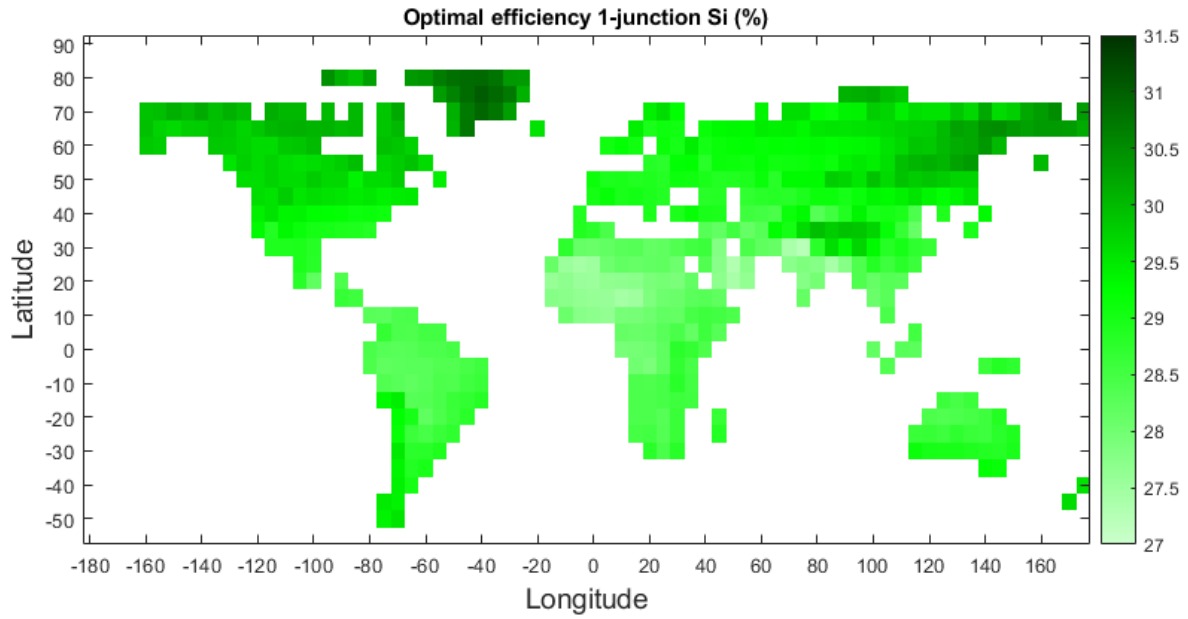

Figure 5.10: Single junction Si optimal efficiency. It ranges from 27.22 to 31.03 %

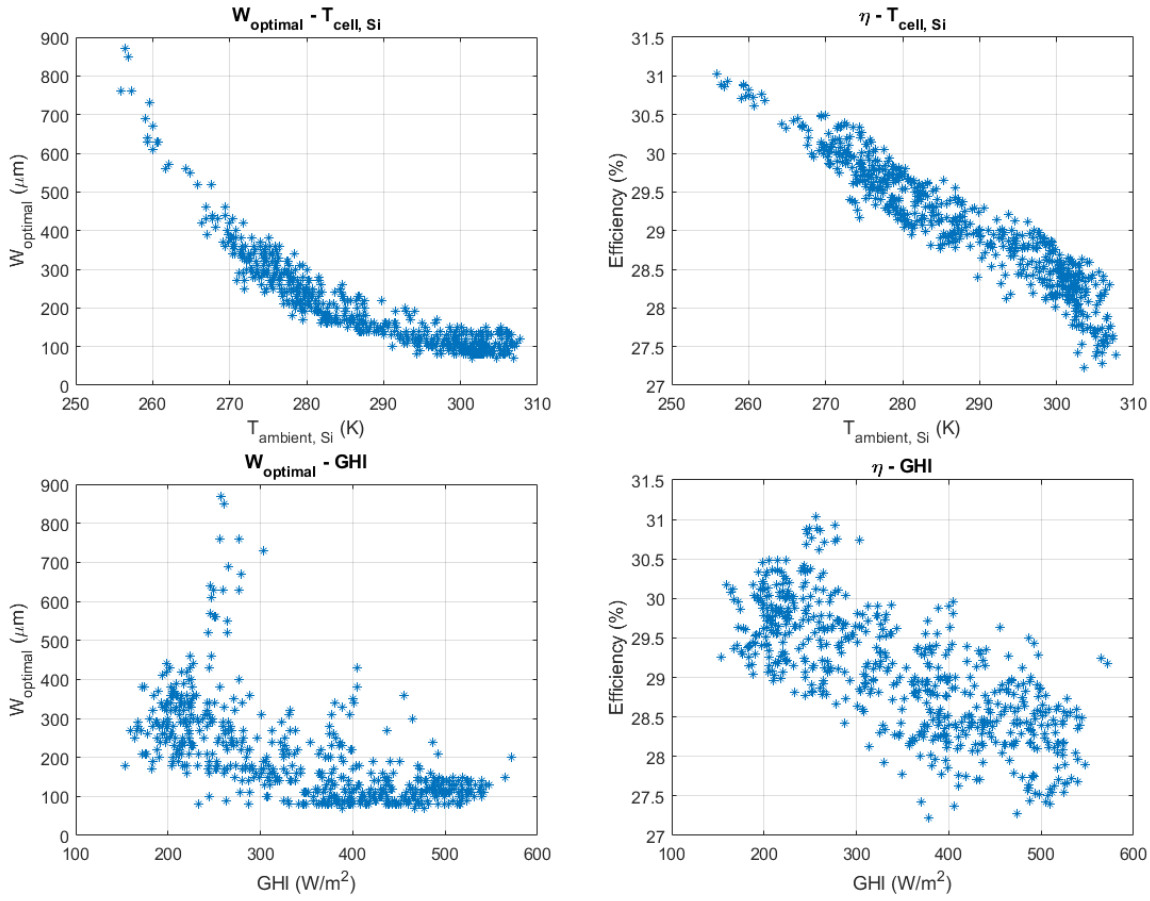

Figure 5.11: Plots of optimal thickness vs. temperature and GHI (left) and efficiency vs. temparature and GHI(right).

Both thickness and efficiency are highest for the lowest temperatures and GHI values. Both are stronger related to the temperature than to the GHI. The first plot of the optimal thickness as a function of temperature is interesting, a relation is visible which can give an indication of the design parameter thickness based of local average temperatures. A function was fitted to express this relation. The fit, Equation 5.2, is depicted in Figure 5.12.

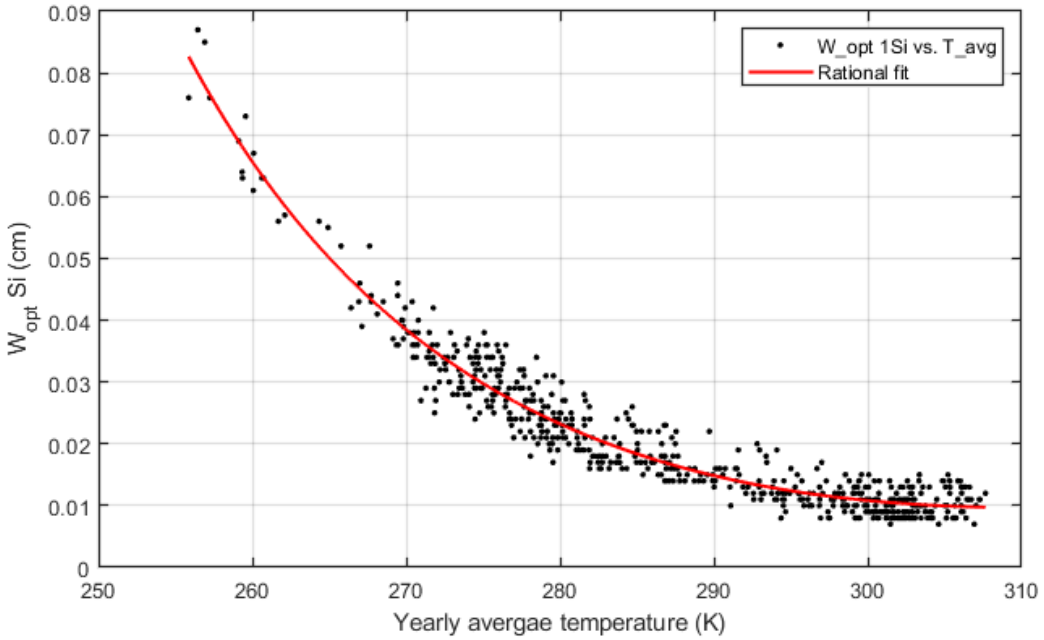

Figure 5.12: Plots of optimal thickness and efficiency against temperature and GHI.

$$W_{opt,fit}(T_a) = \frac{9.092 \cdot 10^{-4} \cdot T_a^2 - 0.5586 \cdot T_a + 85.3}{T_a - 219.3} \tag{5.2}$$

The R-square values is 0.9419. R-square is a measure of how much of the variation can be explained by the model's inputs [70]. The R-square value of a fit should be as close to 1 as possible.
Since not all locations with the same average temperature, receive the same amount of irradiance, a contour plot is a useful tool to quickly look up how thick a single Si absorber should be, based on the local average GHI and ambient temperature combination. In Figure 5.13 the available GHI - $T_{ambient}$ combinations are depicted and in Figure 5.14 the resulting contour plot is shown. `griddata` was used to interpolate the scattered data.

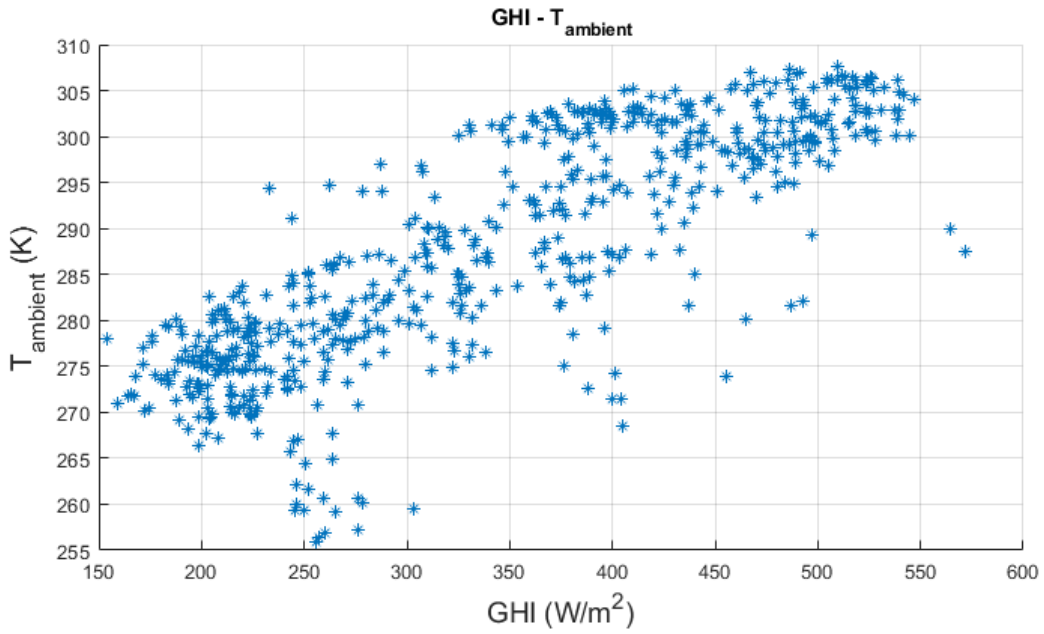

Figure 5.13: All combinations of GHI and ambient temperature.

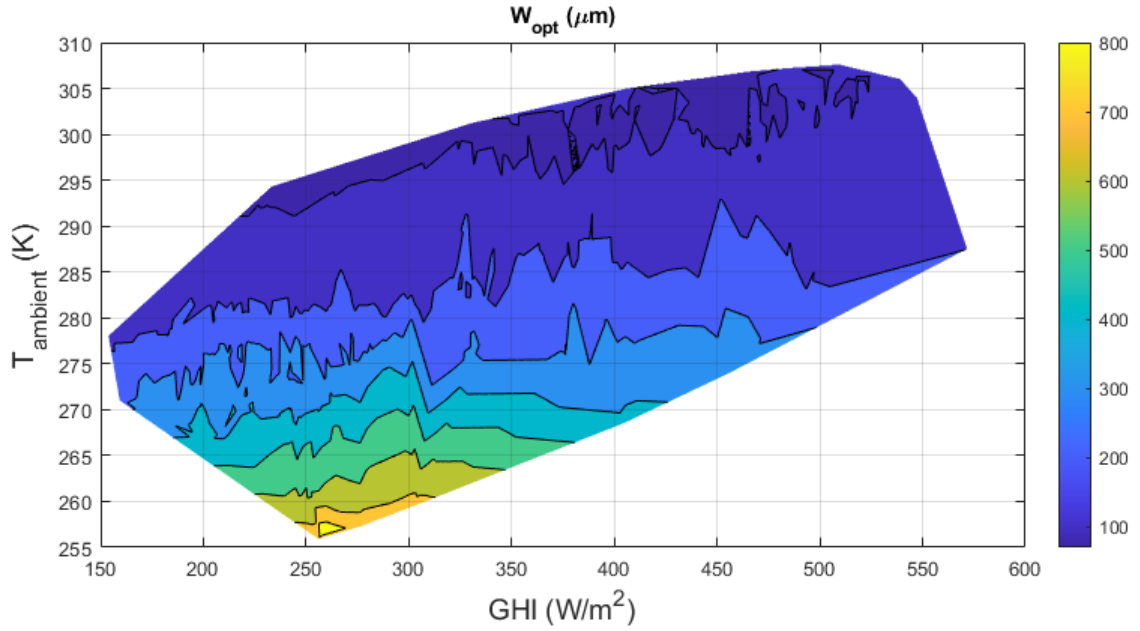

Figure 5.14: Plot and fit of optimal thickness of Si for a single junction.

5.3. 2-junction Perovskite-Si results

In this section the results for optimal thickness and performance of the double junction Perovskite-Si are presented. The bandgap used for Perovskite is 1.72 eV. The optimal thickness of Si was determined using current matching. In Figure 5.15 the optimal thickness is depicted. The maximum thickness of the color bar is limited to 500 μm. Figure 5.16 is the thickness distribution. The y-axis is limited to 40, to make the small amounts better viable. Two locations exceed this number: there are 42 locations with a thickness of 10 μm and 96 with a thickness of 20 μm. There are 597 locations in total.

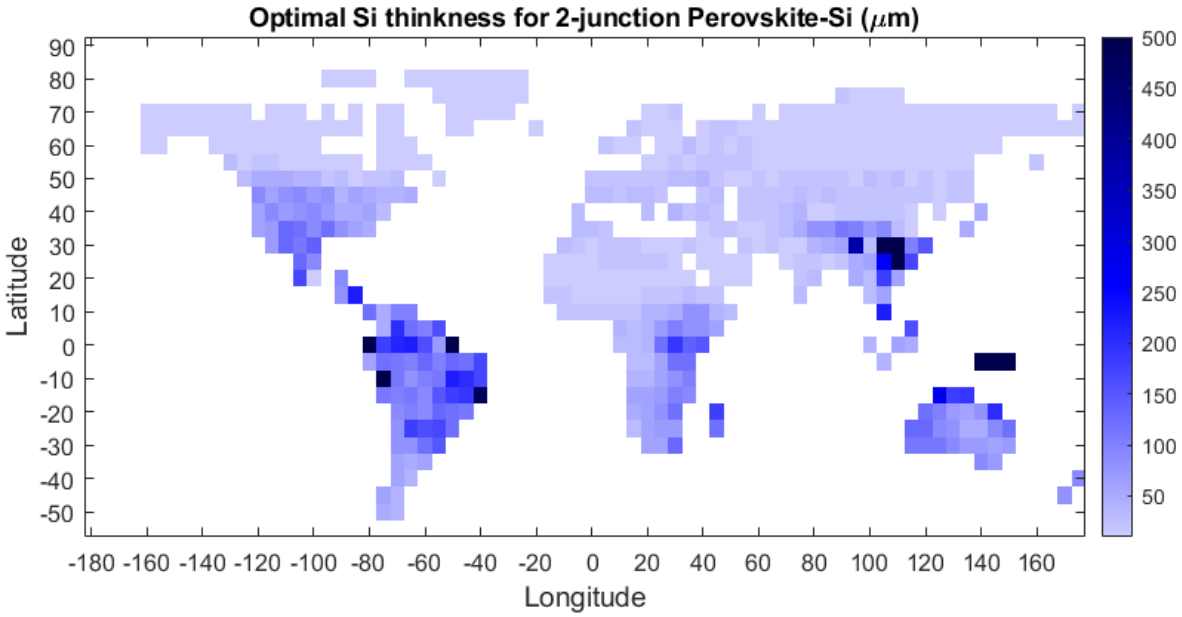

Figure 5.15: Optimal thickness of bottom layer Si, with 1.72 eV Perovskite on top. Current matching is used to determine the optima. The thickness ranges from 10 μ m to 3870 μ m. The average is 77 μm and the irradiance weighted average is 81 μm.

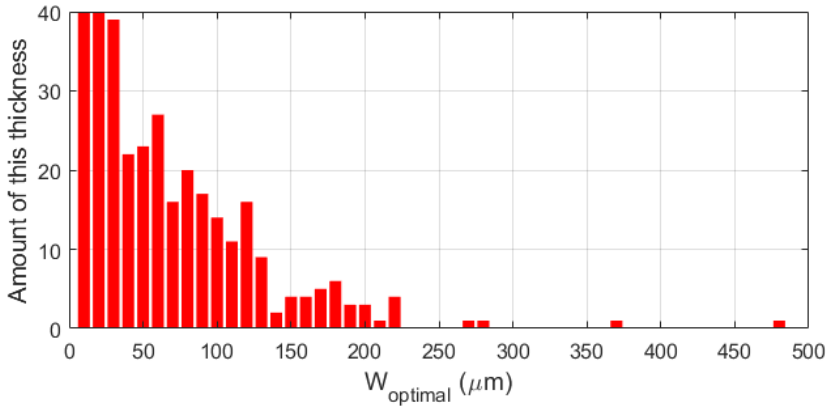

Figure 5.16: Thickness distribution for bottom layer Si in a Perovskite-Si double junction. The x-axis is limited to 500 μm and y-axis to 40, to make the smaller amount better viable. Two thicknesses exceed this number: there are 242 locations with a thickness is 10 μm and 96 with a thickness is 20 μm. The nine thicknesses after 500μm (all occurring ones) are 570, 790, 1280, 1410, 1430, 1720, 4100, 4200 and 4500 μm.

The minimum thickness is 10 μm, this is the lower limit of thickness tried. The maximum thickness is 4500 μm, the average is 77 μm and the irradiance weighted average is 81 μm. There are nine locations where the thickness exceeds 500 μm, in three areas: The north of Latin America, the main land of Southeast Asia and the east of the Malay Archipelago (Indonesia and Papua New Guinea). The thickness values could be related to a difference in the spectrum shape. Therefore the average spectra of the location with the highest thickness

per area and of a nearby low-thickness location where normalised to the AM1.5 spectrum (so the integrated irradiance is 1000 W/m^2) and plotted. The locations are depicted in Figure 5.17. The blue markers are the high-thickness locations and the red are the low-thickness locations.

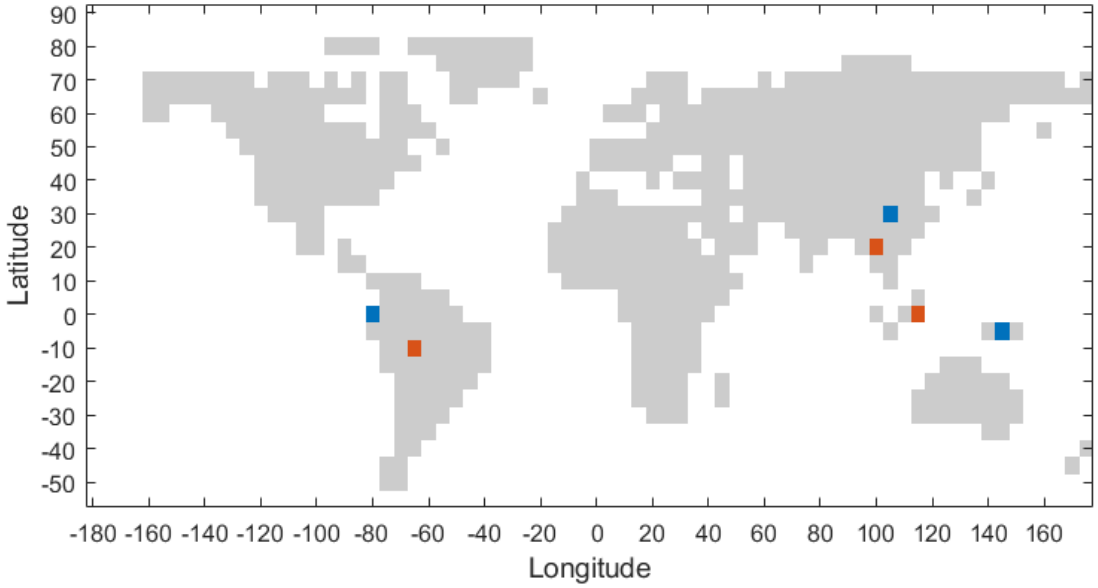

Figure 5.17: Locations of which average spectra where analysed. The blue markers are the high-thickness loactions and the red are the low-thickness locations.

In Figure 5.18, the AM1.5 spectrum is depicted. The yellow part is the part which is absorbed by Perovskite, the red part is absorbed by Si (without Perovskite, Si would absorb both yellow and red part) and the blue part is the rest of the spectrum up to 2500 nm. Irradiance up to 720.8 nm can be absorbed by 1.72 eV Perovskite. And irradiance up to 1107.0 nm can be absorbed by Si.

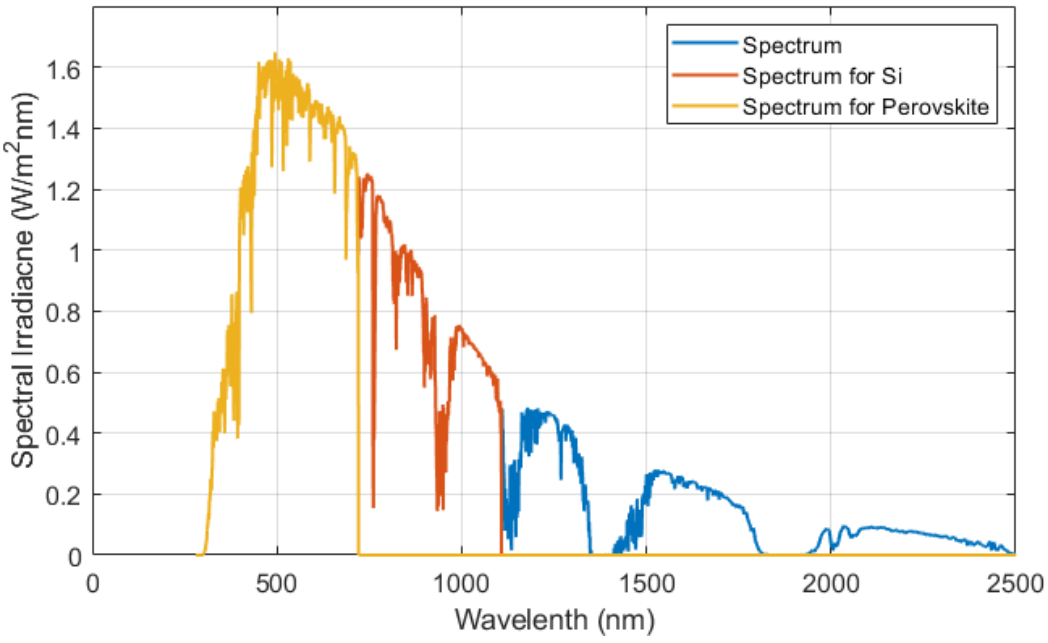

Figure 5.18: AM1.5 spectrum and the parts absorbed by Perovskite(yellow) and Si(red).

In Figures 5.19 to 5.21 the normalised spectra from the three areas are plotted. It can be seen that in all three cases, the spectral irradiance up to ca. 700 nm is higher in the high-thickness spectra than in the low-thickness spectra. Thus as the spectrum shifts to the blue part, the bottom silicon layer has to be thicker. A shift towards the blue part means Perovskite can absorb a higher percentage of the total irradiance and thus can generate a higher current. As a result the thickness of Si has to increase to match that current. Si will also receiving a lower percentage of the spectrum than with a redder spectrum.

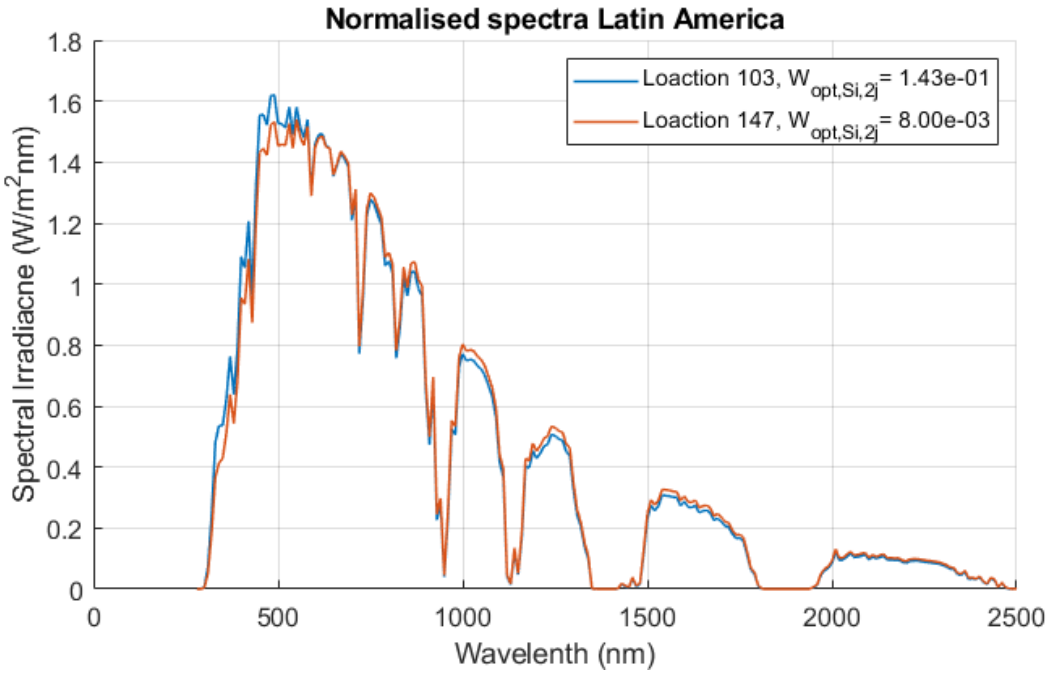

Figure 5.19: Normalised spectrum of the location with the highest thickness and a nearby location with a low thickness in the north of Latin America.

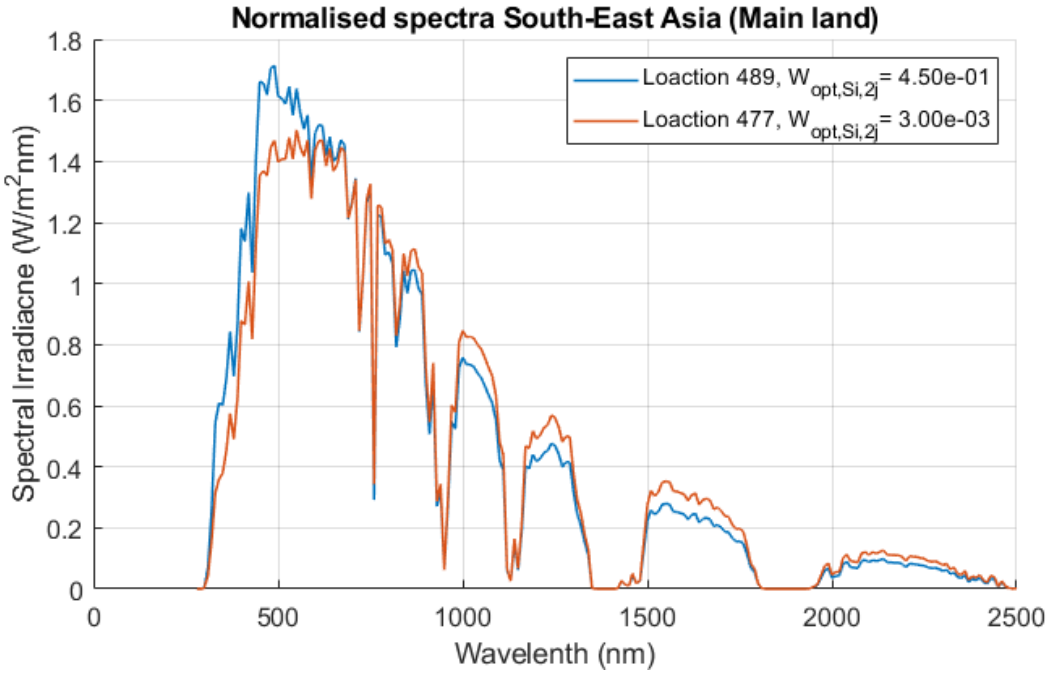

Figure 5.20: Normalised spectrum of the location with the highest thickness and a nearby location with a low thickness in the main land of Southeast Asia.

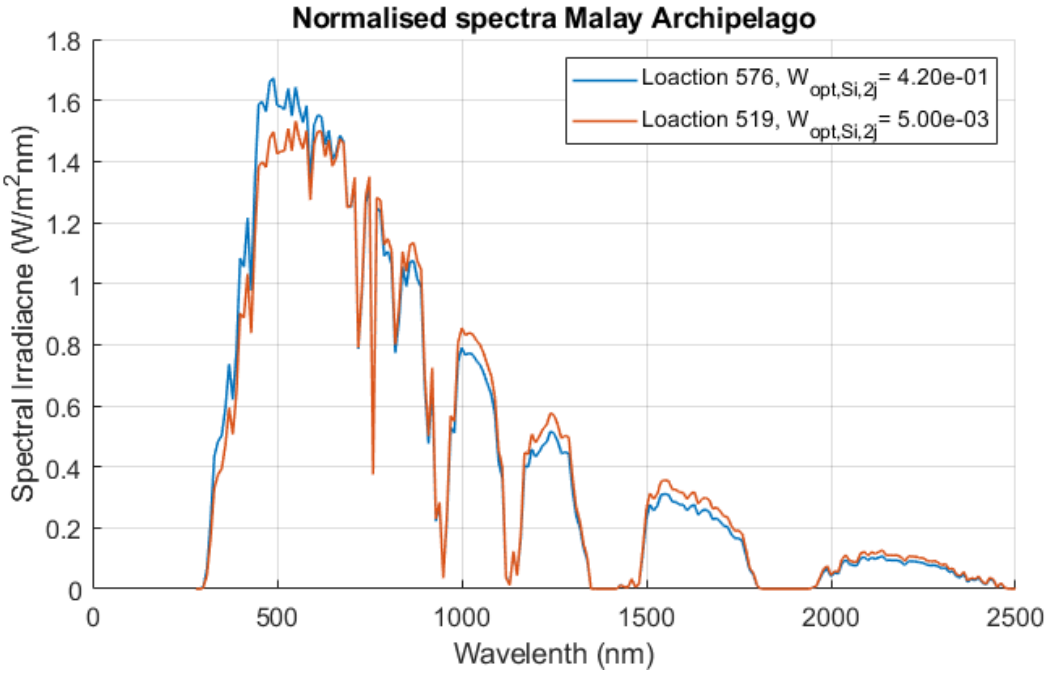

Figure 5.21: Normalised spectrum of the location with the highest thickness and a nearby location with a low thickness in the Malay Archipelago.

To see if a relation could be found between the optimal thickness and the input variable, the optimal thickness was plotted against the ambient temperature, GHI, relative humidity, precipitable water (water in the atmosphere), the altitude and the AOD. In Figure 5.22 the plots are presented. In non of the plots a direct correlation is visible, thus either change in spectrum is caused by a combination of the input variables or by something not considered here. It can be seen in the top left and bottom left plots that the temperate range and altitude range decreases with increasing thickness.

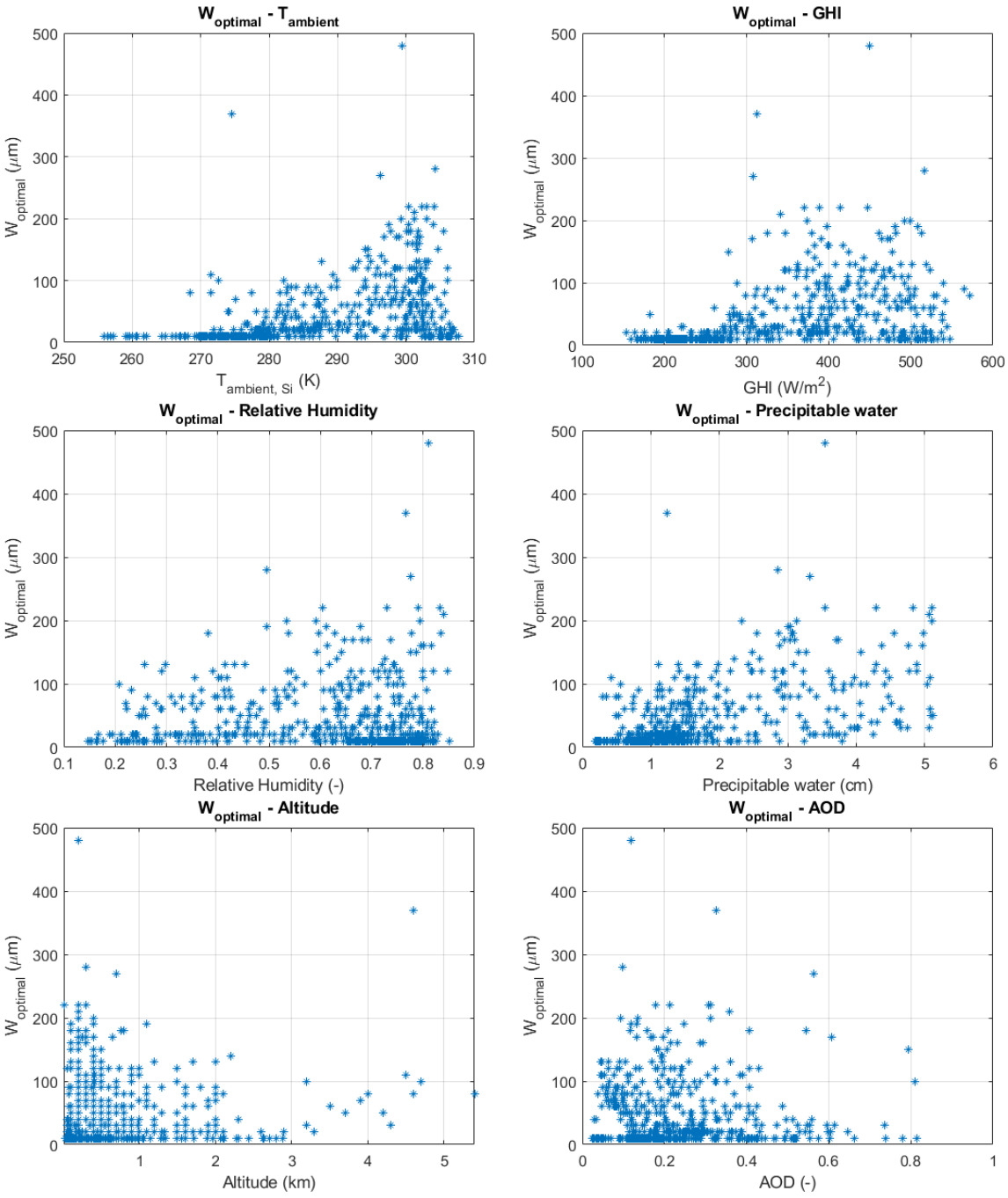

Figure 5.22: Optimal thickness vs. ambient temperature and GHI

The yield is depicted in Figure 5.23. The maximum power point (mpp) power, voltage and current can be found in Appendix B, in section B.2. The yield ranges from 231 to 862 kWh/m^2 and is on average 511 kWh/m^2. The Perovskite bandgap that Liu et al. [11] used in their simulation, is not given. Their reference for EQE, Sahli et al. [71], used 1.6 eV. Because of this comparing the yield values will not insight on the correctness of the results. The global distribution of high and low yield areas is similar.

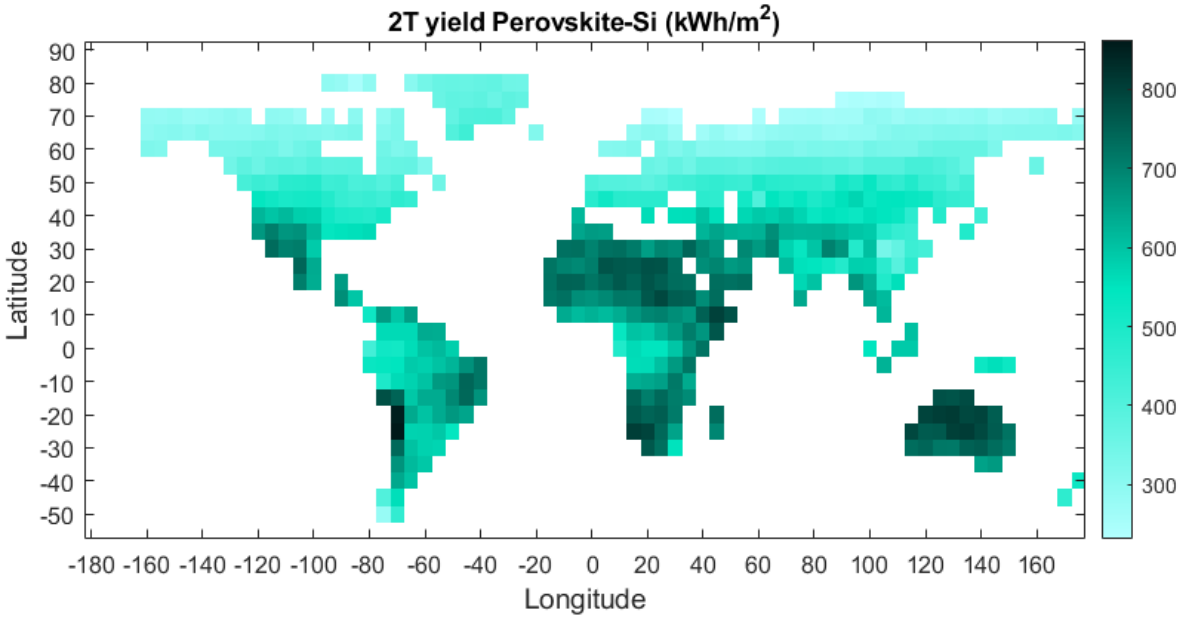

Figure 5.23: Optimal 2T yield of 1.72 eV Perovskite and Si. The values range from 196 to 701 kWh/m^2.

The performance was modeled under STC to compare with literature. For STC the optimal thickness of Si is 100 μm and the efficiency is 34.52 %. Almansouri et al. [72] used the detailed balance model and incorporated losses like incomplete absorption, glass reflection and parasitic absorption afterwards. Their efficiency without losses is 40.6 % and decreases to 29.8 % when losses are considered. A bandgap is not specifically named, but the absorption coefficient used is of 1.5 eV Perovskite[73]. Futscher and Ehrler [74] used a detailed balance approach, modified for tandem solar cells. They found a 45.1 % efficiency with an 1.73 eV top bandgap. Thus the efficiency calculated in this project is notably lower. The current of Si, calculated by the Richter model will be lower than for the detailed balance model, since Auger recombination is considered by the first. And this could lead to a overall lower 2T efficiency.

The worldwide efficiency is depicted in Figure 5.24. The efficiency ranges from 30.30 to 35.34 %. The average is 33.45 % and the irradiance weighted average is 33.51 %. One of the locations with low efficiency is the part of north of Africa and teh Middle East were the normalisation factor was high (Figure 5.5). The normalisation of the spectrum due to high AOD can influence the efficiency. High AOD mainly deceases the blue part of the spectrum, the part that is absorbed. By normalising, all of the spectrum is either increased or decreased. In case of increasing (normalisation factor > 1), also the redder part of the spectrum, which can not be absorbed, is increased, resulting in a lower efficiency. But the normalisation should also result in increased efficiencies, where the normalisation factor is < 1. In the northern hemisphere, between 30° and 75° and in the southern hemisphere below 45°, the normalisation factor was among the lowest. In the southern hemisphere, the high efficiencies can be found there, but in northern hemisphere only the US and Mexico have a high efficiency. When moving north, from Mexico to Canada, the efficiency increases and then, around ca. 50°, the efficiency drops. Because the optimum was found using current matching and the thickness step size is 10 μm, the currents might not optimally match. In Figure 5.25 the mpp current difference between Perovskite and Si is depicted. Si is subtracted from Perovskite, so a negative value means $J_{mpp,Si} > J_{mpp,Perovskite}$ and vise versa for positive values.

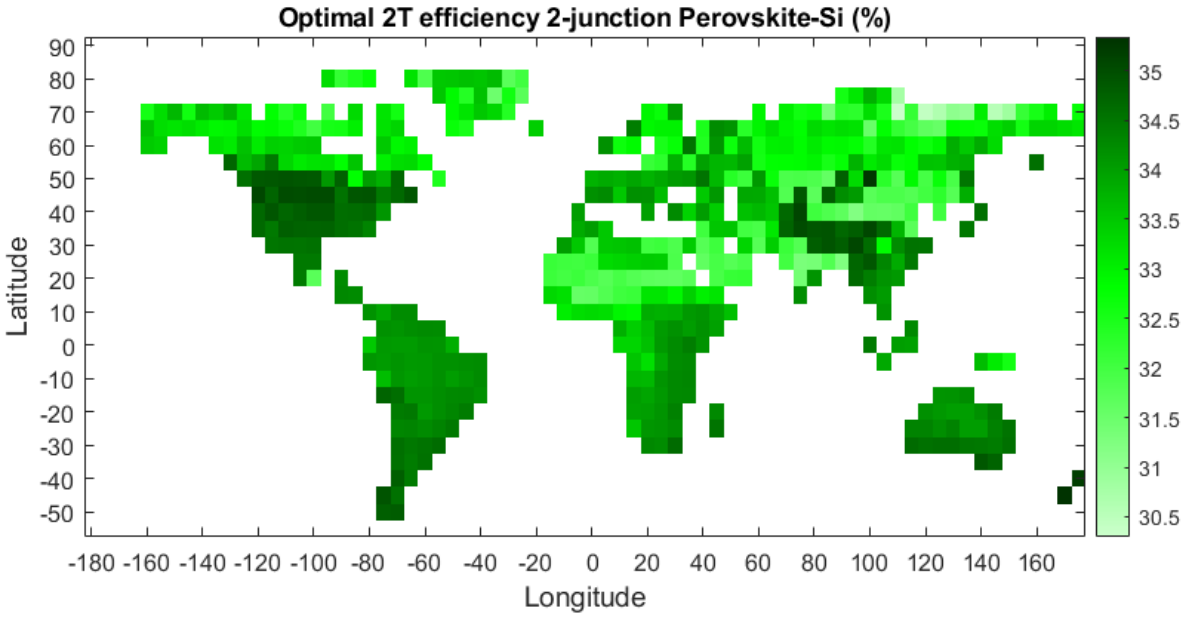

Figure 5.24: Optimal 2T efficiency of 1.72 eV Perovskite and Si. Average is 16.90 cm, minimum is 6 cm and maximum is 51 cm.

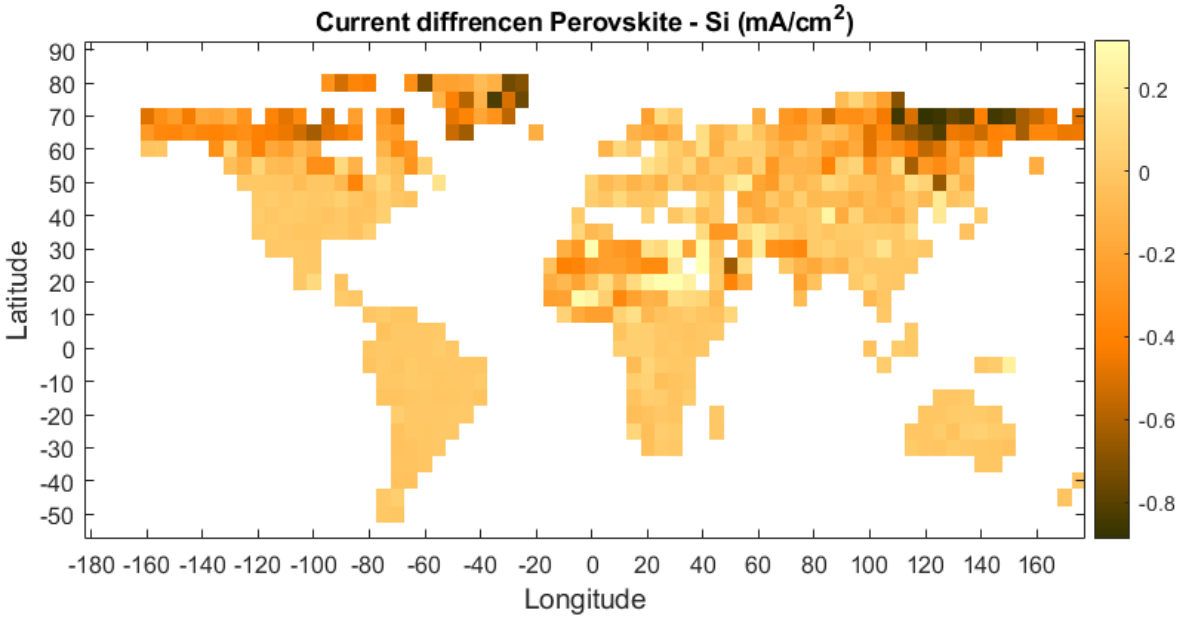

Figure 5.25: Absolute mpp current difference between Perovskite and Si. Si is subtracted from Perovskite, so a negative value means the current of Si is higher than the current of Perovskite and vise versa for positive values.

The current difference ranges from -0.89 to 0.32 mA/cm^2. The average difference is -0.11 mA/cm^2 and the irradiance weighted average is -0.08 mA/cm^2. For the current difference to become less negative, the thickness of Si would need to decrease. The most negative values can be found in the north, where the thickness is already equal to the lower limit, 10μm. For the current difference to become less positive, the thickness of Si needs to increase. Nothing limits the optimisation to do that, so since this did not happen, it means a 10 μm thicker Si layer leads to greater current difference to Perovskite. Both cases can be improved, if the step size is decreased to 1 μm or smaller. As was mentioned earlier, for STC the optimal Si thickness is 100 μm and the efficiency is 34.52 %. The current difference is 0.04 mA/cm^2. Decreasing the thickness steps to 1 μm, results in a optimal thickness of 104 μm, an efficiency of 34.59 % and a current difference of 0.003 mA/cm^2.
To see if there is a direct relation to either the normalisation factor or the current difference, plots for both op-

timal thickness and efficiency were made and are depicted in Figure 5.26. In the top right figure it can be seen that for the efficiencies between 34 and 35 %, most points are clustered around zero current difference. In the top left, the values of current difference are spread out most at the smallest thicknesses and the deviation to 0 becomes smaller as the thickness increases. This indicates that the smaller the needed thickness is, the more precise the thickness should be. According to the plot of the optimal thickness vs. the normalisation factor (bottom left), more locations have a factor below one than above one, especially as the thickness increases.

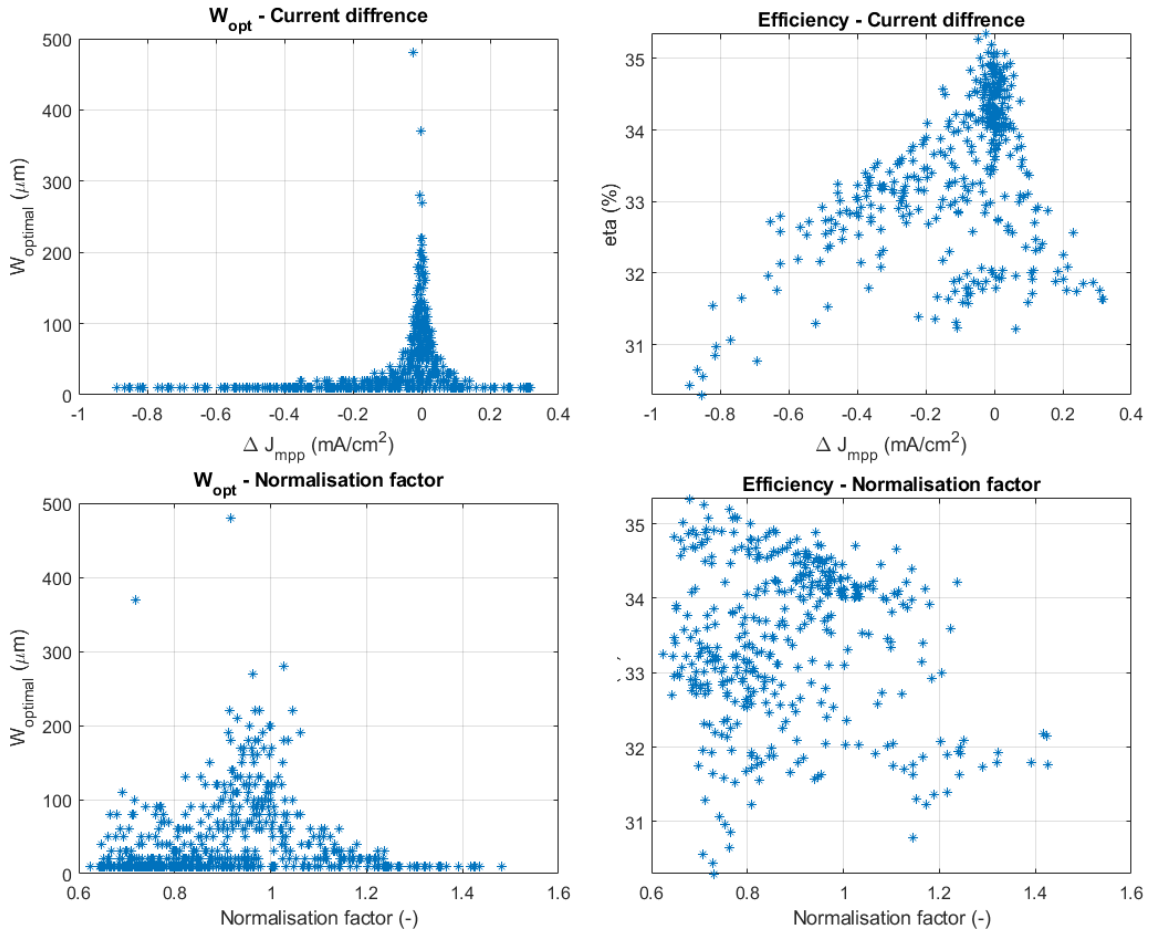

Figure 5.26: Optimal thickness of Si and 2T efficiency plotted against the current difference and normalisation factor.

5.4. Relation between top-bandgap and optimal Si thickness

The optimal thickness of single junction Si differs from the thickness of Si as bottom absorber layer of the double junction Perovskite-Si. In this section the relation between the top-bandgap and the optimal thickness of Si will be explored. To find the optimal combination of top-bandgap and thickness, both variable would need to be varied. Due to limiting time, it was not possible to do this for a whole map. Instead this relation was calculated for STC and four variations. And a map was made of the optimal top bandgap with a Si thickness equal to the irradiance weighted average optimal thickness of single junction Si: 165 μm. In Figure 5.27 the optimal top bandgap and thickness for STC and four variations is plotted. The four variations are: AM1.5 spectrum with temperatures of 0°C and 50°C (273.15K and 323.15K) as well as for AM1.0 and AM2.0 spectra with 25°C.

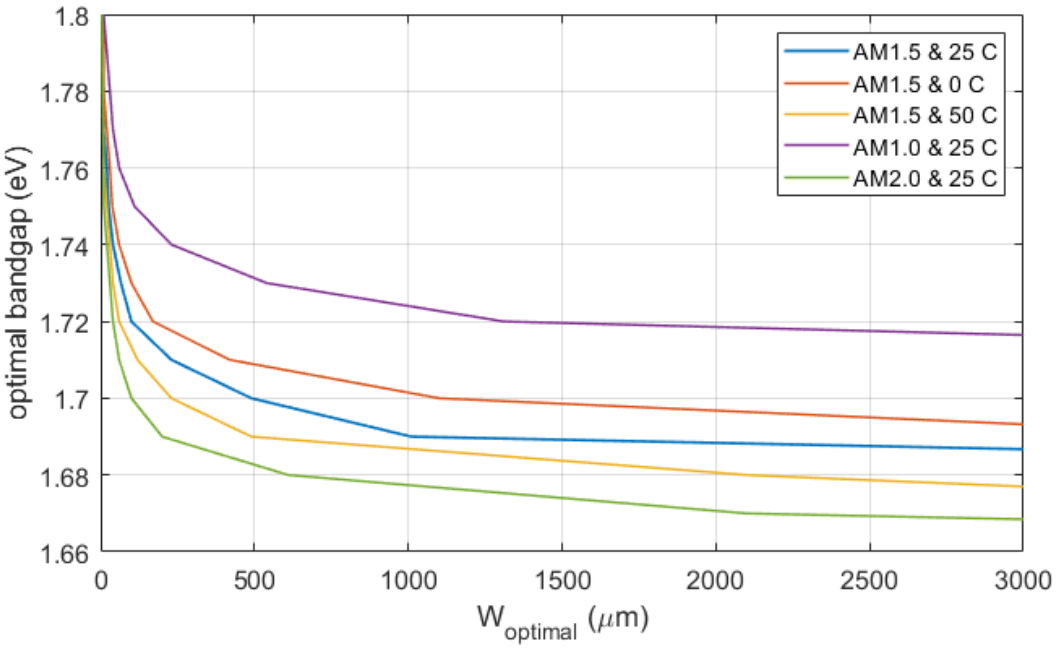

Figure 5.27: Relation between optimal top-bandgap and thickness of Si for varying standard spectra and temperatures.

In all cases Si is thinnest for high bandgaps and the thickness increases with decreasing bandgap. For the top cell, the higher the bandgap, the smaller the part of the spectrum which can be absorbed, thus the lower the current. As a result Si needs to match a lower current and at the same time there is a larger percentage of the spectrum left for Si to absorb. Leading to the thickness of Si being lower. The AM1.5 spectrum with a temperature of 0 °C results in an increased optimal thickness per bandgap and this effect is even stronger for the AM1.0 spectrum with 25°C. The reverse happens for the warmer temperature of 50 °C or using the AM 2.0 spectrum. Similarly the effect is stronger when changing the spectrum than changing the temperature. In Figure 5.28 the AM spectra are depicted. The spectra were made by Ziar[48], using SMARTS. The AM1.0 spectrum relatively has the highest spectral irradiance in the blue part of the spectrum of all three spectra. This part is mostly absorbed by the top cell (Figure 5.18 shows what part a 1.72eV cell would absorb). Thus the current generated by the top cell under AM1.0 will be more than under the other two spectra. And thus the thickness per bandgap is highest for AM1.0 and lowest for AM2.0.

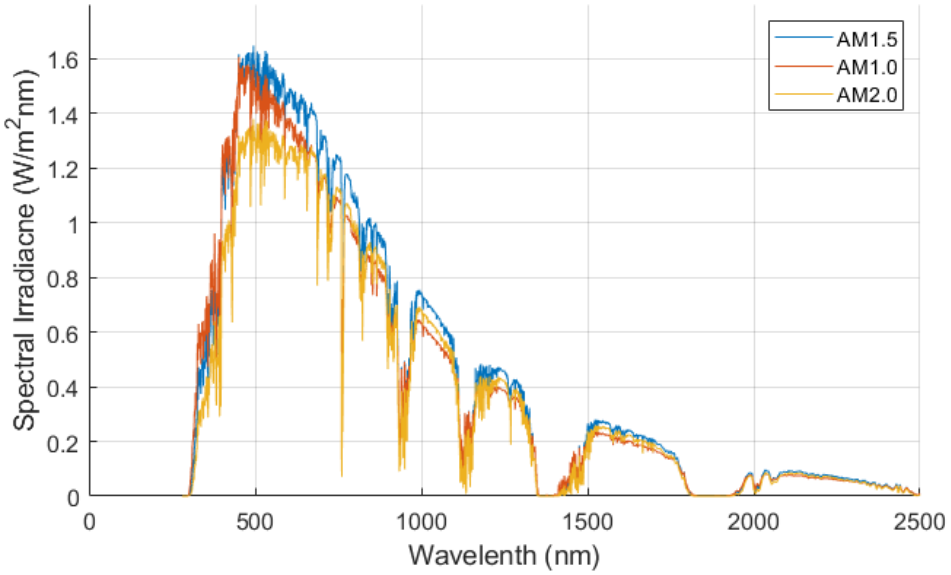

Figure 5.28: The AM1.5 spectrum, AM1.0 spectrum and AM2.0 spectrum.

In Figure 5.29 the worldwide optimal bandgaps with 165 μm thickness are depicted. The bandgaps range from 1.55 to 1.76 eV. The average is 1.655 eV and the irradiance weighted average is 1.663 eV. The smallest bandgaps can be found in the far north.

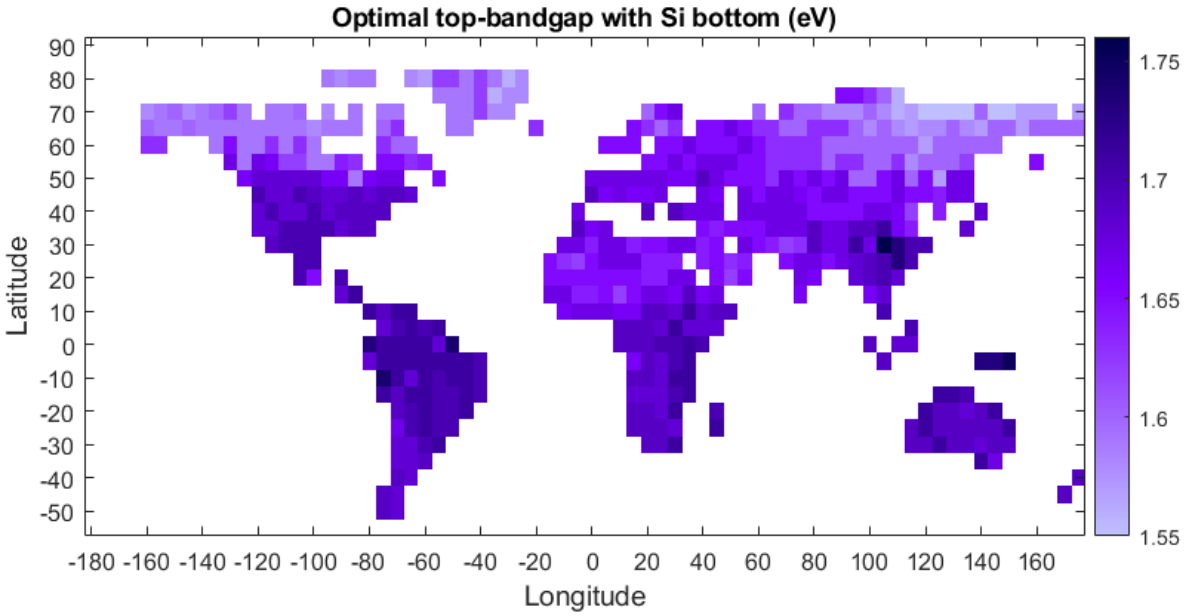

Figure 5.29: Optimal top-bandgap with an absorber layer of Si at the bottom. The thickness of Si is 165 μm. The bandgap values range from 1.55 to 1.76 eV.

To find possible relations between the optimal bandgap and input values, the optimal bandgap was plotted against ambient temperature, GHI, relative humidity and precipitable water. The plots are depicted in Figure 5.30. Extra plot can be found in section B.3. In the top left plot it can be seen that the optimal bandgap first increases with increasing temperature and after ca. 290 K decreases again. This relation, although less strongly, can be observed for GHI as well (top right). For relative humidity (bottom left) the optimal bandgap values range is mostly constant with increasing humidity, but after 0.6, this range increases. Worldwide there are areas that have high humidity as well as either a low or high temperature, which can explain that for high

humidity both high and low optimal bandgap values can be found worldwide. For precipitable water the optimal bandgap increases with the increasing amount of water in the air.

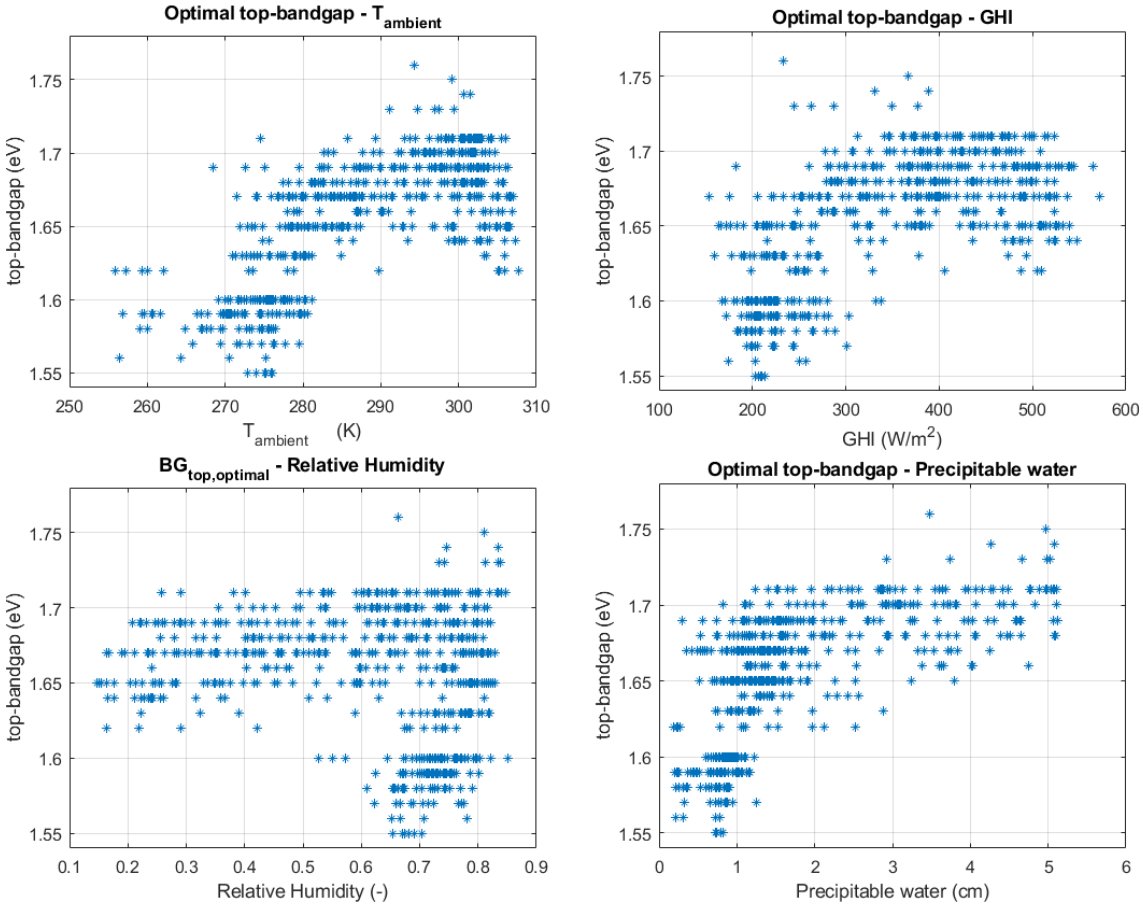

Figure 5.30: Plots of the optimal bandgaps (for $W_{opt,Si}$ = 165 μm) against ambient temperature, GHI, relative humidity and precipitable water.

6

Conclusion and recommendation

In this thesis the effect of global climate differences on the performance of single-junction Si (1.12 eV) and double-junction Perovskite(1.72 eV)-Si solar cells was analysis. The GHI values simulated by SMARTS range from 141 to 615 W/m^2 and the distribution of high and low irradiance areas on the global map is good overall, except for north Africa and the Middle East, were it was too low due to high AOD. As a quick fix, the spectra were normalised using the irradiance data from CERES. Since the AOD effects the blue part of the spectrum more, this is not a long-term solution. The normalisation factor ranges from 0.625 to 1.480 and is on average 0.915. After normalising the GHI ranges from 154 to 572 W/m^2.
The Si bottom layer was modeled using the thickness-dependent Richter model [6]. The minimum of the optimal thickness of single junction Si is 70 μm, the maximum is 870 μm, the average is 205 μm and the irradiance weighted average is 165 μm. A function was fitted to describe the relation between the optimal thickness and temperature. The efficiency ranges between 27.22 and 31.03 %, the average is 29.06 % and the irradiance weighted average is 28.88 %.
Current matching was used to find the optimal Si thickness for double junction Perovskite-Si. The thickness ranges between 10 and 4500 μm, but only nine locations (1.5 %) had a thickness above 500 μm. The average thickness is 77 μm and the irradiance weighted average is 81 μm. By comparing 6 local spectra it was found that the spectra of locations with a high optimal Si thickness had more spectral irradiance in the blue part than low thickness spectra. The efficiency ranges from 30.30 to 35.34 %, the average is 33.45 % and the irradiance weighted average is 33.51 %. All values are quite low, which can be due to the normalisation of the GHI spectra and the too large current differences due to too large thickness steps (10 μm). When plotted, it was found that for low thicknesses the current difference values were spread out most (between -0.89 and 0.32 mA/sm^2) and for increasing thickness, the range of current difference decreased, most values being close to zero.
The optimal top-bandgap was determined using current matching. The thickness of the bottom layer was equal to the irradiance weighted average optimal thickness of single junction Si(165 μm). The bandgaps range from 1.55 to 1.76 eV. The average is 1.655 eV and the irradiance weighted average is 1.663 eV. The relation between the Si thickness and top-bandgap for STC was investigated. High bandgaps had the lowest optimal thicknesses and the thickness increased with decreasing top-bandgap. Alterations in spectrum and temperature where applied as well to find the effect on that relation. When the temperature decreases or the spectrum is changed to AM1.0, the thicknesses for each bandgap become larger (the curve bends earlier) and vice versa was true for a temperature increase or usage of the AM2.0 spectra. In both cases, the spectrum change had a larger impact that temperature change.

The topic of this research is very interesting and worth further research. For future research the map resolution should be increased to 1° x 1°. This way local differences and the shape and size of areas with similar values is better visible. Plus, this results in more data point which is favorable for fitting functions. Another practical step is investigating the too high AOD in the areas where the irradiance should to be high. And the step size for finding the optimal thickness should be decreased to reduce the current difference.
Besides irradiation, population can also be a factor to the likeliness of PV instalment. A higher population means there is more PV necessary to provide the energy demand. Because of that, the population weighted average Si thickness is an interesting value to obtain.

A well known climate classification system is the one derived by Köppen and Geiger [75]. In the Köppen-Geiger system climate are divided into five main classes and 30 sub-types [76]. For future study it would be interesting to find out if PV cell perform similar in the same climate at different locations in the world. And to see if the performance can be generalized per climate classification.
Because the climate is changing, it would be useful to study was effect this has on the performance of PV. Peters and Buonassisi [77] have recently established meteorological trends and projected reduction in performance of single junction PV cell Si and CdTe. This subject can be expanded by adding double junction PV.

A

Yearly data input maps

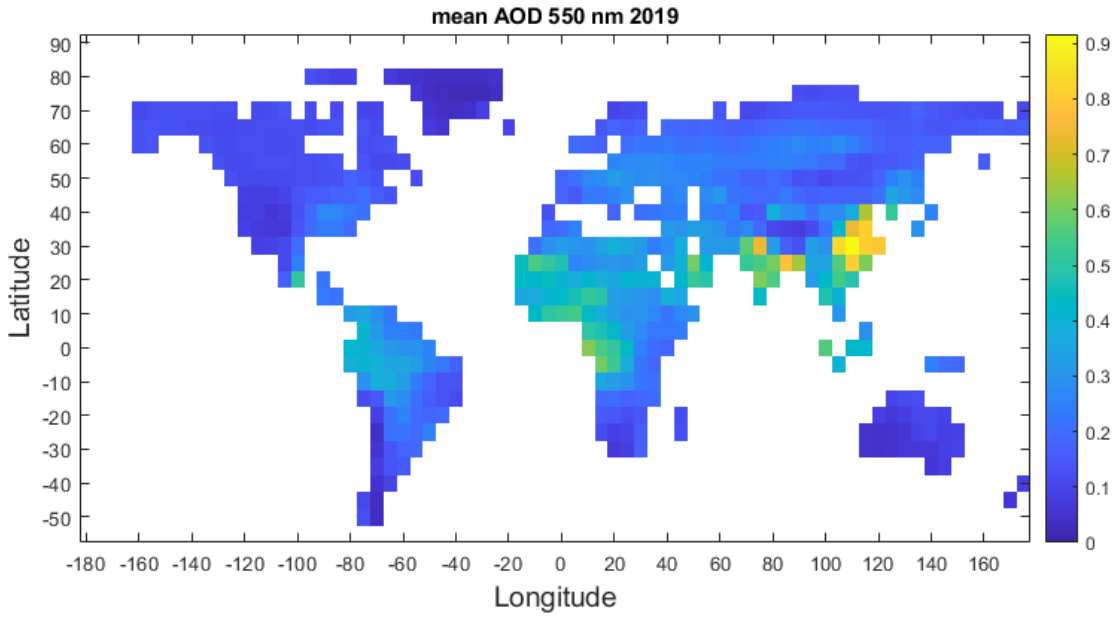

Figure A.1: AOD 550 nm, correct average land data

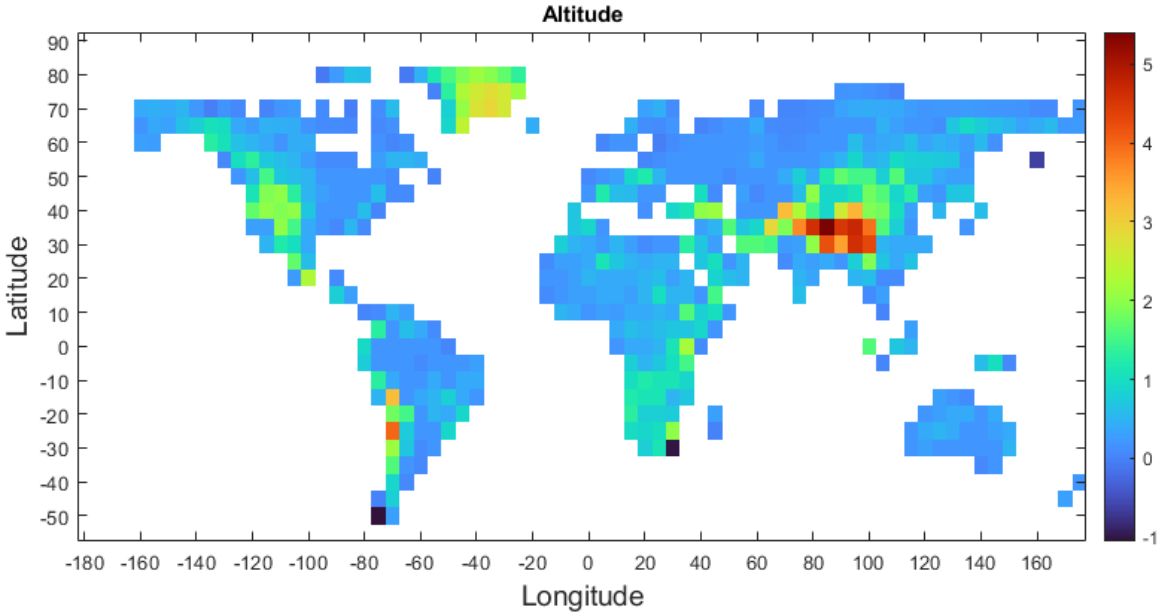

Figure A.2: Altitude

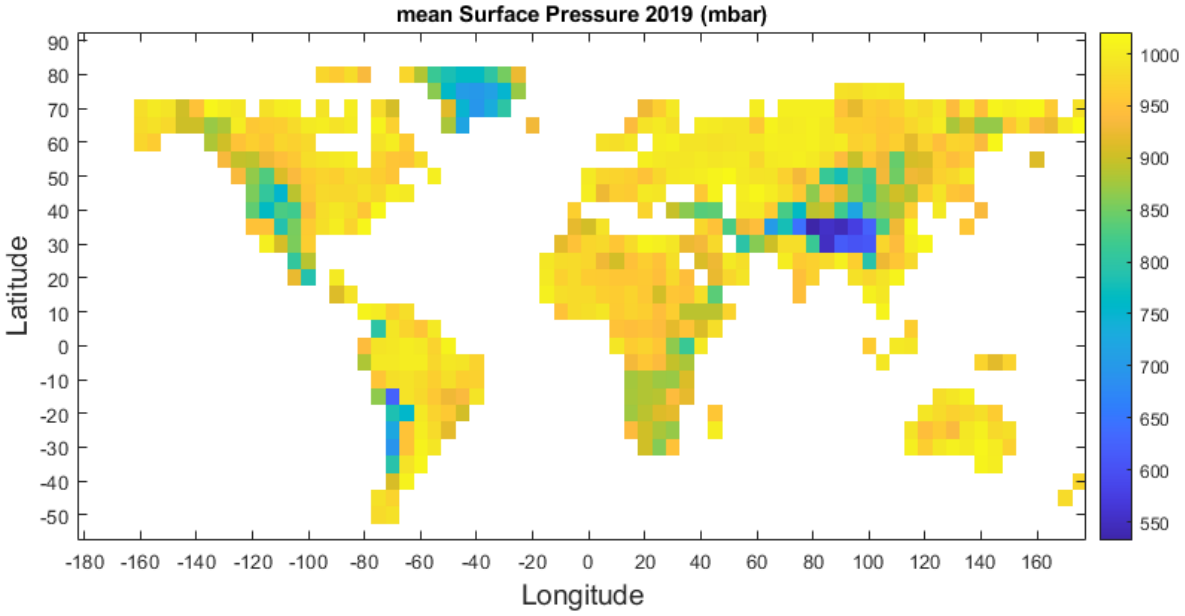

Figure A.3: Yearly average surface pressure 2019

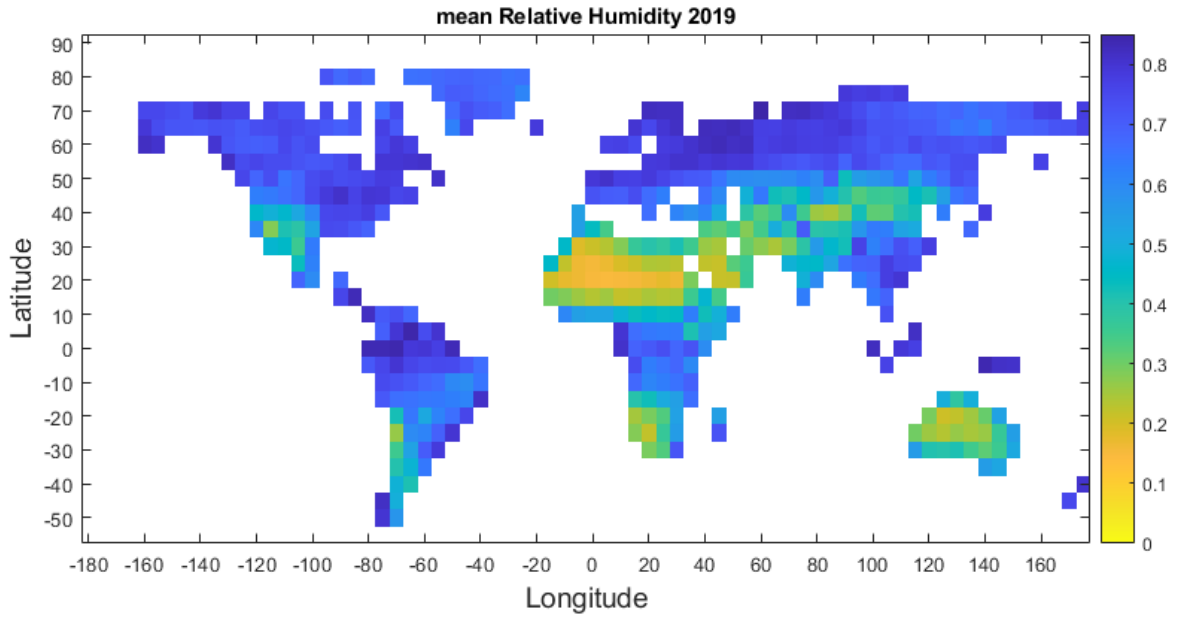

Figure A.4: Yearly average relative humidity 2019

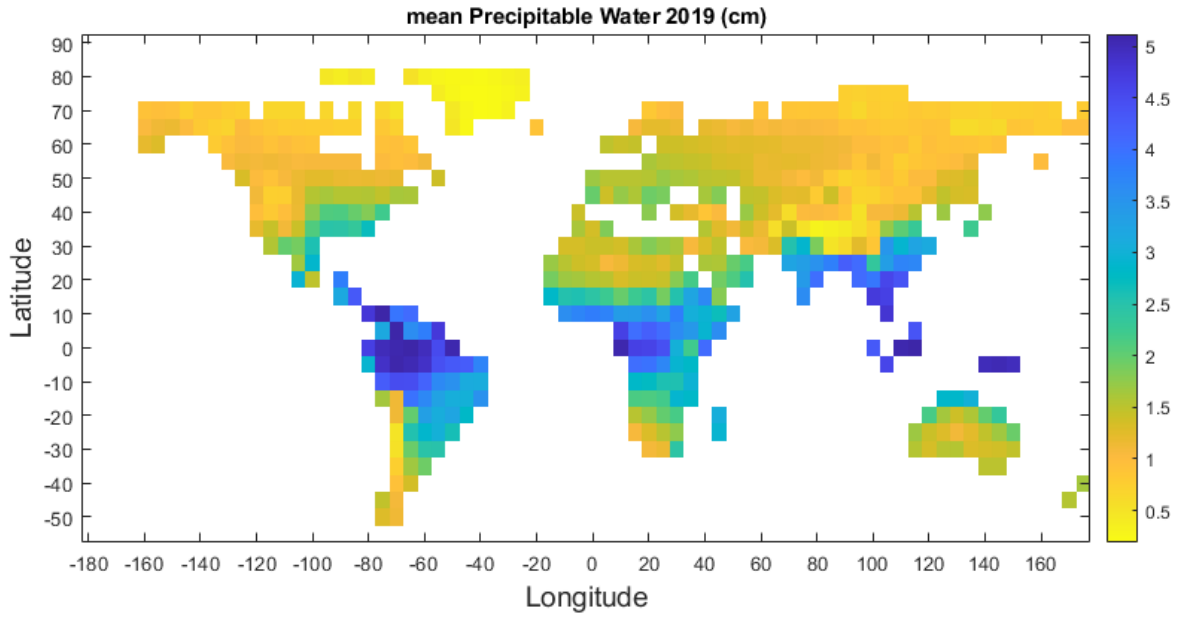

Figure A.5: Yearly average precipitable water 2019

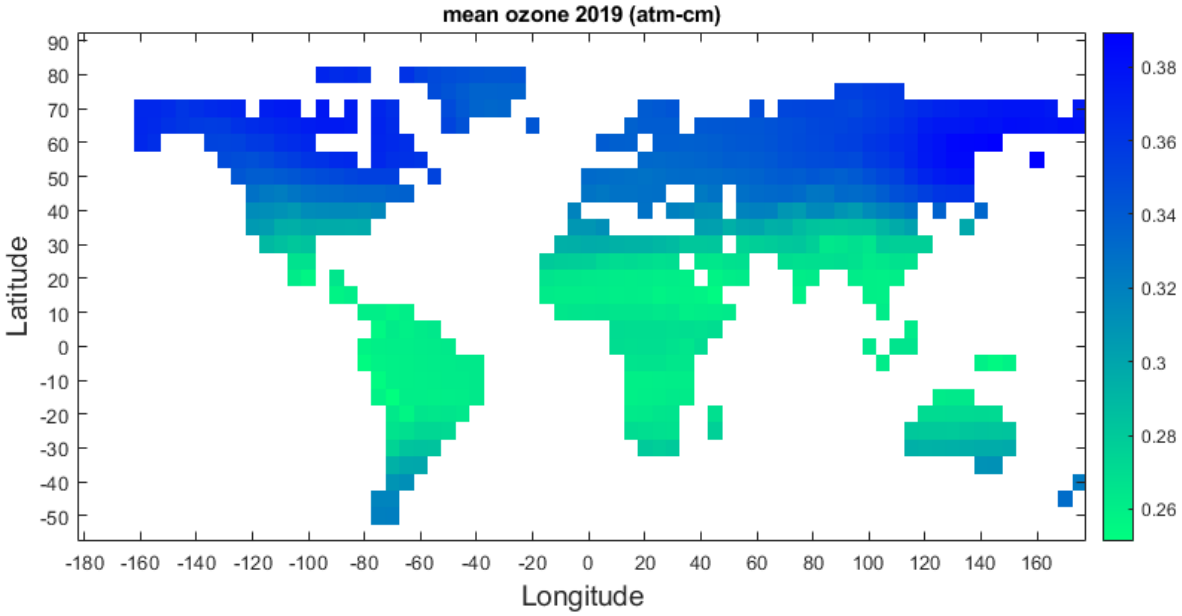

Figure A.6: Yearly average ozone 2019

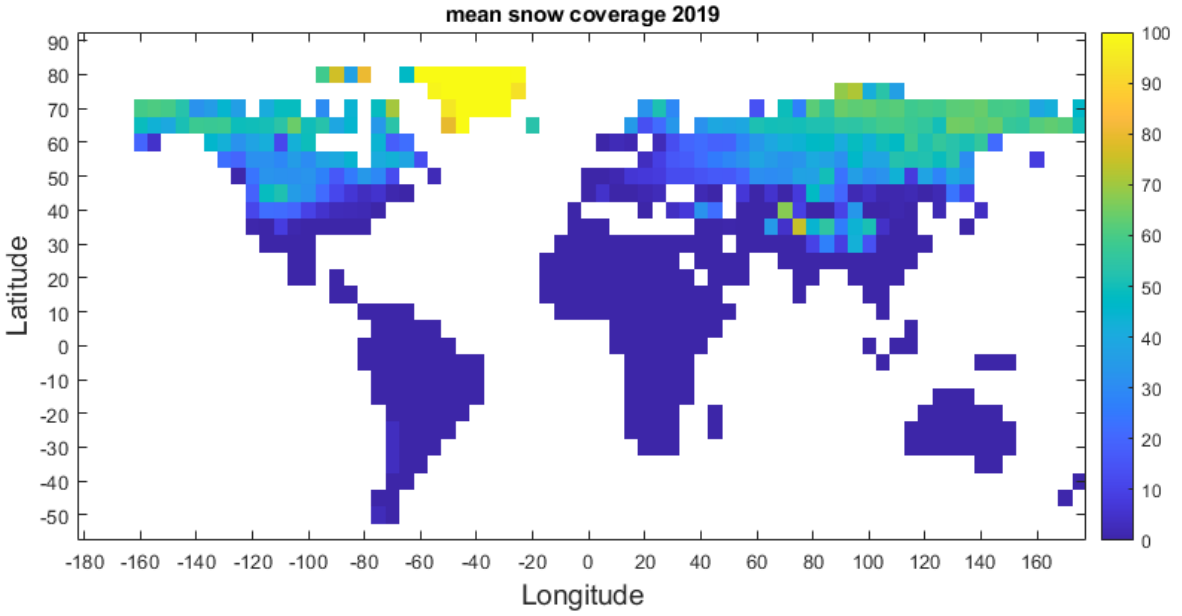

Figure A.7: Yearly average snow coverage 2019

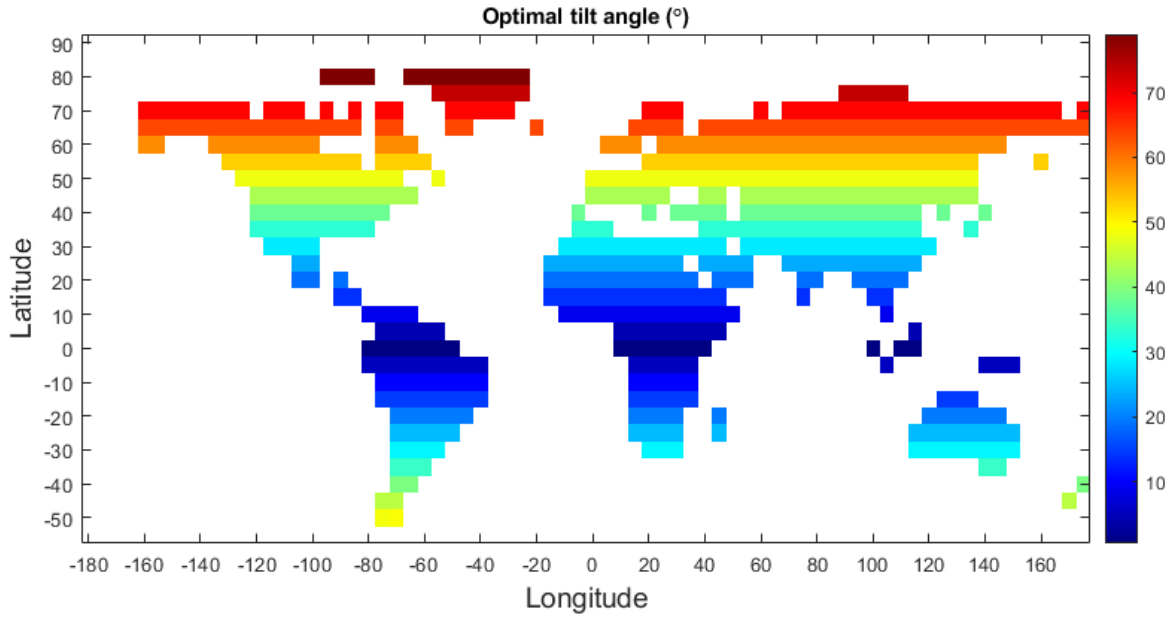

Figure A.8: Optimal tilt angle

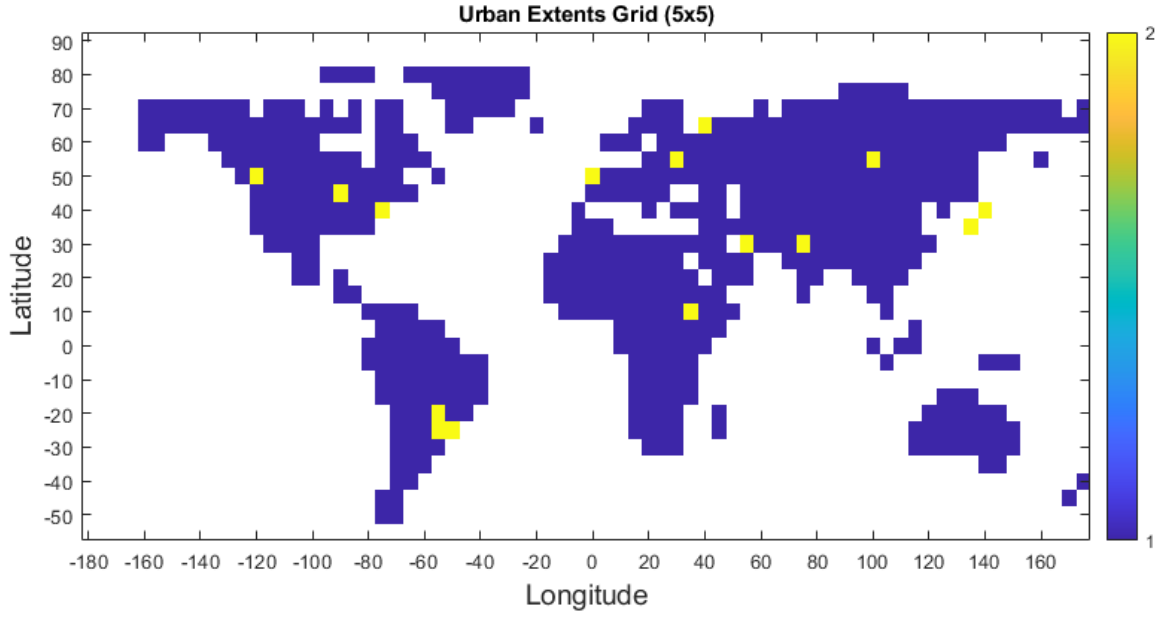

Figure A.9: Urban Extents

B

Extra results

B.1. 1-junction Si

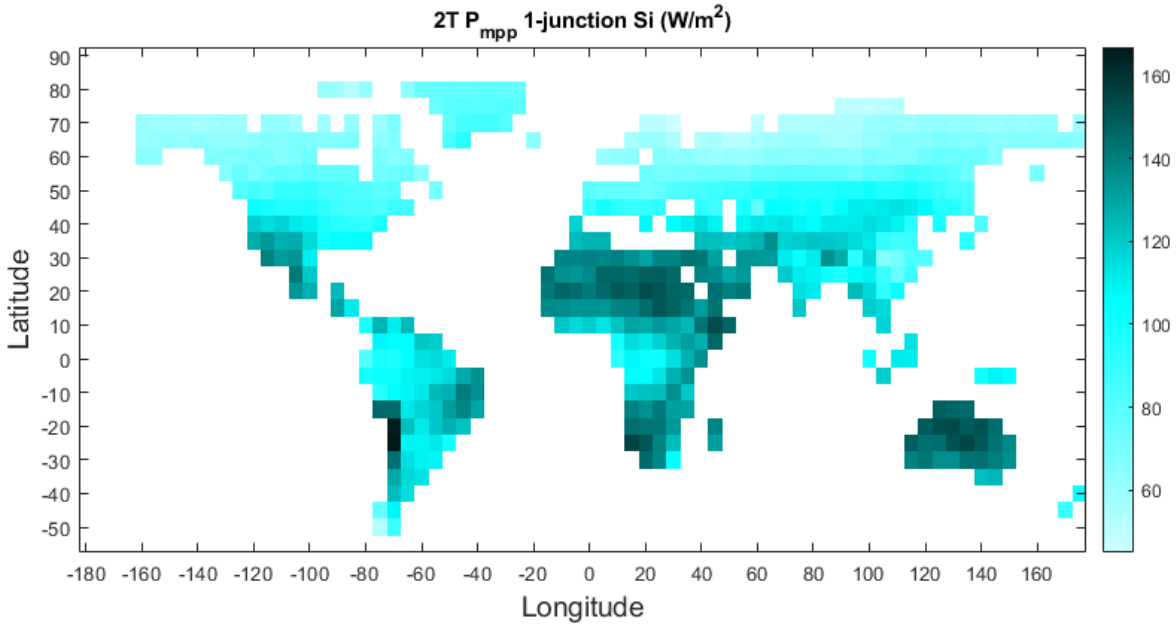

Figure B.1: Maximum power point power for single junction Si, when its thickness is its local optimum.

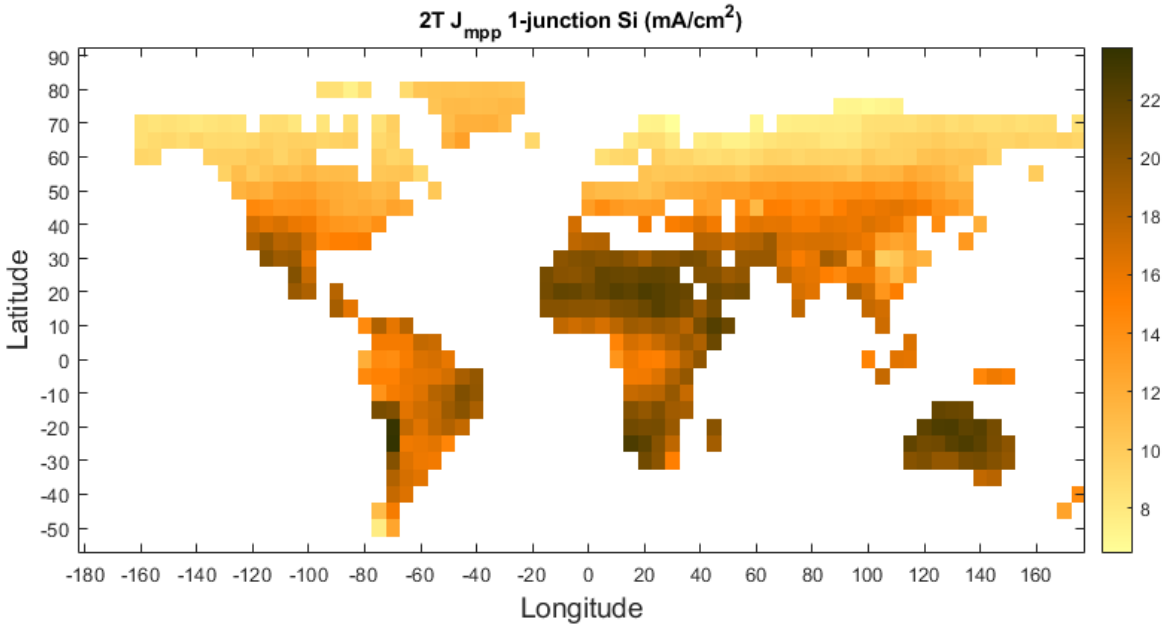

Figure B.2: mpp current for single junction Si, when its thickness is its local optimum.

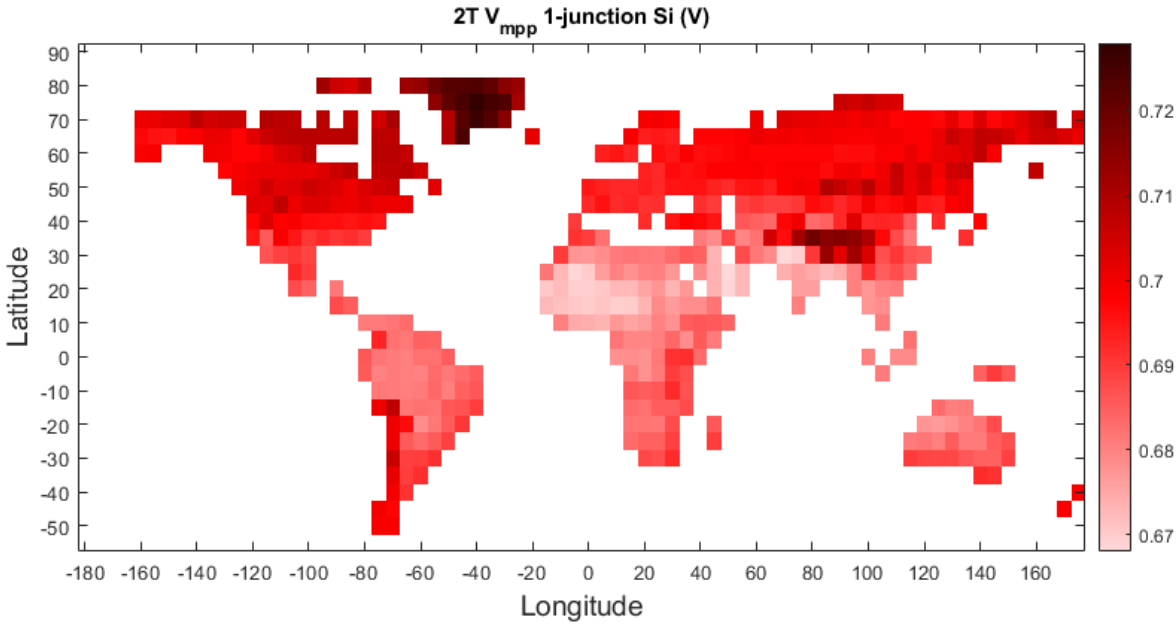

Figure B.3: mpp voltage for single junction Si, when its thickness is its local optimum.

B.2. 2-junction Perovskite-Si

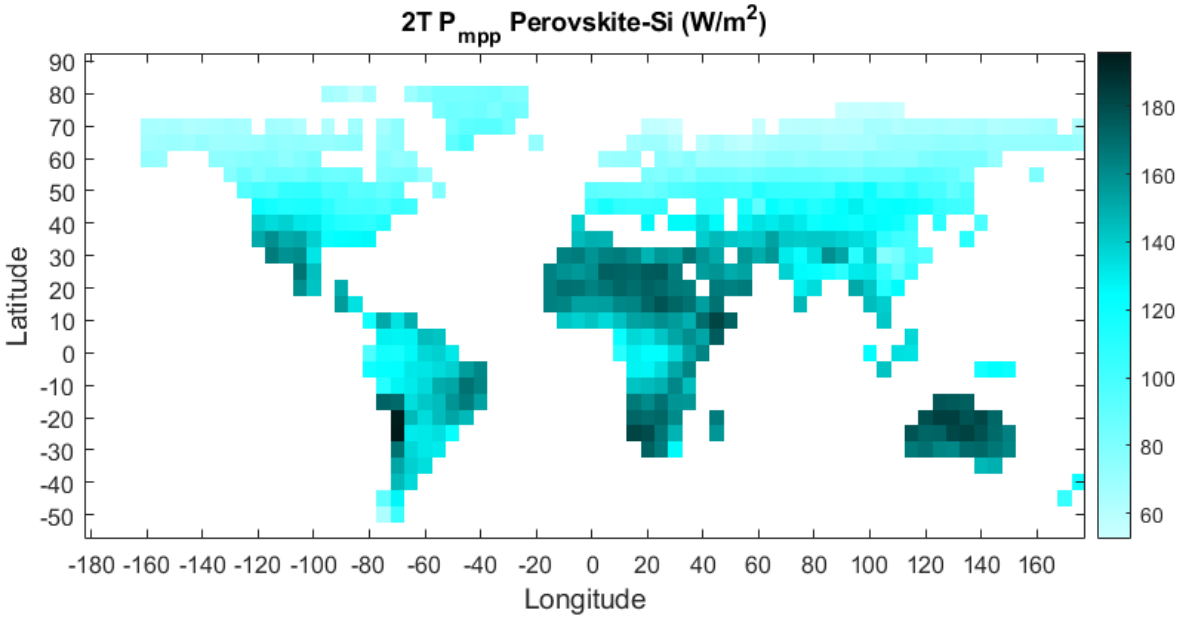

Figure B.4: mpp 2T power of double junction Perovskite-Si.

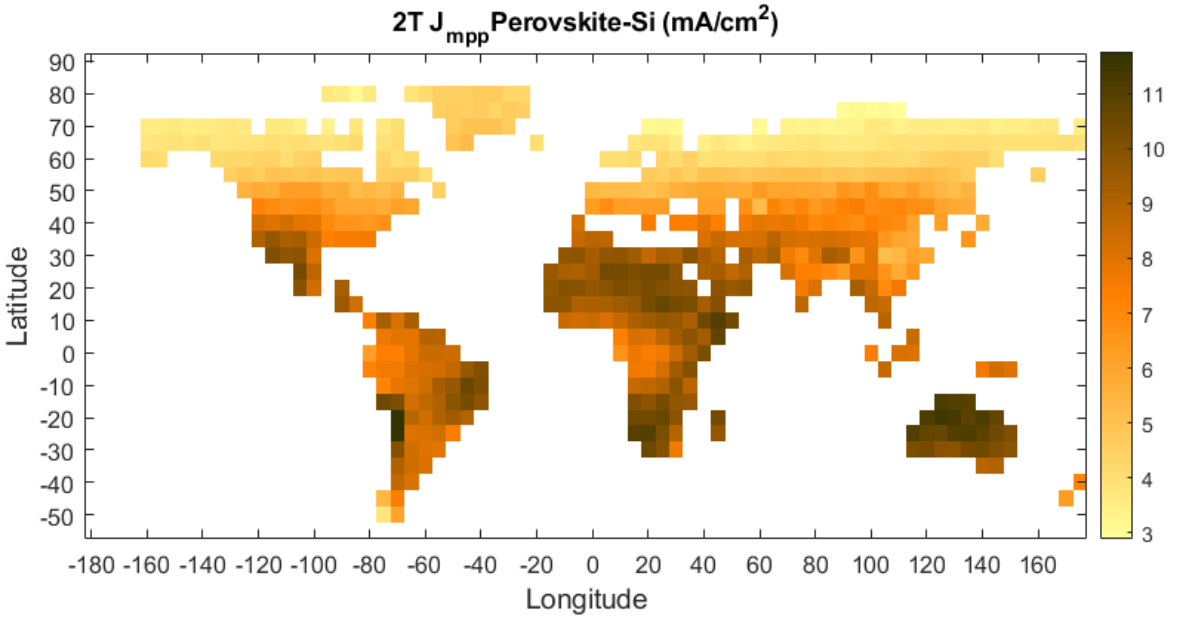

Figure B.5: mpp 2T current (current of the limiting cell) of double junction Perovskite-Si.

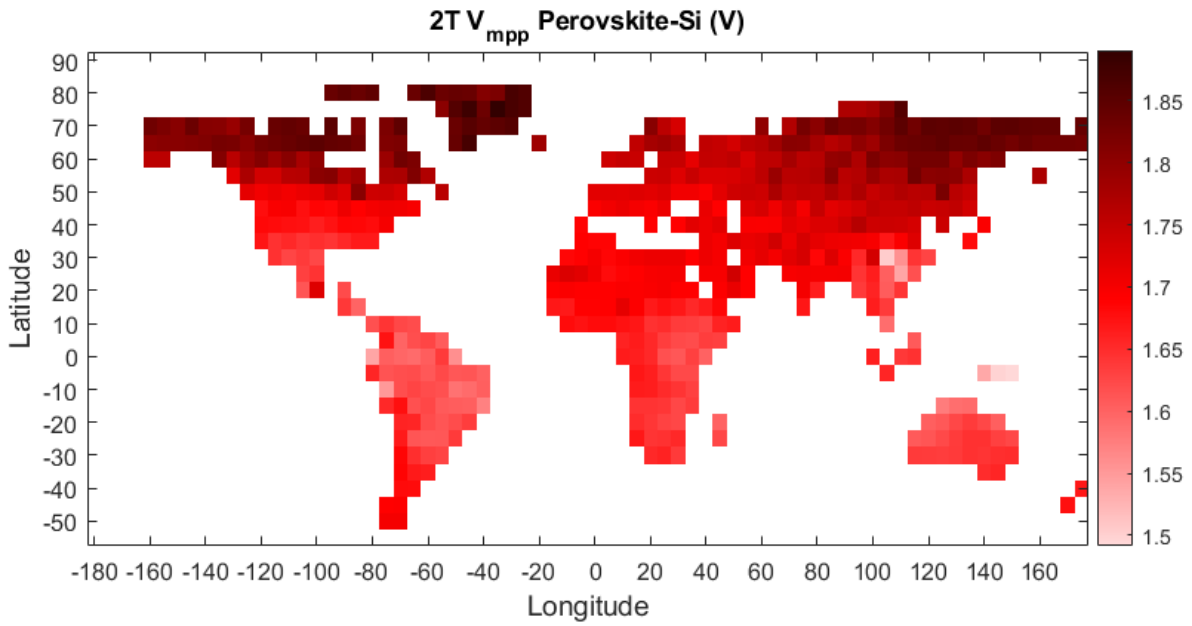

Figure B.6: mpp voltage of double junction Perovskite-Si. This is the sum of the voltage produced by the Perovskite top- and Si bottom absorber.

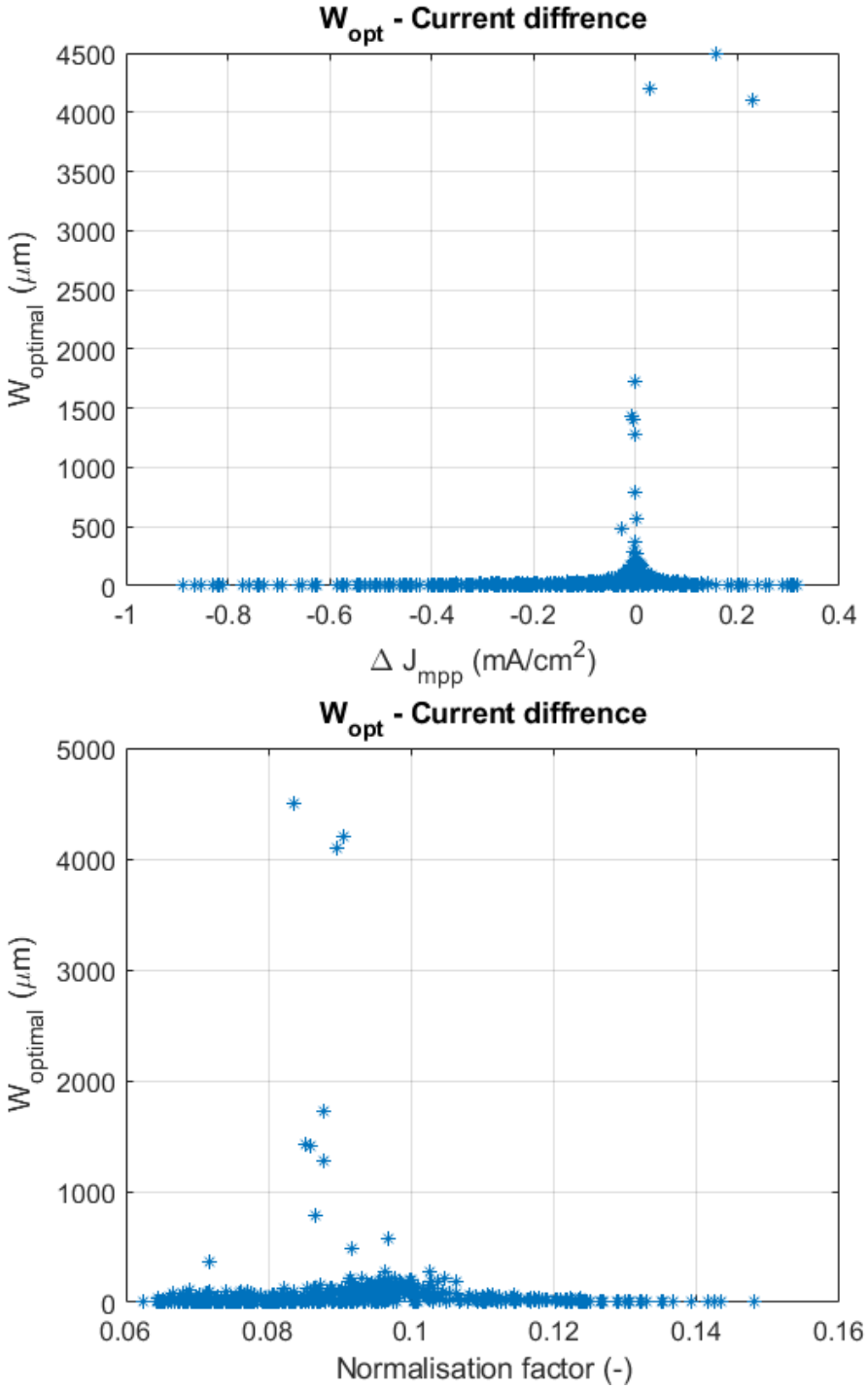

Figure B.7: mpp voltage of double junction Perovskite-Si. This is the sum of the voltage produced by the Perovskite top- and Si bottom absorber.

B.3. Relation between top-bandgap and optimal Si thickness

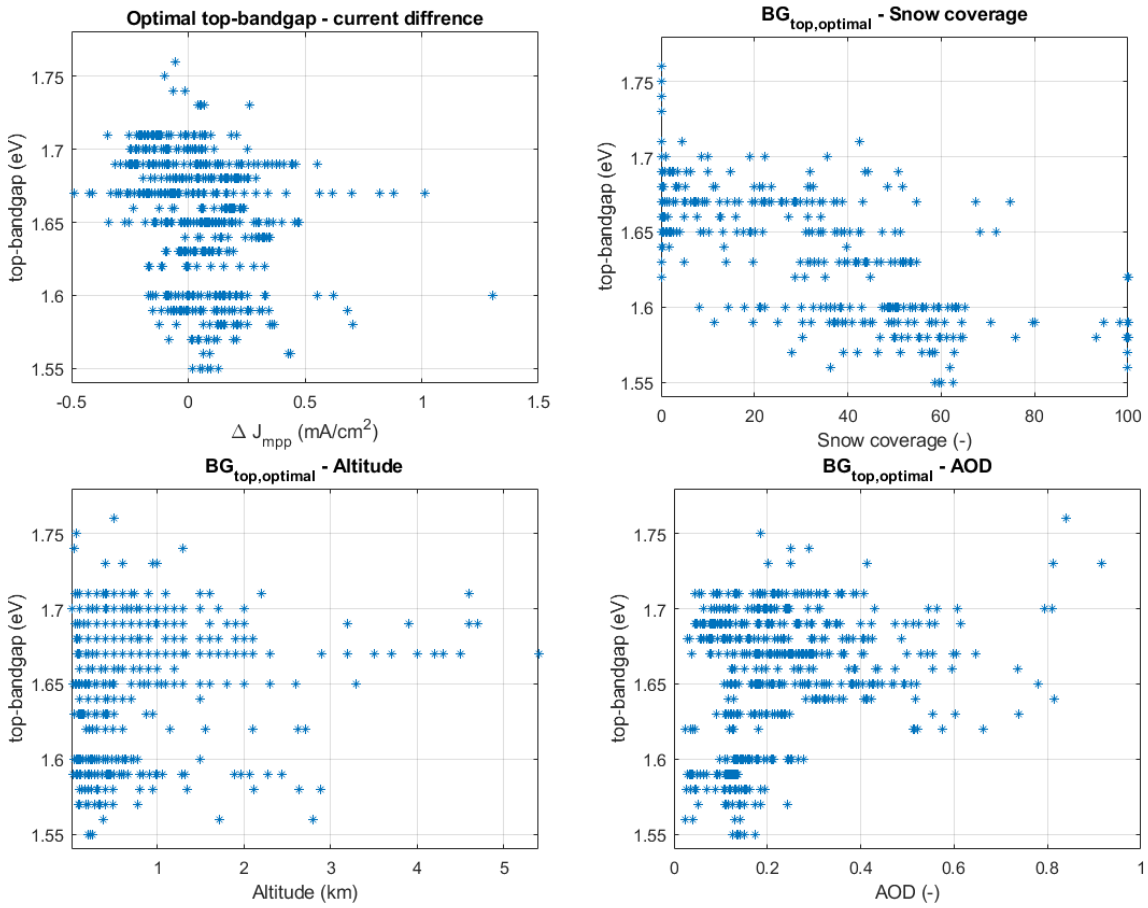

Figure B.8: Plots of the optimal bandgaps (for $W_{opt,Si}$ = 165 μm) against the current difference (negative means Si current is higher that current of top absorber layer), snow coverage, altitude and aerosol optimal depth(AOD).

Bibliography

[1] Raphael Schmager, Malte Langenhorst, Jonathan Lehr, Uli Lemmer, Bryce S Richards, and Ulrich W Paetzold. Methodology of energy yield modelling of perovskite-based multi-junction photovoltaics. *Optics express*, 27(8):A507–A523, 2019.

[2] Hannah Ritchie. Renewable energy. *Our World in Data*, 2017. URL `https://ourworldindata.org/renewable-energy`. [Accessed: 2020-01-28].

[3] Heymi Bahar. Solar pv, 2020. URL `https://www.iea.org/reports/solar-pv`. [Accessed: 2020-01-28].

[4] Solar Energy Technologies Office. Solar photovoltaic cell basics. URL `https://www.iea.org/reports/solar-pv`. [Accessed: 2020-01-28].

[5] William Shockley and Hans J. Queisser. Detailed balance limit of efficiency of p-n junction solar cells. *Journal of applied physics*, 32(3):510–519, 1961.

[6] Armin Richter, Martin Hermle, and Stefan W. Glunz. Reassessment of the limiting efficiency for crystalline silicon solar cells. *IEEE journal of photovoltaics*, 3(4):1184–1191, 2013.

[7] Bruno Ehrler, Esther Alarcón-Lladó, Stefan W. Tabernig, Tom Veeken, Erik C. Garnett, and Albert Polman. Photovoltaics reaching for the shockley–queisser limit. *ACS Energy Letters*, 5(9):3029–3033, 2020. doi: 10.1021/acsenergylett.0c01790.

[8] Arno Smets. Pv2x 3.2.2 multi junction devices, 2017. URL `https://delftxdownloads.tudelft.nl/PV2x/3.2.2/PV2x_2017_3.2.2_Multi_junction_devices-slides.pdf`. [Accessed: 2019-03-01].

[9] Arno Smets. Pv1x 1.2 solar radiation 2, 2017. URL `https://delftxdownloads.tudelft.nl/PV1x_Solar_Energy/Week_1/PV1x_2017_1.2_The_Sun_Radiation_part2-slides.pdf`. [Accessed: 2020-01-12].

[10] Ian Marius Peters and Tonio Buonassisi. Energy yield limits for single-junction solar cells. *Joule*, 2(6): 1160–1170, 2018.

[11] Haohui Liu, Carlos D Rodríguez-Gallegos, Zhe Liu, Tonio Buonassisi, Thomas Reindl, and Ian Marius Peters. A worldwide theoretical comparison of outdoor potential for various silicon-based tandem module architecture. *Cell Reports Physical Science*, page 100037, 2020.

[12] Sven Rühle. Tabulated values of the shockley–queisser limit for single junction solar cells. *Solar Energy*, 130:139–147, 2016.

[13] Markus Fischer. ITRPV 11 edtion report presentation and key findings. Technical report, 2020. [Accessed: 2021-02-25].

[14] Wells Wang. N-type market growth, 2020. URL `https://www.pv-magazine.com/2020/10/20/n-type-market-growth/`. [Accessed: 2021-02-25].

[15] Christian A. Gueymard. *SMARTS code, version 2.9. 5, USER'S MANUAL For Windows*, 2005.

[16] MATLAB. *version R2018b*. The MathWorks Inc., Natick, Massachusetts, 2018.

[17] MATLAB. *version R2020b*. The MathWorks Inc., Natick, Massachusetts, 2020.

[18] Cas de Mooij. A Spectrally Resolved Model for a PV + PCM System. Master's thesis, Delft University of Technology, Mekelweg 5, 2628 CD Delft, 2020. URL `http://resolver.tudelft.nl/uuid:1ae70ca5-8a8e-4f5b-8838-a106de39c18c`.

[19] H Beaudoing, M Rodell, and NASA/GSFC/HSL (2020). *GLDAS Noah Land Surface Model L4 3 hourly 1.0 x 1.0 degree V2.1*. Greenbelt, Maryland, USA, Goddard Earth Sciences Data and Information Services Center (GES DISC), 2020. doi: 10.5067/IIG8FHR17DA9. [Accessed: 2020-10-23].

[20] Matthew Rodell, PR Houser, UEA Jambor, J Gottschalck, K Mitchell, C-J Meng, K Arsenault, B Cosgrove, J Radakovich, M Bosilovich, et al. The global land data assimilation system. *Bulletin of the American Meteorological Society*, 85(3):381–394, 2004. doi: 10.1175/BAMS-85-3-381.

[21] William H Brune. Ways to specify water vapor, 2020. URL `https://www.e-education.psu.edu/meteo300/node/519`. [Accessed: 2020-11-12].

[22] The University of Arizona. Water vapor in air, 2013. URL `http://www.atmo.arizona.edu/students/courselinks/spring08/atmo336s1/courses/fall13/atmo551a/Site/ATMO_451a_551a_files/WaterVapor.pdf`. [Accessed: 2020-11-12].

[23] John M. Wallace and Peter V. Hobbs. *Atmospheric Science, An Introductory Survey*. Academic Press, 2006. ISBN 9780127329512.

[24] University of Colorado Boulder. Atmospheric thermodynamics. URL `https://atoc.colorado.edu/~cassano/atoc5050/Lecture_Notes/wh_ch3_part4.pdf`. [Accessed: 2020-11-12].

[25] David R Doelling, Norman G Loeb, Dennis F Keyes, Michele L Nordeen, Daniel Morstad, Cathy Nguyen, Bruce A Wielicki, David F Young, and Moguo Sun. Geostationary enhanced temporal interpolation for ceres flux products. *Journal of Atmospheric and Oceanic Technology*, 30(6):1072–1090, 2013. doi: 10.1175/JTECH-D-12-00136.1.

[26] David R Doelling, Moguo Sun, Le Trang Nguyen, Michele L Nordeen, Conor O Haney, Dennis F Keyes, and Pamela E Mlynczak. Advances in geostationary-derived longwave fluxes for the ceres synoptic (syn1deg) product. *Journal of Atmospheric and Oceanic Technology*, 33(3):503–521, 2016. doi: 10.1175/JTECH-D-15-0147.1.

[27] David A Rutan, Seiji Kato, David R Doelling, Fred G Rose, Le Trang Nguyen, Thomas E Caldwell, and Norman G Loeb. Ceres synoptic product: Methodology and validation of surface radiant flux. *Journal of Atmospheric and Oceanic Technology*, 32(6):1121–1143, 2015. doi: 10.1175/JTECH-D-14-00165.1.

[28] National Aeronautics and Space Administration. CERES_SYN1deg_Ed4.1 Subsetting and Browsing. URL `https://ceres-tool.larc.nasa.gov/ord-tool/jsp/SYN1degEd41Selection.jsp`. [Accessed: 2020-12-17].

[29] William D Collins, Phillip J Rasch, Brian E Eaton, Boris V Khattatov, Jean-Francois Lamarque, and Charles S Zender. Simulating aerosols using a chemical transport model with assimilation of satellite aerosol retrievals: Methodology for indoex. *Journal of Geophysical Research: Atmospheres*, 106(D7):7313–7336, 2001.

[30] National Aeronautics and Space Administration. CERES_SYN1deg_Ed4A Data Quality Summary (10/3/2017), 2017. URL `https://ceres.larc.nasa.gov/documents/DQ_summaries/CERES_SYN1deg_Ed4A_DQS.pdf`. [Accessed: 2020-05-18].

[31] Todd Mitchell. Elevation data in netcdf, 2014. URL `http://research.jisao.washington.edu/data_sets/elevation`. [Accessed: 2020-10-26].

[32] W. Lawrence Gates and Alfred B. Nelson. A new (revised) tabulation of the scripps topography on a 1 degree global grid: Part i: Terrain heights. 1975. URL `https://www.rand.org/pubs/reports/R1276-1.html`.

[33] Stuart M. Smith, Henry William Menard, and George Sharman. World-wide ocean depths and continental elevations averaged for areas approximating one degree squares of latitute and longitude. 1966.

[34] Information Network - CIESIN - Columbia University, International Food Policy Research Institute - IFPRI, The World Bank, and Centro Internacional de Agricultura Tropical - CIAT. *Global Rural-Urban Mapping Project, Version 1 (GRUMPv1): Urban Extents Grid*. Greenbelt, Maryland, USA, Goddard Earth Sciences Data and Information Services Center (GES DISC), 2011. doi: https://doi.org/10.7927/H4GH9FVG. [Accessed: 2020-10-29].

[35] Eric W. Weisstein. Arc second., 2020. URL https://mathworld.wolfram.com/ArcSecond.html. [Accessed: 2020-11-03].

[36] NREL. Reference air mass 1.5 spectra. URL https://www.nrel.gov/grid/solar-resource/spectra-am1.5.html. [Accessed: 2020-11-02].

[37] Stephanie White Quinn and Brad Lehman. A simple formula for estimating the optimum tilt angles of photovoltaic panels. In *2013 IEEE 14th Workshop on Control and Modeling for Power Electronics (COMPEL)*, pages 1–8. IEEE, 2013.

[38] Barbara Ridley, John Boland, and Philippe Lauret. Modelling of diffuse solar fraction with multiple predictors. *Renewable Energy*, 35(2):478–483, 2010.

[39] Douglas T Reindl, William A Beckman, and John A Duffie. Diffuse fraction correlations. *Solar energy*, 45 (1):1–7, 1990.

[40] Arvid Skartveit, Jan Asle Olseth, and Marit Elisabet Tuft. An hourly diffuse fraction model with correction for variability and surface albedo. *Solar Energy*, 63(3):173–183, 1998.

[41] RR Perez, Pierre Ineichen, EL Maxwell, RD Seal, and A Zalenka. Dynamic global-to-direct irradiance conversion models. *Ashrae Transactions*, 98(1):354–369, 1992.

[42] JL Torres, M De Blas, A García, and A De Francisco. Comparative study of various models in estimating hourly diffuse solar irradiance. *Renewable Energy*, 35(6):1325–1332, 2010.

[43] Sandeep Mishra. Selection Map for PV Module Installation Based on Shading Tolerability and Temperature Coefficient. Master's thesis, Delft University of Technology, Mekelweg 5, 2628 CD Delft, 2018. URL http://resolver.tudelft.nl/uuid:1ae70ca5-8a8e-4f5b-8838-a106de39c18c.

[44] Tim Stark. Modeling and Monitoring of a Floating Photovoltaic Pilot System. Master's thesis, Delft University of Technology, Mekelweg 5, 2628 CD Delft, 2020. URL http://resolver.tudelft.nl/uuid:1ae70ca5-8a8e-4f5b-8838-a106de39c18c.

[45] John Boland, Barbara Ridley, and Bruce Brown. Models of diffuse solar radiation. *Renewable Energy*, 33 (4):575–584, 2008.

[46] Muhammad Iqbal. *An Introduction to Solar Radiation*. Academic Press, 1983. ISBN 0123737508.

[47] Arno HM Smets, Klaus Jäger, Olindo Isabella, René ACMM Swaaij, and Miro Zeman. *Solar energy: The physics and engineering of photovoltaic conversion, technologies and systems*. UIT Cambridge, 2015.

[48] Hesan Ziar, Patrizio Manganiello, Olindo Isabella, and Miro Zeman. Photovoltatronics: intelligent pv-based devices for energy and information applications. *Energy & Environmental Science*, 14(1):106–126, 2021.

[49] Ameen M. Ali, K.S. Rahman, Lamya M. Ali, M. Akhtaruzzaman, K. Sopian, S. Radiman, and N. Amin. A computational study on the energy bandgap engineering in performance enhancement of cdte thin film solar cells. *Results in Physics*, 7:1066 – 1072, 2017. ISSN 2211-3797. doi: https://doi.org/10.1016/j.rinp.2017.02.032. URL http://www.sciencedirect.com/science/article/pii/S2211379717301468.

[50] Jonathan Lehr, Malte Langenhorst, Raphael Schmager, Simon Kirner, Uli Lemmer, Bryce S Richards, Chris Case, and Ulrich W Paetzold. Energy yield modelling of perovskite/silicon two-terminal tandem pv modules with flat and textured interfaces. *Sustainable Energy & Fuels*, 2(12):2754–2761, 2018. URL https://pubs.rsc.org/am/content/articlehtml/2018/se/c8se00465j.

[51] RG Ross Jr and MI Smokler. Flat-plate solar array project. volume 6: Engineering sciences and reliability. 1986.

[52] Marko Jošt, Benjamin Lipovšek, Boštjan Glažar, Amran Al-Ashouri, Kristijan Brecl, Gašper Matič, Artiom Magomedov, Vytautas Getautis, Marko Topič, and Steve Albrecht. Perovskite solar cells go outdoors: Field testing and temperature effects on energy yield. *Advanced Energy Materials*, page 2000454, 2020.

[53] Clemens Schwingshackl, Marcello Petitta, Jochen Ernst Wagner, Giorgio Belluardo, David Moser, Mariapina Castelli, Marc Zebisch, and Anke Tetzlaff. Wind effect on pv module temperature: Analysis of different techniques for an accurate estimation. *Energy Procedia*, 40:77–86, 2013. URL https://www.sciencedirect.com/science/article/pii/S1876610213016044.

[54] Armin Richter, Stefan W Glunz, Florian Werner, Jan Schmidt, and Andres Cuevas. Improved quantitative description of auger recombination in crystalline silicon. *Physical review B*, 86(16):165202, 2012.

[55] Andreas Schenk. Finite-temperature full random-phase approximation model of band gap narrowing for silicon device simulation. *Journal of Applied Physics*, 84(7):3684–3695, 1998.

[56] AB Sproul and MA Green. Intrinsic carrier concentration and minority-carrier mobility of silicon from 77 to 300 k. *Journal of Applied Physics*, 73(3):1214–1225, 1993.

[57] Romain Couderc, Mohamed Amara, and Mustapha Lemiti. Reassessment of the intrinsic carrier density temperature dependence in crystalline silicon. *Journal of Applied Physics*, 115(9):093705, 2014.

[58] CD Thurmond. The standard thermodynamic functions for the formation of electrons and holes in ge, si, gaas, and gap. *Journal of the Electrochemical Society*, 122(8):1133, 1975.

[59] T Trupke, Mr A Green, P Würfel, PP Altermatt, A Wang, J Zhao, and R Corkish. Temperature dependence of the radiative recombination coefficient of intrinsic crystalline silicon. *Journal of Applied Physics*, 94 (8):4930–4937, 2003.

[60] Pietro P Altermatt, Frank Geelhaar, Thorsten Trupke, Ximing Dai, Axel Neisser, and Ernst Daub. Injection dependence of spontaneous radiative recombination in c-si: experiment, theoretical analysis, and simulation. In *NUSOD'05. Proceedings of the 5th International Conference on Numerical Simulation of Optoelectronic Devices, 2005.*, pages 47–48. IEEE, 2005.

[61] Martin A Green. Self-consistent optical parameters of intrinsic silicon at 300 k including temperature coefficients. *Solar Energy Materials and Solar Cells*, 92(11):1305–1310, 2008.

[62] Marc Rüdiger, Johannes Greulich, Armin Richter, and Martin Hermle. Parameterization of free carrier absorption in highly doped silicon for solar cells. *IEEE transactions on electron devices*, 60(7):2156–2163, 2013.

[63] PV Education. Solar cell structure. URL https://www.pveducation.org/pvcdrom/solar-cell-operation/solar-cell-structure. [Accessed: 2021-04-22].

[64] Bert Holtslag. *Boundary Layer (Atmospheric) and Air Pollution: Modeling and Parameterization*, pages 265–273. 12 2015. ISBN 9780123822253. doi: 10.1016/B978-0-12-382225-3.00087-6.

[65] Earth System Research Laboratories, Global Monitoring Laboratory. Surfrad aerosol optical depth. URL https://www.esrl.noaa.gov/gmd/grad/surfrad/aod/. [Accessed: 2021-04-08].

[66] M Rezazadeh, P Irannejad, and Y Shao. Climatology of the middle east dust events. *Aeolian Research*, 10:103–109, 2013.

[67] Haim Kutiel Hadar Furman. Dust storms in the middle east: sources of origin and their temporal characteristics. *Indoor and Built Environment*, 12(6):419–426, 2003.

[68] globalsolaratlas.info. Global solar atlas, 2021. URL https://globalsolaratlas.info/map. [Accessed: 2021-04-09].

[69] Marios Theristis, Cameron Stark, and Tadhg S O'Donovan. Determination of the cooling requirements for single cell photovoltaic receivers under variable atmospheric parameters. In *2015 IEEE 42nd Photovoltaic Specialist Conference (PVSC)*, pages 1–5. IEEE, 2015.

[70] Jason Fernando. R-squared definition, 2020. URL https://www.investopedia.com/terms/r/r-squared.asp. [Accessed: 2021-04-10].

[71] Florent Sahli, Jérémie Werner, Brett A Kamino, Matthias Bräuninger, Raphaël Monnard, Bertrand Paviet-Salomon, Loris Barraud, Laura Ding, Juan J Diaz Leon, Davide Sacchetto, et al. Fully textured monolithic perovskite/silicon tandem solar cells with 25.2% power conversion efficiency. *Nature materials*, 17(9): 820–826, 2018.

[72] Ibraheem Almansouri, Anita Ho-Baillie, and Martin A Green. Ultimate efficiency limit of single-junction perovskite and dual-junction perovskite/silicon two-terminal devices. *Japanese Journal of Applied Physics*, 54(8S1):08KD04, 2015.

[73] Shuangyong Sun, Teddy Salim, Nripan Mathews, Martial Duchamp, Chris Boothroyd, Guichuan Xing, Tze Chien Sum, and Yeng Ming Lam. The origin of high efficiency in low-temperature solution-processable bilayer organometal halide hybrid solar cells. *Energy & Environmental Science*, 7(1):399–407, 2014.

[74] Moritz H Futscher and Bruno Ehrler. Efficiency limit of perovskite/si tandem solar cells. *ACS Energy Letters*, 1(4):863–868, 2016.

[75] Wladimir Köppen. *Die klimate der Erde*. de Gruyter, 2020.

[76] Hylke E Beck, Niklaus E Zimmermann, Tim R McVicar, Noemi Vergopolan, Alexis Berg, and Eric F Wood. Present and future köppen-geiger climate classification maps at 1-km resolution. *Scientific data*, 5(1): 1–12, 2018.

[77] Ian Marius Peters and Tonio Buonassisi. How changes in worldwide operating conditions affect solar cell performance. *Solar Energy*, 220:671–679, 2021.